Temporal properties of counterpropagating twin photons

Tommaso Corti

Supervisor: Dr. Alessandra Gatti, Dr. Enrico Brambilla

Dipartimento di Scienza e Alta Tecnologia
Università degli Studi dell'Insubria

This dissertation is submitted for the degree of
Dottorato di Ricerca in Fisica

April 2017

to my parents . . .

Acknowledgements

This thesis and the work that it contains would not have been possible without the support and guidance provided by those around me, and especially by my supervisor, Dr. Alessandra Gatti. I would like to thank her for giving me the opportunity to be a member of his research group and benefit from his vast knowledge and passion for research. Thanks to her, the last four years have been an extremely interesting and a great learning experience. I wish to thank Dr. Enrico Brambilla for his patience and continuous support. His encouragement helped me in all the time of research and writing of this thesis.

A special thanks to my family. Words cannot express how grateful I am to my mother Nicoletta and to my father Giuseppe, for all of the sacrifices that they have made on my behalf. I would also like to thank all of my friends who supported me in these PhD years.

Abstract

Twin photon pairs generated through parametric downconversion (PDC) in a χ^2 medium is one of the most widely used source of entanglement. We focus here on a non-conventional geometry in which one of the twin photons propagates in the opposite direction with respect to the pump beam, exploiting quasi-phase-matching in a periodically poled crystal. Through predicted almost 50 years ago, this new PDC configuration has been realized experimentally only recently [1] thanks to new fabrication techniques achieving the required sub-micrometer poling period. Because of the presence of distributed feedback, the optical system has been shown to behave as a Mirrorless Optical Parametric Oscillator (MOPO) and exhibits peculiar spectral properties which strongly differ from those found in more common geometries involving co-propagating beams. In this work we provide a detailed analysis of the correlation and coherence properties of counter-propagating twin beams both in the purely spontaneous regime and in the neighborhood of the MOPO threshold.

We consider on the on side the regime of spontaneous pair production where the characteristic narrow band of the counter-propagating twin beams offers the unique opportunity of generating heralded single photon states with a high degree of purity, a relevant property for applications in quantum communication [2]. In this context, we investigate how the degree of separability of the twin photon state varies with the pump pulse duration τ_p. We find that two well separated time scales characterize the system dynamics: a short time scale τ_{gvm}, in the picoseconds range, corresponding to the typical temporal delay of co-propagating waves due to group-velocity mismatch, and a much longer time scale τ_{gvs} associated with the temporal separation of counter-propagating waves. Such a difference of time scales occurs naturally in the counterpropagating configuration, for basically any kind of material and tuning condition. Because of this same feature, counter-propagating twin photons in a pure state can in principle be heralded at any wavelength by choosing the appropriate poling period. We show that a high degree of separability can be achieved when the pump pulse duration satisfy the condition $\tau_{gvm} \ll \tau_p \ll \tau_{gvs}$, as put in evidence from the evaluation of Schmidt number as a function of the pump pulse duration which reaches a minimum close to unity in this region. The separability is lost in the nearly monochromatic limit ($\tau_p \gg \tau_{gvs}$) as well as for ultra-short pulses ($\tau_p \ll \tau_{gvm}$), where the entanglement between the signal

and idler frequencies can be inferred by the non factorable shape of the spectral biphoton amplitude. We offer a physical interpretation of such a behaviour, and a detailed analysis of the Schmidt number characterizing the entanglement of the state.

We also considered a completely different regime of operation, close to the MOPO threshold, where the combined effect of stimulated PDC and distributed feedback affects dramatically the property of coherence of the field. Our analysis put in evidence a progressive narrowing of both the spectral twin beam correlation and the intensity spectra as the pump field intensity approaches its threshold value. This translates into a drastic increase of the correlation and coherence times in the temporal domain, a feature which can be attributed to the critical slowing down of the fluctuation dynamics characterizing the transition toward coherent emission occurring at the MOPO threshold.

Furthermore, we investigate the potentiality of the source to generate squeezing and EPR type correlations in the threshold vicinity. In this regards, the obtained results shows that the system displays a behaviour which is very similar to that found in standard optical parametric oscillators enclosed in a resonant cavity. In the last part of the work, we present some preliminary results from numerical simulations illustrating the transition above the MOPO thresholds. We also take into account non collinear PDC emission, showing explicitely that the spatial and the temporal degrees of freedoms of the emitted twin photons are almost uncoupled. This feature strongly distinguish the counter-propagating configuration from standard co-propagating geometries where the phase-matching mechanism usually leads to strong angular dispersion.

Table of contents

List of figures **xi**

Introduction **1**

1 The model **5**
1.1 Qualitative description of the PDC process in a periodically poled crystals . 6
1.2 Classical propagation equations in $\chi^{(2)}$ media 9
1.3 The counterpropagating geometry 15
1.4 Quantization of the electromagnetic field 16

2 The classical model and the MOPO threshold **21**
2.1 The classical model 21
2.2 The stationary solution and the MOPO threshold 22
2.3 Review of experimental findings 27

3 Spontaneous pair production regime **31**
3.1 Spectral biphoton correlation 35
3.2 Interpretation: biphoton correlation in the time domain 41
3.3 Spectral coherence 44
3.4 Schmidt number of entanglement 52

4 Stimulated pair production regime **59**
4.1 Coherence and correlation 63
4.2 Low gain regime, $g \ll \frac{\pi}{2}$ 67
4.3 Biphoton correlation 67
4.4 Coherence function 69
4.5 High-gain regime (threshold region), $g \to \frac{\pi}{2}$ 70
4.6 Field correlation 71
4.7 Coherence function 74

4.8 An intuitive picture 74
4.9 Numerical simulations, crossing the threshold 76

5 Quadrature correlations in the MOPO below threshold 83

6 Spatio-temporal aspects 93
6.1 Evaluation of the effective nonlinear coupling costant 100

Conclusions 103

References 107

Appendix A Nonlinear polarization 111

Appendix B Relation between formalisms 113

List of figures

1.1 Schematic representation of the PDC process 5
1.2 Schematic representations of the PDC process (co-propagating configuration) in a second-order nonlinear optical material 7
1.3 Schematic representations of the PDC process (counter-propagating configuration) in a second-order nonlinear optical material 8

2.1 Schematic representations of the MOPO configuration in the classical model 22
2.2 Conversion efficiency and pump depletion of the MOPO 27
2.3 Microscope image of a PPKTP crystal 28
2.4 Experimental results in [1] 28
2.5 Schematic representations of the PDC process in a KTP crystal (counterpropagating geometry) 29

3.1 Ratio $\eta = \tau_{gvm}/\tau'_{gvs}$ for periodically poled KTP and $LiNbO_3$ 37
3.2 Biphoton correlation $|\Psi|$ in various pumping regimes. 38
3.3 Temporal correlation of twin photons $|\phi(\bar{t}_i,\bar{t}_s)|$ 42
3.4 Coherence functions $|G(\Omega,\Omega')|$ of signal and idler fields for different pumping regime. 46
3.5 Emission spectra $G^{(1)}(\Omega,\Omega) = \tilde{\mathcal{I}}(\Omega)$ for a quasi CW pump pulse. 47
3.6 Schmidt number, as a function of the pump spectral bandwidth or duration. 54
3.7 Schmidt number, as a function of the pump spectral bandwidth or duration, inset of Fig. 3.6(a) 57
3.8 Role of GVM in determining the purity of the state: Schmidt number for different crystals and/or different phase matching conditions 58

4.1 Biphoton correlation in the spontaneous PDC regime 68
4.2 PDC spectrum at the crystal output faces and coherence function in the time domain in the low gain regime 70

4.3 Spectral correlation density and biphoton correlation in the temporal domain in different gain regimes. 72
4.4 Spectrum and temporal coherence function near threshold. 75
4.5 Schematic representation of the propagation along the crystal of photon pairs originating from a PDC event 77
4.6 PDC spectrum at the crystal exit faces in the lowgain and high gain regime . 80
4.7 Pump depletion η as a function of the parametric gain g 81
4.8 Spectra over threshold for increasing values of ε 81
4.9 Evolution of the FWHM of the emission spectra crossing threshold 82

5.1 Squeezing spectrum $\Sigma_{\pm}^{S}(\Omega)$ for different values of the parametric gain g . . 89
5.2 Anti-squeezing spectrum $\Sigma_{\pm}^{A}(\Omega)$ for different values of the parametric gain . 90
5.3 Squeezing spectrum $\Sigma_{\pm}^{S}$ and anti-squeezing spectrum $\Sigma_{\pm}^{A}$ for $\Omega = 0$ as functions of g 90

6.1 Emission spectrum in the $(\boldsymbol{q},\Omega)$ plane in the copropagating configuration and in the counterpropagating configuration 95
6.2 Crystal reference frame and pump reference frame 97
6.3 Signal emission spectrum in the (λ,α) plane in the co-propagating configuration and in the counter-propagating configuration 98
6.4 Signal emission spectrum at the output face of a KTP crystal in the $(\boldsymbol{q},\Omega)$ plane and in the (λ,α) plane for for the non degenerate case. 99
6.5 Coefficient d_{eff} as a function of the emission angles α and β 101
6.6 Signal emission spectrum in the walk-off plane and in the plane perpendicular to the walk-off 102

Introduction

This thesis analyzes the properties of spontaneous parametric down-conversion (SPDC) occurring in periodically poled $\chi^{(2)}$ media that, under certain conditions, allow the generation of counterpropagating twin beams. SPDC process has become one of the most efficient and widely used source of entangled photon pairs (biphotons) and of single photons, heralded by the detection of the partner. The microscopic process, where a high energy photon of the pump laser splits into two lower energy photons, is ruled by conservation laws (energy, momentum, angular momentum, polarization), which are at the origin of a wide range of quantum correlations between the members of the pair. The SPDC process has been extensively studied in the standard configuration, where the down-converted photon pairs propagate in the same direction of the pump. In this configuration the two photon state is characterized by a high dimensional entanglement, because a quantum correlation is present over huge temporal and angular bandwidths. The temporal correlation was historically the first one to be studied [3–5]: in the standard configuration a pair of twin photon, generated at the same point, propagate nearly in the same direction, and exit the crystal almost simultaneously. A small uncertainty in their temporal separation is present because of their different group velocities or because of the group velocity dispersion, and can be reduced to the smallest limit when the spatial degrees of freedom are properly controlled [6, 7]. Such a short correlation time results in a high-dimensional temporal entanglement [8]. Its spectral counterpart is the huge spectral bandwidth of SPCD emission, and the high dimensional spectral entanglement of SPDC photons [9]. High-dimensional entanglement offers relevant opportunities in view of broadband quantum communication schemes, but can also be regarded as a negative feature, because it affects the purity of heralded single photons. In fact, if we consider PDC as a source of single photons heralded by their twin partner, entanglement must be avoided as much as possible, since the heralded photons are required to be in a pure state in order to provide high-visibility interference [10].

This work is devoted to the description of a non-conventional configuration, where one of the down-converted photons is generated in the backward direction with respect to the pump laser, in a periodically poled crystal. A unique feature of this counterpropagating geometry is

the presence of distributed feedback which leads to a transition towards coherent oscillations when the pump intensity exceeds a given threshold value. Above this threshold the system can in principle be exploited as a source of coherent and tunable radiation, thereby the name mirrorless optical parametric oscillators (MOPO).

Although predicted almost 50 years ago [11], counterpropagating down-conversion has been only recently realized [1, 12], thanks to technical advancements in achieving the submicrometer poling periods necessary to phase match the nonlinear interaction [13–15]. Thus, only few experimental results have been obtained until now. The first experimental realization of a MOPO was performed in 2007 by C. Canalias and V. Pasiskevicius. In [1] the existence of a threshold for the pump intensity beyond which the system starts to oscillate coherently is experimentally demonstrated. Beyond threshold the co-propagating signal field is essentially a wavelength-shifted replica of the pump spectrum, while the bandwidth of the counterpropagating idler field is two orders of magnitude narrower than that of the pump. The unusual properties of temporal coherence of the MOPO radiation above threshold have been studied in Ref. [12, 16, 17]. The three wave-mixing interaction with counterpropagating fields has been investigated also in different contexts [18–21]. An overview can be found in [13].

Our works wants to give a full theoretical description of the SPDC process in this non-conventional configuration, which lacks in literature, focusing on the temporal coherence and correlation properties of the down-converted photon pairs. Our analysis mainly focus on two parametric regimes below the MOPO threshold: the purely spontaneous regime, far from threshold, in which the photon pairs are emitted independently along the crystal, and the regime close to threshold where most photon pairs originate from stimulated emission in a cascading process and distributed feedback becomes highly relevant. In the regime of spontaneous pair production, well below the MOPO threshold, we analyze the temporal quantum properties of counterpropagating twin photons generated in a purely collinear configuration. We provide a detailed theoretical description of the effects of the spectral properties of the pump laser on the degree of entanglement of the state. We also investigate the system potentiality as a source of heralded single photons with a high level of purity, identifying the conditions under which the twin photon state may become separable and providing a consistent interpretation of the transition between separibility and entanglement (Chap. III).

In the regime of stimulated pair production, including also the region close to the MOPO threshold, the effect of the feedback mechanism starts to play a determinant role. We provide here for the first time a complete theoretical description of the critical behavior of coherence and correlation of counterpropagating beams considering a monochromatic plane wave

pump. We illustrate the divergence of the correlation time and the critical slowing down phenomenon of temporal fluctuations occurring when approaching the transition towards coherent oscillations and provide an intuitive picture explaining the transition between these two regimes (Chap. IV). We present also some preliminary results from numerical simulations illustrating the transition above the MOPO threshold. Furthermore, we investigate the potentiality of the source to generate squeezing and EPR type correlations in the threshold vicinity. In this regards, the obtained results shows that the system displays a behaviour which is very similar to that found in standard optical parametric oscillators enclosed in a resonant cavity (Chap. V)

In the last part of the work, we also take into account non collinear PDC emission, showing explicitely that the spatial and the temporal degrees of freedoms of the emitted twin photons are almost uncoupled. This feature strongly distinguishes the counter-propagating configuration from standard co-propagating geometries where the phase-matching mechanism usually leads to strong angular dispersion (Chap. VI).

The thesis is organized as follows: in Chap. I we introduce the general quantum model that we shall use to describe the PDC field generated in a periodically poled $\chi^{(2)}$ crystal with a counter-propagating geometry. In Chap. II we derive the solution for the classical MOPO (the classical counter-part of the model illustrated in Chap. I), showing the existence of a threshold above which coherent oscillations take place. In Chap. III we study the quantum properties of the twin photons emitted in the regime of purely spontaneous PDC, well below the MOPO threshold, exploring the potentiality of the source for generating single heralded photons with a high degree of purity. Chapter IV investigates the transition from the regime far from threshold, where purely spontaneous down-conversion is the main source of twin photon pairs, up to a regime close to threshold where the combined effect of stimulated PDC and distributed feedback affects dramatically the properties of coherence and correlation of the light source. We also show some preliminary numerical results illustrating the behavior of the MOPO emission during the transition from below to above threshold. In Chapter V we turn our attention to the genuinely quantum properties of the light source in the vicinity of the threshold, investigating its potentiality to generate squeezing. In Chapter VI non-collinear emission is taken into account and we illustrated through some examples how the spatial and the temporal degrees of freedom of the emitted twin photons are very weakly coupled by phase-matching, a distinguishing feature of the counter-propagating geometry.

Chapter 1

The model

In this chapter we introduce the model that we shall use to describe the parametric down-conversion process in a $\chi^{(2)}$ periodically poled nonlinear crystal. We first give a short overview of the process of parametric down-conversion, showing how the phase-matching conditions between the pump field and the two down-converted fields determines the PDC emission spectrum. After that we will derive the classical propagation equations for the fields involved in the process.

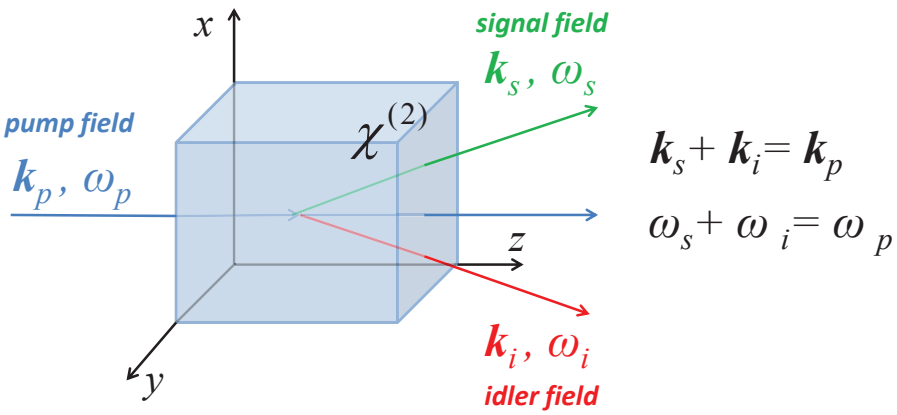

Fig. 1.1 Schematic representation of the PDC process in which an intense pump field propagating through a quadratic nonlinear medium is partially down-converted into two fields at lower frequencies, called signal and idler fields.

1.1 Qualitative description of the PDC process in a periodically poled crystals

The PDC process, taking place in a nonlinear crystal with a quadratic nonlinearity is shown schematically in Fig. 1.1. An intense coherent pump pulse of central frequency ω_p is injected into the nonlinear medium and is partially down-converted into two of fields of lower frequencies. The process exploits the presence of a quadratic $\chi^{(2)}$ term in the power expansion of the macroscopic polarization of the dielectric medium [22, 23], with a quadratic dependence on the electric field of the form

$$P_l^{NL} = \varepsilon_0 \chi^2_{jkl} E_j E_k \quad (i,j,k = x,y,z), \tag{1.1}$$

a feature which characterizes non crystalline structures lacking an inversion symmetry (the $\chi^{(2)}$ tensor is generally frequency dependent as described in [22]).

At an elementary level, the process occurs because some of the pump photons are spontaneously down-converted into two pairs of photons of lower energies $\hbar\omega_s$ and $\hbar\omega_i$, usually referred to as *signal* and *idler* photon pairs or simply *twin photons*. For each elementary PDC process, the energy and momentum conservation laws are expressed by the following phase-matching conditions

$$\omega_p = \omega_s + \omega_i, \tag{1.2}$$

$$k_{pz}(\boldsymbol{q}_p, \omega_p) = k_{sz}(\boldsymbol{q}_s, \omega_s) \pm k_{iz}(\boldsymbol{q}_i, \omega_i), \tag{1.3}$$

$$\boldsymbol{q}_p = \boldsymbol{q}_s + \boldsymbol{q}_i, \tag{1.4}$$

where $k_{jz}(\omega_j) = \frac{\omega_j n_j(\omega_j)}{c}$, $(j = p,s,i)$ denotes the wave vector components along the propagation direction associated to the pump, the signal and the idler photons, being $\boldsymbol{q}$ the transverse wave vector and $n(\omega)$ the refractive index. Photon pairs are emitted only for those frequencies and propagation directions satisfying conditions (1.2-1.4), which thus determines the angular emission spectrum of the down-converted signal and idler fields.

In a bulk media, conditions (1.3,1.4) can generally not be satisfied by three waves with the same polarizations since the refractive index is an increasing function of the frequency under condition of normal dispersion. The birefringence characterizing the propagation of waves with different polarizations in a $\chi^{(2)}$ nonlinear crystal is the most common optical property exploited in order to achieve phase-matching between the three interacting waves at the frequencies ω_p, ω_s and $\omega_i = \omega_p - \omega_s$. For each propagation direction, two different field polarization directions are usually allowed inside an anisotropic $\chi^{(2)}$ nonlinear crystal: a *slow*

wave with a high refraction index n_+, and *fast* wave with lower refraction index n_- [23, 24]. In order to satisfy the phase-matching conditions (1.3,1.4), the pump field at the highest frequency ω_p must necessarily be in the slow wave polarization, while the signal and idler fields can either both have the same fast wave polarization (type I phase-matching), or be differently polarized (type II phase-matching). Considering the simplest case of an uniaxial crystal with an ordinary and an extraordinary refraction index (only the latter depends on the propagation direction) the following phase-matching configuration are possible:

- Type I configuration: the signal and idler fields have the same polarization (ordinary or extraordinary). For negative crystals the down-conversion process is allowed for an extraordinary pump, and ordinarily polarized signal and idler waves, and this kind of interaction is therefore called Type I $e \rightarrow oo$ phase matching (the first index refers to the pump, while the others two to the signal and idler waves, respectively). In positive crystals, instead, the phase matching conditions can be satisfied only in a $o \rightarrow ee$ configuration.

- Type II configuration: the signal and idler fields have different polarization. In this case, for negative crystals the allowed interaction is of the type $e \rightarrow oe$, whereas for positive crystals it is $o \rightarrow oe$.

In this work we shall consider the process of parametric down-conversion in a periodically poled crystals (PPNC), which allows to achieve phase-matching between the three interacting wave with a higher degree of flexibility with respect to other phase-matching techniques (see [22, 25, 26]). Periodically poled materials are nonlinear crystals that are fabricated so

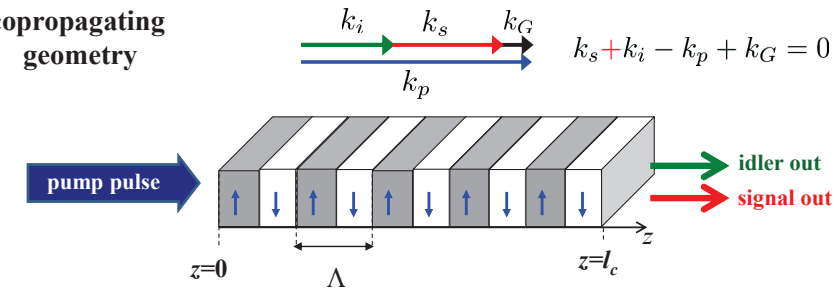

Fig. 1.2 Schematic representations of the PDC process (standard co-propagating configuration) in a second-order nonlinear optical material in the form of a periodically poled crystal, in which the crystalline axis alternates in orientation along the propagation direction z.

that the orientation of one of the crystalline axis is inverted periodically as a function of position within the material along the optical mean propagation axis, as illustrated in Fig. 1.2. The typical poling period Λ of commercially available PPNC ranges typically from a few micrometers up to several tens of micrometers. The inversion of the orientation of one of

the crystalline axis results in periodic alternation of the sign of the nonlinear susceptibility $\chi^{(2)}(z)$, that can compensate for a nonzero wavevector mismatch Δk (see Fig. 1.2). The momentum conservation law is replaced with the following less restrictive relation, in which the first-order momentum associated to the nonlinear grating $k_G = 2\pi/\Lambda$ can participate in the momentum balance (Quasi Phase Matching).

$$k_{sz}(\omega_s) + k_{iz}(\omega_i) - k_{pz}(\omega_p) + k_G = 0, \quad \text{(a) co-propagating case.} \tag{1.5}$$

Choosing appropriately the poling period Λ every particular couple of conjugated frequencies ω_s and ω_i can in principle be phase-matched. More generally any three-wave mixing process that satisfies energy conservation can be phase-matched, including processes with combinations of polarizations not allowed in a bulk medium. This allows one to use the largest nonlinear coefficient of the material in the nonlinear interaction.

In this works we shall focus on a more exotic quasi-phase matching configuration in which one of the two fields, say the idler field, propagates opposite to the pump direction as shown schematically in Fig.1.3. This counterpropagating geometry has been proposed by Harris in bulk media in 1966 [11] and requires a submicrometric poling period, with Λ on the same order of the pump wavelength λ_p. In such a condition the momentum imparted by the nonlinear grating k_G is sufficiently large to compensate for the pump photon momentum and the photons emitted in each elementary down-conversion process must propagate along opposite direction in order to satisfy momentum conservation. Relation (1.5) is now substituted with the relation (see also Fig.1.3)

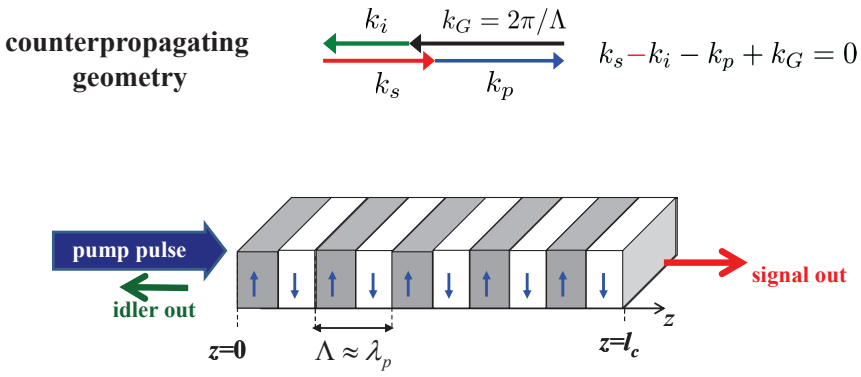

Fig. 1.3 Schematic representations of the PDC process (counter-propagating configuration) in a second-order nonlinear optical material in the form of a periodically poled crystal ($\Lambda \approx \lambda_p$).

$$k_{sz}(\omega_s) - k_{iz}(\omega_i) - k_{pz}(\omega_p) + k_G = 0, \quad \text{(b) counter-propagating case.} \tag{1.6}$$

We shall mostly focus on this commonly realized type 0 interaction [1], where pump, signal and idler fields have extraordinary polarization ($e-ee$), and that allows to exploit the largest nonlinear coefficient $d33$. We leave however the formalism quite general: the subscript j in the wave number may refer to dispersion relations for either the ordinary or extraordinary wave, including thus type I, II or 0 PDC.

Counterpropagating PDC presents unique features, as the presence of distributed feedback which leads to a transition towards coherent oscillations [27] when the pump intensity exceeds a given threshold value. This concept was proposed theoretically many years ago [11], but only recently experimental evidence has been achieved [1], due to the technical difficulties involved in the fabrication of periodically poled crystal with the required submicrometric poling period. Above threshold the system can in principle be exploited as a source of coherent and tunable radiation [2]. A second peculiar feature of the MOPO is the narrow spectral bandwidth of emission (the backward-propagating wave can be more monochromatic than the pump laser [1]). In the quantum domain, as pointed out in [2], counterpropagating SPDC can generate highly monochromatic photon pairs in an almost separable state, which makes it a promising source of high-purity heralded single photons.

1.2 Classical propagation equations in $\chi^{(2)}$ media

In this section we will derive the field propagation equations that characterize the parametric down conversion process in a periodically poled nonlinear medium. We initially follow the approach proposed in [28] in the case of a bulk crystal. Further references can be found in [22] and in [29].

We start from the macroscopic Maxwell's equations, from which it is possible to derive the classical propagation equation for an electromagnetic field in a medium, i.e.

$$-\vec{\nabla}\times\vec{\nabla}\times\boldsymbol{E}(\boldsymbol{r},t)-\frac{1}{c^2}\frac{\partial^2\boldsymbol{E}(\boldsymbol{r},t)}{\partial t^2}=\mu_0\frac{\partial^2\boldsymbol{P}(\boldsymbol{r},t)}{\partial t^2}\qquad\text{with}\quad\boldsymbol{r}=(x,y,z),\tag{1.7}$$

where c is the speed of light, μ_0 is the vacuum permeability and $\boldsymbol{P}$ is the macroscopic polarization density vector. For the transverse component of the fields, i.e. the component perpendicular to the propagation direction, we have that $\vec{\nabla}\cdot\boldsymbol{E}_\perp(\boldsymbol{r},t)=0$ and it is thus possible to write $\vec{\nabla}\times\vec{\nabla}\times\boldsymbol{E}_\perp(\boldsymbol{r},t)=-\nabla^2\boldsymbol{E}_\perp(\boldsymbol{r},t)+\vec{\nabla}[\vec{\nabla}\cdot\boldsymbol{E}_\perp(\boldsymbol{r},t)]=\nabla^2\boldsymbol{E}_\perp(\boldsymbol{r},t)$. The propagation equation (1.7) now reads:

$$\nabla^2\boldsymbol{E}_\perp(\vec{r},t)-\frac{1}{c^2}\frac{\partial^2\boldsymbol{E}_\perp(\boldsymbol{r},t)}{\partial t^2}=\frac{1}{\varepsilon_0 c^2}\frac{\partial^2\boldsymbol{P}_\perp(\boldsymbol{r},t)}{\partial t^2}.\tag{1.8}$$

In the general case of anisotropic media, such the ones considered in the following, one should consider a propagation equation also for the longitudinal component of the electromagnetic field but, since this component is usually very small compared to the transverse one, it can be neglected. From now on in order to simplify the notation we drop the subscript $\perp$.

It is now convenient to move to the frequency domain, introducing the Fourier transforms with respect to the time t and space coordinates $\boldsymbol{x} \equiv (x,y)$:

$$E_j(\boldsymbol{q},\omega,z) = \int \frac{d\boldsymbol{x}}{2\pi} \int \frac{dt}{\sqrt{2\pi}} E_j(\boldsymbol{x},t,z) e^{-i\boldsymbol{q}\cdot\boldsymbol{x}+i\omega t} \quad (j=x,y,z) \tag{1.9a}$$

$$P_j(\boldsymbol{q},\omega,z) = \int \frac{d\boldsymbol{x}}{2\pi} \int \frac{dt}{\sqrt{2\pi}} P_j(\boldsymbol{x},t,z) e^{-i\boldsymbol{q}\cdot\boldsymbol{x}+i\omega t}, \tag{1.9b}$$

where $\boldsymbol{q}$ is the transverse wave vector, ω is the frequency and where the index j indicates a particular component of the vector along the coordinate axis. In the Fourier domain, the propagation equations for the pump, signal and idler fields become:

$$\left(\frac{\partial^2}{\partial z^2} - \boldsymbol{q}^2 + \frac{\omega^2}{c^2}\right) E_j(\boldsymbol{q},\omega,z) = -\frac{\omega^2}{\varepsilon_0 c^2} P_j(\boldsymbol{q},\omega,z) \qquad (j=x,y,z) \tag{1.10}$$

In parametric media material, far away from atomic resonances, the macroscopic polarization can be written as a power series of the electric field with ascending powers giving smaller and smaller contributions. We separate the linear and the nonlinear part of the macroscopic polarization by setting:

$$\boldsymbol{P}(\boldsymbol{r},t) = \boldsymbol{P}^L(\boldsymbol{r},t) + \boldsymbol{P}^{NL}(\boldsymbol{r},t). \tag{1.11}$$

The linear component can be written in the form [22]

$$P_j^L(\boldsymbol{q},\omega) = \sum_k \varepsilon_0 \chi_{jk}^{(1)}(\boldsymbol{q},\omega) E_k(\boldsymbol{q},\omega) = \sum_k \varepsilon_0 [n_{jk}^2(\boldsymbol{q},\omega) - 1] E_k(\boldsymbol{q},\omega), \qquad j,k = x,y,z \tag{1.12}$$

where $\chi_{jk}^{(1)} = n_{jk}^2 - 1$ denotes the linear susceptibility tensor in the chosen reference frame. For the nonlinear component we consider only the quadratic nonlinearity, neglecting higher order contribution such as the Kerr nonlinearity. The nonlinear polarization describes a number of wave-mixing processes such as sum frequency and second-harmonic generation to higher frequencies. Here we shall assume they do not contribute significantly to the field dynamics and consider only the interaction involving the exchange of energy between the pump field of central frequency ω_p and the two down-converted fields of lower central frequencies ω_s and ω_i such that $\omega_s + \omega_i = \omega_p$.

The nonlinear polarization terms for the pump, the signal and the idler fields describing their interaction are then given by

$$P_p^{NL}(\boldsymbol{q},\omega) = \varepsilon_0\chi^{(2)}\int d\boldsymbol{q}'d\omega' E_s(\boldsymbol{q}',\omega')E_i(\boldsymbol{q}-\boldsymbol{q}',\omega-\omega'), \tag{1.13a}$$

$$P_s^{NL}(\boldsymbol{q},\omega) = \varepsilon_0\chi^{(2)}\int d\boldsymbol{q}'d\omega' E_p(\boldsymbol{q}+\boldsymbol{q}',\omega+\omega')E_i^*(\boldsymbol{q}',\omega'), \tag{1.13b}$$

$$P_i^{NL}(\boldsymbol{q},\omega) = \varepsilon_0\chi^{(2)}\int d\boldsymbol{q}'d\omega' E_p(\boldsymbol{q}+\boldsymbol{q}',\omega+\omega')E_s^*(\boldsymbol{q}',\omega'), \tag{1.13c}$$

where for simplicity we did not take into account dispersion phenomena of the second-order nonlinearity and χ^2 denotes the effective second-order susceptibility along the pump field propagation direction (see Appendix A for further details).

Until now, we did not make any explicit assumptions about the propagation directions of the down-converted signal and idler fields $\boldsymbol{E}_s$ and $\boldsymbol{E}_i$ in our model equations. As shown qualitatively in the previous sections, they are ultimately determined by the particular quasi-phasematching conditions imposed by the crystal nonlinear grating. In order to better illustrate this point, we now derive separate equations for both the forward and a backward propagating components of the two down-converted fields and show explicitly how the periodic poling selects the components that survives because of quasi phase-matching. We follow the general procedure outlined in [30], starting from the propagation equations (1.10) rewritten in the form

$$\left[\frac{\partial^2}{\partial z^2}+k_{jz}^2(\boldsymbol{q},\omega)\right]E_j(\boldsymbol{q},\omega,z) = -\frac{\omega^2}{\varepsilon_0 c^2}P_j^{NL}(\boldsymbol{q},\omega,z) \qquad j=p,s,i, \tag{1.14}$$

where

$$k_{jz}(\boldsymbol{q},\omega) = \sqrt{k_j^2(\boldsymbol{q},\omega)-q^2} \qquad j=p,s,i. \tag{1.15}$$

is the longitudinal k-vector component associated to the j-polarized plane-wave mode of frequency ω and transverse wave-vector $\boldsymbol{q}$. In order to simplify the notation we introduce the three-dimensional vector $\boldsymbol{u}=(\boldsymbol{q},\omega)$. We now consider the Fourier transform of the signal and idler electric fields and polarizations with respect to the longitudinal coordinate z:

$$E_j(\boldsymbol{u},\beta) \equiv \int \frac{dz}{\sqrt{2\pi}}e^{-i\beta z}E_j(\boldsymbol{u},z)\,, \qquad P_j^{NL}(\boldsymbol{u},\beta) \equiv \int \frac{dz}{\sqrt{2\pi}}e^{-i\beta z}P_j^{NL}(\boldsymbol{u},z). \tag{1.16}$$

Eq. (1.14) transforms then to

$$[-\beta^2+k_{jz}^2(\boldsymbol{u})]E_j(\boldsymbol{u},\beta) = -\frac{\omega^2}{\varepsilon_0 c^2}P_j^{NL}(\boldsymbol{u},\beta), \quad (j=s,i). \tag{1.17}$$

Simple manipulation allows to rewrite this equation in the following form

$$E_j(\boldsymbol{u},\beta) = \frac{\omega^2}{\varepsilon_0 c^2}\frac{P_j^{NL}(\boldsymbol{u},\beta)}{k_{jz}^2(\boldsymbol{u})-\beta^2} \tag{1.18}$$

$$= \frac{\omega^2}{\varepsilon_0 c^2}\frac{1}{2k_{jz}(\boldsymbol{u})}\left[\frac{1}{\beta-k_{jz}(\boldsymbol{u})}-\frac{1}{\beta+k_{jz}(\boldsymbol{u})}\right]P_j^{NL}(\boldsymbol{u},\beta). \tag{1.19}$$

Notice that the decomposition at the second line is valid only for $k_{jz}\neq 0$. Relation (1.19) suggests to separate the field E_j into a forward and a backward propagating component by setting:

$$E_j(\boldsymbol{u},\beta) = E_j^f(\boldsymbol{u},\beta)+E_j^b(\boldsymbol{u},\beta), \tag{1.20}$$

with

$$E_j^f(\boldsymbol{u},\beta) = \frac{\omega^2}{\varepsilon_0 c^2}\frac{1}{2k_{jz}(\boldsymbol{u})}\frac{1}{\beta-k_{jz}(\boldsymbol{u})}P_j^{NL}(\boldsymbol{u},\beta), \tag{1.21a}$$

$$E_j^b(\boldsymbol{u},\beta) = -\frac{\omega^2}{\varepsilon_0 c^2}\frac{1}{2k_{jz}(\boldsymbol{u})}\frac{1}{\beta+k_{jz}(\boldsymbol{u})}P_j^{NL}(\boldsymbol{u},\beta). \tag{1.21b}$$

In order to show that component E_j^f co-propagates with the pump along the positive z-axis direction while E_j^b propagates along the opposite direction, we rewrite Eqs. (1.21) in the form:

$$[\beta-k_{jz}(\boldsymbol{u})]E_j^f(\boldsymbol{u},\beta) = \frac{\omega^2}{\varepsilon_0 c^2}\frac{1}{2k_{jz}(\boldsymbol{u})}P_j^{NL}(\boldsymbol{u},\beta), \tag{1.22a}$$

$$[\beta+k_{jz}(\boldsymbol{u})]E_j^b(\boldsymbol{u},\beta) = -\frac{\omega^2}{\varepsilon_0 c^2}\frac{1}{2k_{jz}(\boldsymbol{u})}P_j^{NL}(\boldsymbol{q},\omega,\beta). \tag{1.22b}$$

We obtain the evolution equations along the z-axis through a back-Fourier transform with respect to β (corresponding to the formal substitution $\beta\rightarrow -i\frac{\partial}{\partial z}$):

$$\frac{\partial}{\partial z}E_j^f(\boldsymbol{u},z) = ik_{jz}(\boldsymbol{u})E_j^f(\boldsymbol{u},z)+i\frac{\omega^2}{2\varepsilon_0 c^2 k_{jz}(\boldsymbol{u})}P_j^{NL}(\boldsymbol{u},z)\ , \tag{1.23a}$$

$$\frac{\partial}{\partial z}E_j^b(\boldsymbol{u},z) = -ik_{jz}(\boldsymbol{u})E_j^b(\boldsymbol{u},z)-i\frac{\omega^2}{2\varepsilon_0 c^2 k_{jz}(\boldsymbol{u})}P_j^{NL}(\boldsymbol{u},z). \tag{1.23b}$$

They describe, as anticipated, the propagation of the two field components along the positive and the negative z-axis directions respectively. Notice that they are coupled through the presence of the nonlinear polarization term at the r.h.s which generally depends on both E_j^f and E_j^b. Before substituting the explicit expression of P^{NL} for the $\chi^{(2)}$ nonlinear medium, it

is convenient extract the "fast" variation along z of the fields variables associated to linear propagation by setting for the signal and the idler field:

$$E_j^f(\boldsymbol{u},z) = \mathcal{E}_j^f(\boldsymbol{u},z)e^{ik_{jz}(\boldsymbol{u})z}, \tag{1.24a}$$

$$E_j^b(\boldsymbol{u},z) = \mathcal{E}_j^b(\boldsymbol{u},z)e^{-ik_{jz}(\boldsymbol{u})z} \qquad j=s,i. \tag{1.24b}$$

Similarly, for the injected pump field we set

$$E_p(\boldsymbol{u}+\boldsymbol{u}',z) = \mathcal{E}_p(\boldsymbol{u}+\boldsymbol{u}',z)e^{ik_{pz}(\boldsymbol{u}+\boldsymbol{u}')z}, \tag{1.25}$$

assuming it propagates only in the forward direction.

The new field variables $\mathcal{E}_p$, $\mathcal{E}_j^f$, and $\mathcal{E}_j^b$ are slowly varying with respect to the z coordinate, since they are only affected by the nonlinear source term at the r.h.s of Eq (1.10) which is assumed to act as a small perturbation to the linear propagation.

In this way we have written the field as the product of two terms: the first one, the carrier term $e^{\pm ik_{jz}(\boldsymbol{u})z}$, is the linear propagation responsible for the fast variation of the field; the second one, $\mathcal{E}_j(\boldsymbol{u},z)$, has a slow variation along z due only to the presence of the nonlinear interaction.

Substituting Eqs. (1.24) into Eqs. (1.23) we obtain the propagation equations for the slow components of the forward and backward propagating signal and idler fields:

$$\frac{\partial}{\partial z}\mathcal{E}_j^f(\boldsymbol{u},z) = +i\frac{\omega^2 e^{-ik_{jz}(\boldsymbol{u})z}}{2\varepsilon_0 c^2 k_{jz}(\boldsymbol{u})}P_j^{NL}(\boldsymbol{u},z), \tag{1.26a}$$

$$\frac{\partial}{\partial z}\mathcal{E}_j^b(\boldsymbol{u},z) = -i\frac{\omega^2 e^{ik_{jz}(\boldsymbol{u})z}}{2\varepsilon_0 c^2 k_{jz}(\boldsymbol{u})}P_j^{NL}(\boldsymbol{u},z), \qquad j=s,i. \tag{1.26b}$$

We now write the the NL polarizations (1.13) in terms of the slow field $\mathcal{E}_j$. For the signal and idler fields we have:

$$\begin{aligned} P_j^{NL}(\boldsymbol{u},z) &= \varepsilon_0\chi^{(2)}(z)\int d\boldsymbol{u}' E_p(\boldsymbol{u}+\boldsymbol{u}',z)E_l^*(z,\boldsymbol{u}') \\ &= \varepsilon_0\chi^{(2)}(z)\int d\boldsymbol{u}' \mathcal{E}_p(\boldsymbol{u}+\boldsymbol{u}',z)\mathcal{E}_l^{f*}(\boldsymbol{u}',z)e^{-i[k_{lz}(\boldsymbol{u}')-k_{pz}(\boldsymbol{u}+\boldsymbol{u}')]z} \qquad (1.27a) \\ &+ \varepsilon_0\chi^{(2)}(z)\int d\boldsymbol{u}' \mathcal{E}_p(\boldsymbol{u}+\boldsymbol{u}',z)\mathcal{E}_l^{b*}(\boldsymbol{u}',z)e^{i[k_{lz}(\boldsymbol{u}')-k_{pz}(\boldsymbol{u}+\boldsymbol{u}')]z} \qquad (1.27b) \end{aligned}$$

Assuming the crystal long with respect to Λ, the nonlinear susceptibility χ^2 is approximately a periodic function of z. Thus, it can be expanded in Fourier series

$$\chi^{(2)}(z) = \sum_n \chi_n e^{ik_n z}, \qquad \text{where } k_n = \frac{2\pi n}{\Lambda} \text{ with } n = 0, \pm 1, \pm 2, \cdots \tag{1.28}$$

being Λ the poling period of the crystal and k_n the wavevector of order n associated to the poling. The nonlinear coefficients χ_n of the Fourier expansion (1.28) can be calculated for example in the most common case of a periodic poling with equal steps [$\chi(z) = 1$ for $0 \leq z \leq \frac{\Lambda}{2}$ and $\chi(z) = -1$ for $\frac{\Lambda}{2} \leq z \leq \Lambda$]:

$$\begin{aligned}
\chi_n &= \frac{1}{\Lambda}\int_0^\Lambda dz \chi(z) e^{-ik_n z} = \frac{1}{\Lambda}\left[\int_0^{\frac{\Lambda}{2}} dz e^{-ik_n z} - \int_{\frac{\Lambda}{2}}^{\Lambda} dz e^{-ik_n z}\right] \\
&= \frac{-i}{2\pi n} e^{-i\pi n}\left(e^{i\frac{\pi n}{2}} - e^{-i\frac{\pi n}{2}}\right)^2 \\
&= \frac{2i}{n\pi} e^{-in\pi} \sin^2\left(\frac{n\pi}{2}\right) = \begin{cases} -\frac{2i}{(2k+1)\pi} & \text{if } n = 2k+1 \\ 0 & \text{if } n = 2k \end{cases}
\end{aligned} \tag{1.29}$$

Substituting the results of Eqs. (1.27-1.28) into Eq. (1.26a) we get the following propagation equations for the forward propagating signal and idler fields

$$\begin{aligned}
\frac{\partial}{\partial z}\mathcal{E}_j^f(\boldsymbol{u}, z) = &+ i\frac{\omega^2}{2c^2 k_{jz}(\boldsymbol{u})} \sum_n \chi_n \int d\boldsymbol{u}' \mathcal{E}_p(\boldsymbol{u}+\boldsymbol{u}', z) \mathcal{E}_l^{f*}(\boldsymbol{u}', z) \\
&\times e^{-i[k_{jz}(\boldsymbol{u}) + k_{lz}(\boldsymbol{u}') - k_{pz}(\boldsymbol{u}+\boldsymbol{u}') - k_n]z} \qquad (1.30a) \\
&+ i\frac{\omega^2}{2c^2 k_{jz}(\boldsymbol{u})} \sum_n \chi_n \int d\boldsymbol{u}' \mathcal{E}_p(\boldsymbol{u}+\boldsymbol{u}', z) \mathcal{E}_l^{b*}(\boldsymbol{u}', z) \\
&\times e^{-i[k_{jz}(\boldsymbol{u}) - k_{lz}(\boldsymbol{u}') - k_{pz}(\boldsymbol{u}+\boldsymbol{u}') - k_n]z}. \qquad (1.30b)
\end{aligned}$$

Similarly, for the backward propagating components we obtain:

$$\begin{aligned}
\frac{\partial}{\partial z}\mathcal{E}_j^b(\boldsymbol{u}, z) = &- i\frac{\omega^2}{2c^2 k_{jz}(\boldsymbol{u})} \sum_n \chi_n \int d\boldsymbol{u}' \mathcal{E}_p(\boldsymbol{u}+\boldsymbol{u}', z) \mathcal{E}_l^{f*}(\boldsymbol{u}', z) \\
&\times e^{-i[-k_{jz}(\boldsymbol{u}) + k_{lz}(\boldsymbol{u}') - k_{pz}(\boldsymbol{u}+\boldsymbol{u}') - k_n]z} \qquad (1.31a) \\
&- i\frac{\omega^2}{2c^2 k_{jz}(\boldsymbol{u})} \sum_n \chi_n \int d\boldsymbol{u}' \mathcal{E}_p(\boldsymbol{u}+\boldsymbol{u}', z) \mathcal{E}_l^{b*}(\boldsymbol{u}', z) \\
&\times e^{-i[-k_{jz}(\boldsymbol{u}) - k_{lz}(\boldsymbol{u}') - k_{pz}(\boldsymbol{u}+\boldsymbol{u}') - k_n]z}. \qquad (1.31b)
\end{aligned}$$

For the forward propagating pump field we have instead four possible source terms coming from the up-conversion of the forward and backward propagating signal and idler fields:

$$\begin{aligned}\frac{\partial}{\partial z}\mathcal{E}_p(\boldsymbol{u},z) = i\frac{\omega^2}{2c^2k_{pz}(\boldsymbol{u})}\sum_n \chi_n \int d\boldsymbol{u}'\mathcal{E}_s^f(\boldsymbol{u}',z)\mathcal{E}_i^f(\boldsymbol{u}-\boldsymbol{u}',z)e^{[ik_{sz}(\boldsymbol{u})+ik_{iz}(\boldsymbol{u}-\boldsymbol{u}')-ik_{pz}(\boldsymbol{u})+k_n]z} \\ \times \mathcal{E}_s^f(\boldsymbol{u}',z)\mathcal{E}_i^b(\boldsymbol{u}-\boldsymbol{u}',z)e^{[ik_{sz}(\boldsymbol{u})-ik_{iz}(\boldsymbol{u}-\boldsymbol{u}')-ik_{pz}(\boldsymbol{u})+k_n]z} \\ \times \mathcal{E}_s^b(\boldsymbol{u}',z)\mathcal{E}_i^f(\boldsymbol{u}-\boldsymbol{u}',z)e^{[-ik_{sz}(\boldsymbol{u})+ik_{iz}(\boldsymbol{u}-\boldsymbol{u}')-ik_{pz}(\boldsymbol{u})+k_n]z} \\ \times \mathcal{E}_s^b(\boldsymbol{u}',z)\mathcal{E}_i^b(\boldsymbol{u}-\boldsymbol{u}',z)e^{[-ik_{sz}(\boldsymbol{u})-ik_{iz}(\boldsymbol{u}-\boldsymbol{u}')-ik_{pz}(\boldsymbol{u})+k_n]z}\end{aligned} \tag{1.32}$$

We ignore the possibility of the generation of a counterpropagating pump field coming from the up-conversion of signal and idler fields since we neglect second order effects. We shall now focus on the case of interest, the counterpropagating geometry, and make the approximation which consists keeping only the highest order terms at the r.h.s. of Eqs. (1.30-1.32), since higher order harmonics have smaller and smaller amplitudes [see example (1.29) for the simple poling, where $\chi_n \propto 1/n$]. This amount to approximate the square-shaped periodic function $\chi^{(2)}(z) \approx \chi_{+1}e^{+ik_G z} + \chi_{-1}e^{-ik_G z}$.

1.3 The counterpropagating geometry

As illustrated qualitatively in Sec. 1.1, the counterpropagating configuration requires a poling period on the order of the pump wavelength inside the material, i.e. with $\Lambda \approx \lambda_0$ or

$$k_{n=1} \equiv k_G = \frac{2\pi}{\Lambda} \approx k_p. \tag{1.33}$$

Notice that the pump central frequency ω_p and the crystal poling period Λ univocally determine the quasi-phasematched frequencies of the signal and idler fields along the collinear direction, ω_s and $\omega_i = \omega_p - \omega_s$, solution of the equation

$$k_{sz}(q=0,\omega_s) - k_{iz}(q=0,\omega_p-\omega_s) - k_{pz}(\omega_p, q=0) + k_G = 0. \tag{1.34}$$

While condition (1.33) allows for solutions of this *forward-backward* quasiphasematching condition within the crystal transparency range, the analogous conditions for *forward-forward* and *backward-backward* emission are never satisfied except for extreme wavelengths in the UV and in the far infrared. It is thus legitimate to drop of the corresponding source terms at the r.h.s. of Eqs. (1.30-1.32). We keep accordingly only the $n=-1$ terms of the $\chi^{(2)}$ expansion in the signal and idler propagation equations and the $n=1$ term in the pump

propagation equation, obtaining

$$\frac{\partial}{\partial z}\mathcal{E}_s^f(\boldsymbol{q},\Omega,z) = +i\frac{(\omega_s+\Omega)^2}{2c^2k_{sz}(\boldsymbol{q},\Omega)}\chi_{-1}\int d\boldsymbol{q}'d\Omega'\mathcal{E}_p(\boldsymbol{q}+\boldsymbol{q}',\Omega+\Omega',z)\mathcal{E}_i^{b*}(\boldsymbol{q}',\Omega',z) \times e^{-iD(\boldsymbol{q},\boldsymbol{q}',\Omega,\Omega')z} \tag{1.35a}$$

$$\frac{\partial}{\partial z}\mathcal{E}_i^b(\boldsymbol{q},\Omega,z) = -i\frac{(\omega_i+\Omega)^2}{2c^2k_{iz}(\boldsymbol{q},\Omega)}\chi_{-1}\int d\boldsymbol{q}'d\Omega'\mathcal{E}_p(\boldsymbol{q}+\boldsymbol{q}',\Omega+\Omega',z)\mathcal{E}_s^{f*}(\boldsymbol{q}',\Omega',z) \times e^{-iD(\boldsymbol{q}',\boldsymbol{q},\Omega',\Omega)z} \tag{1.35b}$$

$$\frac{\partial}{\partial z}\mathcal{E}_p(\boldsymbol{q},\Omega,z) = +i\frac{(\omega_p+\Omega)^2}{2c^2k_{pz}(\boldsymbol{q},\Omega)}\chi_{+1}\int d\boldsymbol{q}'d\Omega'\mathcal{E}_s^f(\boldsymbol{q}',\Omega',z)\mathcal{E}_i^b(\boldsymbol{q}-\boldsymbol{q}',\Omega-\Omega',z) \times e^{iD(\boldsymbol{q}',\boldsymbol{q}-\boldsymbol{q}',\Omega',\Omega-\Omega')z}. \tag{1.35c}$$

where Ω denotes the frequency offset from the respective reference frequencies ω_s, ω_i and $\omega_p = \omega_s + \omega_i$ satisfying condition (1.34) and we introduced the quasi-phase matching function

$$D(\boldsymbol{q},\boldsymbol{q}',\Omega,\Omega') = k_{sz}(\boldsymbol{q},\Omega) - k_{iz}(\boldsymbol{q}',\Omega') - k_{pz}(\boldsymbol{q}+\boldsymbol{q}',\Omega+\Omega') + k_G, \tag{1.36}$$

characterizing the counterpropagating geometry.

1.4 Quantization of the electromagnetic field

We shall now move to the quantum description of the process. For this section we basically follow the approach by Loudon [29], which consider only two dimensions for the electric field, and the work by Caspani [28], which consider a full 3D model including also the transverse dimension of the field. Although in our work we will mostly consider the collinear geometry, thus neglecting the spatial degrees of freedom we will keep for now the discussion general considering both the spatial and the temporal degrees of freedom. Moreover we consider only the linear properties of the medium in order to pass from the classical electromagnetic field to annihilation-creation operators, assuming that the nonlinearities do not affect significantly the quantization. In order to do this the electromagnetic field operator is written as a superposition of creation and annihilation operators. It is shown in [28] that we can obtain the quantized propagation equations for the field operators with the formal substitution:

$$E_j^{f,b}(\boldsymbol{w},z) \to \hat{E}_j^{f,b}(\boldsymbol{w},z) = i\sqrt{\frac{\hbar(\omega_j+\Omega)^2}{2\varepsilon_0c^2k_{jz}(\boldsymbol{w})}}\hat{A}_j^{f,b}(\boldsymbol{w},z), \tag{1.37}$$

where $j = s,i$, $\hat{a}$ is the photon operator and $\boldsymbol{w} = (\boldsymbol{q},\Omega)$. Eq. (1.37) with respect to the fields obtained by extracting the linear propagation, becomes:

$$\mathcal{E}_j^{f,b}(\boldsymbol{w},z) \to \hat{\mathcal{E}}_j^{f,b}(\boldsymbol{w},z) = i\sqrt{\frac{\hbar(\omega_j+\Omega)^2}{2\varepsilon_0 c^2 k_{jz}(\boldsymbol{w})}}\hat{a}_j^{f,b}(\boldsymbol{w},z), \tag{1.38}$$

where

$$\hat{A}_j^{f,b}(\boldsymbol{w},z) = \hat{a}_j^{f,b}(\boldsymbol{w})e^{\pm ik_{jz}(\boldsymbol{w})z}. \tag{1.39}$$

The quantized version of Eq. (1.35) can be obtained using the relation (1.38). We obtain for the forward fields ($j,l = s,i$, $j \neq l$):

$$\frac{\partial}{\partial z}\hat{a}_{j+}(\boldsymbol{w},z) = +\frac{\chi_{-1}}{2c^3}\sqrt{\frac{\hbar}{2\varepsilon_0}}\int d\boldsymbol{w}' C(\boldsymbol{w},\boldsymbol{w}')\hat{a}_p(\boldsymbol{w}+\boldsymbol{w}',z)\hat{a}_{l+}^{\dagger}(\boldsymbol{w}',z)e^{-iD(\boldsymbol{w},\boldsymbol{w}')z}. \tag{1.40}$$

and, similarly, for the backward fields

$$\frac{\partial}{\partial z}\hat{a}_{j-}(\boldsymbol{w},z) = -\frac{\chi_{-1}}{2c^3}\sqrt{\frac{\hbar}{2\varepsilon_0}}\int d\boldsymbol{w}' C(\boldsymbol{w},\boldsymbol{w}')\hat{a}_p(\boldsymbol{w}+\boldsymbol{w}',z)\hat{a}_{l+}^{\dagger}(\boldsymbol{w}',z)e^{-iD(\boldsymbol{w}',\boldsymbol{w})z}. \tag{1.41}$$

where we have introduced the coupling coefficient C, defined by the relation:

$$C(\boldsymbol{w},\boldsymbol{w}') = \sqrt{\frac{(\omega_p+\Omega+\Omega')^2(\Omega_s+\Omega)^2(\omega_i+\Omega')^2}{k_{pz}(\boldsymbol{w}+\boldsymbol{w}')k_{sz}(\boldsymbol{w})k_{iz}(\boldsymbol{w}')}}. \tag{1.42}$$

Following the approach in [28] we shall reduce the coefficient to a constant in order to simplify the calculations. It is possible to expand the coefficient C in power series of Ω/ω_s and q/k_s, where Ω is the frequency offset from the central frequencies ω_s and ω_i. We can expand the coefficient (1.42) obtaining at the first order:

$$\begin{aligned} C(\boldsymbol{w},\boldsymbol{w}') &= \sqrt{\frac{(\omega_p+\Omega+\Omega')^2(\omega_s+\Omega)^2(\omega_i+\Omega')^2}{k_{pz}(\boldsymbol{q}+\boldsymbol{q}',\omega_s+\omega_i+\Omega+\Omega')k_{sz}(\boldsymbol{q},\omega_s+\Omega)k_{iz}(\boldsymbol{q}',\omega_i+\Omega')}} \\ &= \sqrt{\frac{\omega_p^2\omega_s^2\omega_i^2}{k_pk_sk_i}}\left[1+\mathcal{O}\left(\frac{\Omega}{\omega_s},\frac{\boldsymbol{q}}{k_s}\right)\right] \\ &\approx \sqrt{\frac{c^3\omega_p\omega_s\omega_i}{n_pn_sn_i}} \end{aligned} \tag{1.43}$$

The coefficient, under this approximation, is constant and can be taken out from the integral. This approximation is valid for small bandwidths, i.e. for $\frac{\Omega}{\omega_s},\frac{\Omega'}{\omega_i} \ll 1$ (note that the condition

$\frac{\Omega}{\omega_s}$ is almost always valid, except for ultrashort pulses with durations of few femtoseconds) and for small angles, i.e. $\frac{q_s}{k_s}, \frac{q_i}{k_i} \ll 1$.

The coupling coefficient results

$$\bar{\sigma}_{\pm 1} = \frac{\chi_{\pm 1}}{2c^3}\sqrt{\frac{\hbar}{2\varepsilon_0}}C = \chi_{\pm 1}\sqrt{\frac{\hbar}{8\varepsilon_0 c^3}\frac{\omega_p\omega_s\omega_i}{n_p n_s n_i}}, \tag{1.44}$$

where $\chi = \chi_{+1} = -\chi_{-1}$.

From Eqs. (1.40,1.41) we thus obtain:

$$\frac{\partial}{\partial z}\hat{a}_{s+}(\boldsymbol{w},z) = +\bar{\sigma}_{-1}\int d\boldsymbol{w'}\hat{a}_p(\boldsymbol{w}+\boldsymbol{w'},z)\hat{a}^\dagger_{i-}(\boldsymbol{w'},z)e^{-iD(\boldsymbol{w},\boldsymbol{w'})z} \tag{1.45a}$$

$$\frac{\partial}{\partial z}a_{i-}(\boldsymbol{w},z) = -\bar{\sigma}_{-1}\int d\boldsymbol{w'}\hat{a}_p(\boldsymbol{w}+\boldsymbol{w'},z)\hat{a}^\dagger_{s+}(\boldsymbol{w'},z)e^{-iD(\boldsymbol{w'},\boldsymbol{w})z} \tag{1.45b}$$

$$\frac{\partial}{\partial z}\hat{a}_{p+}(\boldsymbol{w},z) = -\bar{\sigma}_{1}\int d\boldsymbol{w'}\hat{a}_{s+}(\boldsymbol{w'},z)\hat{a}_{i-}(\boldsymbol{w}-\boldsymbol{w'},z)e^{iD(\boldsymbol{w'},\boldsymbol{w}-\boldsymbol{w'})z} \tag{1.45c}$$

where, according to Eqs.(1.28, 1.43), the coupling coefficients are defined as:

$$\bar{\sigma}_1 = -i\sigma, \quad \bar{\sigma}_{-1} = i\sigma, \quad \sigma = \frac{1}{2\pi}\sqrt{\frac{\hbar}{8\varepsilon_0 c^3}\frac{\omega_p\omega_i\omega_s}{n_p n_s n_i}}|\chi|. \tag{1.46}$$

By making the unitary transformation for the field operators $\hat{a}_{j\pm}(\boldsymbol{w},z) \to i\hat{a}_{j\pm}(\boldsymbol{w},z)$ we get finally:

$$\frac{\partial}{\partial z}\hat{a}_{s+}(\boldsymbol{w},z) = +\sigma\int d\boldsymbol{w'}\hat{a}_p(\boldsymbol{w}+\boldsymbol{w'},z)\hat{a}^\dagger_{i-}(\boldsymbol{w'},z)e^{-iD(\boldsymbol{w},\boldsymbol{w'})z} \tag{1.47a}$$

$$\frac{\partial}{\partial z}\hat{a}_{i-}(\boldsymbol{w},z) = -\sigma\int d\boldsymbol{w'}\hat{a}_p(\boldsymbol{w}+\boldsymbol{w'},z)\hat{a}^\dagger_{s+}(\boldsymbol{w'},z)e^{-iD(\boldsymbol{w'},\boldsymbol{w})z} \tag{1.47b}$$

$$\frac{\partial}{\partial z}\hat{a}_{p+}(\boldsymbol{w},z) = -\sigma\int d\boldsymbol{w'}\hat{a}_{s+}(\boldsymbol{w'},z)\hat{a}^\dagger_{i-}(\boldsymbol{w}-\boldsymbol{w'},z)e^{iD(\boldsymbol{w'},\boldsymbol{w}-\boldsymbol{w'})z}. \tag{1.47c}$$

These are the equations that rule the propagation of signal, idler and pump field in a periodically poled crystal in the counterpropagating configuration. Our work is mainly devoted to the analysis of these equations under the MOPO threshold. In this regime the depletion of the pump beam can be neglected and the pump approximated by a constant c-number field, corresponding to the pump pulse at the crystal input face. The strength of the parametric coupling is then described by the dimensionless gain parameter:

$$g = \sqrt{\sigma}\alpha_p(t=0)l_c \tag{1.48}$$

where $\alpha_p(t=0)$ is the peak value of the pump temporal profile. In the following chapters we will analyze these equations mainly in two different parametric regimes under the MOPO threshold:

- The regime of spontaneous pair production ($g \ll 1$), where the feedback mechanism in negligible. Here we shall follow a perturbative approach (g being the perturbative parameter) and find a solution up to first order in g. The analysis in mainly devoted to the description of the finite pump effects on the twin photon coherence and correlation and to the determination of the degree of entanglement of the quantum states.

- The regime of stimulated pair production, including also the region close to the MOPO threshold, where the effect of the feedback mechanism plays a determinant role. Here it is possible to find an analytical solution in the form of input-output relations considering a monochromatic plane wave pump. The analysis is mainly devoted to the investigation of the temporal coherence and correlation in the transition from below to above threshold.

In Chap. VI we will also consider the gain regime above the MOPO threshold, where some preliminary numerical results are shown.

In the following we shall consider only collinear propagation, either assuming that light is collected only at small propagation angles with respect to the pump, or because of a waveguiding configuration. Spatial correlations will be discussed only in Chap. VII.

Chapter 2

The classical model and the MOPO threshold

In this Chapter we basically derive the results for the classical model of the MOPO obtained by Y. Ding anf J. Khurgin in [27]. With this simple model, considering a CW pump, one can demonstrate the existence of a threshold above wich PDC emission occurs in absence of injected signal and idler fields.

2.1 The classical model

The classical counterpart of the quantum model (1.47) can be obtained by formally replacing the fields operators $\hat{a}_i$ in Eqs. (1.47) with c-number fields, $\hat{a}_i \to \alpha_i$, which corresponds to consider $\hat{a}_i = \alpha_i + \delta\hat{a}_i$ and to neglect the quantum fluctuations $\delta\hat{a}_i$. In this way one obtains propagation equations for the c-number fields $\alpha_j(\Omega, z)$ which are formally identical to Eqs. (1.47). In order to recast them in a form which is more familiar in literature, see e.g. [16, 12], we rather consider the fields:

$$\beta_s(z,\Omega) = e^{i[k_s(\Omega)-k_s]z}\alpha_s, \tag{2.1a}$$

$$\beta_i(z,\Omega) = e^{-i[k_i(\Omega)-k_i]z}\alpha_i, \tag{2.1b}$$

$$\beta_p(z,\Omega) = e^{i[k_p(\Omega)-k_p]z}\alpha_p. \tag{2.1c}$$

Then we assume that the effects of second and higher order dispersion are negligible with respect to the first order (approximation valid for the MOPO)

$$k_j(\Omega) - k_j = k'_j\Omega + \frac{1}{2}k''_j\Omega^2 + \ldots \approx \frac{1}{v_{gj}}\Omega, \tag{2.2}$$

where derivatives k_j', k_j'', etc. are calculated at the central frequencies ω_j and $v_{gj} = 1/k_j'$ are the group velocities of the three waves. By back-transforming to the temporal domain $\beta_j(z,t) = \int \frac{d\Omega}{\sqrt{2\pi}} \beta_j(z,\Omega) e^{-i\Omega t}$, the classical propagation equations take the form:

$$\frac{\partial \beta_s(z,t)}{\partial z} + \frac{1}{v_{gs}} \frac{\partial \beta_s(z,t)}{\partial t} = \bar{\sigma} \beta_p(z,t) \beta_i^*(z,t) \tag{2.3a}$$

$$\frac{\partial \beta_i(z,t)}{\partial z} - \frac{1}{v_{gi}} \frac{\partial \beta_i(z,t)}{\partial t} = -\bar{\sigma} \beta_p(z,t) \beta_s^*(z,t) \tag{2.3b}$$

$$\frac{\partial \beta_p(z,t)}{\partial z} + \frac{1}{v_{gp}} \frac{\partial \beta_p(z,t)}{\partial t} = -\bar{\sigma} \beta_s(z,t) \beta_i(z,t) \tag{2.3c}$$

Considering the case of a CW pump field, a non trivial stationary solution with no injected signal and idler fields, i.e. satisfying the boundary conditions (see Fig. 2.1)

$$\beta_s(z = 0, t) = 0, \tag{2.4a}$$

$$\beta_i(z = l_c, t) = 0. \tag{2.4b}$$

is known to exist [27] (see next section for a derivation).

The distributed feedback mechanism characterizing the counter-prropagating geometry is indeed responsible of the establishment of coherent oscillations above threshold. In contrast, within the classical description the copropagating configuration always requires the injection of a signal of frequency ω_s lower than ω_p in order to trigger the process of parametric amplification.

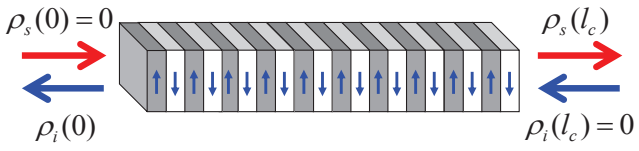

Fig. 2.1 Schematic representations of the MOPO configuration in the classical model. Notice that there are no injected signal and idler fields.

2.2 The stationary solution and the MOPO threshold

In this section we basically derive the results obtained by Y. Ding anf J. Khurgin in [27], looking for a non trivial stationary solution of Eqs. (2.3) that satisfies the boundary conditions

(2.4). Separating the real and the imaginary part of the fields $\beta_j(z) = \rho_j(z)e^{i\phi_j(z)}$ we get the following propagation equations for the ampitudes $\rho_j(z)$ and the phases $\phi_j(z)$:

$$\frac{d\rho_s(z)}{dz} = \bar{\sigma}\rho_p(z)\rho_i(z)\cos\Theta(z), \tag{2.5a}$$
$$\frac{d\rho_i(z)}{dz} = -\bar{\sigma}\rho_p(z)\rho_s(z)\cos\Theta(z), \tag{2.5b}$$
$$\frac{d\rho_p(z)}{dz} = -\bar{\sigma}\rho_s(z)\rho_i(z)\cos\Theta(z), \tag{2.5c}$$

and the phases $\phi_j(z)$

$$\frac{d\phi_s}{dz} = \bar{\sigma}\frac{\rho_p(z)\rho_i(z)}{\rho_s(z)}\sin\Theta(z), \tag{2.6a}$$
$$\frac{d\phi_i}{dz} = -\bar{\sigma}\frac{\rho_p(z)\rho_s(z)}{\rho_i(z)}\sin\Theta(z), \tag{2.6b}$$
$$\frac{d\phi_p}{dz} = \bar{\sigma}\frac{\rho_s(z)\rho_i(z)}{\rho_p(z)}\sin\Theta(z), \tag{2.6c}$$

where $\Theta(z) = \phi_s(z) + \phi_i(z) - \phi_p(z)$. From the equations for the intensities (2.5) we get the Manley-Rowe relations for the counterpropagating twin beams:

$$\frac{d}{dz}[\rho_s^2(z) + \rho_i^2(z)] = 0 \quad \rightarrow \quad \rho_s^2(z) + \rho_i^2(z) = c_1 \tag{2.7a}$$
$$\frac{d}{dz}[\rho_p^2(z) + \rho_s^2(z)] = 0 \quad \rightarrow \quad \rho_p^2(z) + \rho_s^2(z) = c_2 \tag{2.7b}$$
$$\frac{d}{dz}[\rho_p^2(z) - \rho_i^2(z)] = 0 \quad \rightarrow \quad \rho_p^2(z) - \rho_i^2(z) = c_3, \tag{2.7c}$$

with c_1, c_2, c_3 real constants, $c_1 + c_2 = c_3$.

From the boundaries $\rho_s(z = 0) = 0$, $\rho_i(z = l_c) = 0$ we can determine the constants c_1, c_2, c_3 and the Manley-Rowe relations (2.7) become:

$$\rho_s^2(z) + \rho_i^2(z) = \rho_s^2(l_c) = \rho_i^2(0) \tag{2.8a}$$
$$\rho_p^2(z) + \rho_s^2(z) = \rho_p^2(0) \tag{2.8b}$$
$$\rho_p^2(z) - \rho_i^2(z) = \rho_p^2(l_c). \tag{2.8c}$$

Another integration constant is given by

$$\Gamma(z) = \bar{\sigma}\rho_s(z)\rho_i(z)\rho_p(z)\sin\Theta(z), \tag{2.9}$$

since we have:

$$\begin{aligned}\frac{d\Gamma(z)}{dz} &= \bar{\sigma}\sin\Theta(z)\frac{d}{dz}[\rho_s(z)\rho_i(z)\rho_p(z)] - \bar{\sigma}\cos\Theta(z)\frac{d\Theta(z)}{dz}\rho_s(z)\rho_i(z)\rho_p(z)\\ &= \bar{\sigma}\sin\Theta(z)\frac{d}{dz}[\rho_s(z)\rho_i(z)\rho_p(z)]\\ &\quad - \bar{\sigma}\cos\Theta(z)\left[\frac{1}{\text{cotan}\Theta(z)}\frac{1}{\rho_s\rho_i\rho_p}\frac{d}{dz}[\rho_s(z)\rho_i(z)\rho_p(z)]\right]\times\rho_s(z)\rho_i(z)\rho_p(z)\\ &= \bar{\sigma}\sin\Theta(z)\frac{d}{dz}[\rho_s(z)\rho_i(z)\rho_p(z)] - \bar{\sigma}\sin\Theta(z)\frac{d}{dz}[\rho_s(z)\rho_i(z)\rho_p(z)] = 0.\end{aligned}$$

From the boundaries $\Gamma(z=0)=\Gamma(z=l_c)=0$, thus we can write

$$\Gamma(z) = \bar{\sigma}\rho_s(z)\rho_i(z)\rho_p(z)\sin\Theta(z) = 0,\ \forall z. \tag{2.10}$$

For $\sin\Theta(z)\neq 0$ this equation is satified only by the trivial solution $\rho_s(z)=\rho_i(z)=0$, $\forall z$. A non trivial solution with non vanishing signal and idler fields exists only for $\sin\Theta(z)=0$, i.e. $\Theta(z)=n\pi$ for all z so that $\cos\Theta(z)=\pm 1$ and Eqs.(2.5) become

$$\frac{d\rho_s(z)}{dz} = +\sigma\rho_p(z)\rho_i(z) > 0, \tag{2.11a}$$

$$\frac{d\rho_i(z)}{dz} = -\sigma\rho_p(z)\rho_s(z) < 0, \tag{2.11b}$$

$$\frac{d\rho_p(z)}{dz} = -\sigma\rho_s(z)\rho_i(z) < 0, \tag{2.11c}$$

since we need $+$ sign in the signal equation and $-$ sign in the idler one in order to have amplification. Eqs. 2.6 become

$$\frac{d\phi_p(z)}{dz} = \frac{d\phi_s(z)}{dz} = \frac{d\phi_i(z)}{dz} = 0. \tag{2.12}$$

since From Eq.(2.11) we see that the three fields involved in the parametric process have constant phases along the crystal length, these being linked by the relation

$$\Theta = \phi_s + \phi_i - \phi_p = 2k\pi. \tag{2.13}$$

From (2.11) we see that ρ_s increases monotonically from 0 to l_c while ρ_i, ρ_p decrease with $\rho_s^2+\rho_i^2$ remaining constant. Expressing the product $\rho_p\rho_i$ as a function of ρ_s in the equation

for the signal amplitude, thanks to relation (2.8) we obtain the following closed equation

$$\frac{d\rho_s(z)}{dz} = \bar{\sigma}\sqrt{\rho_p^2(0)-\rho_s^2(z)}\sqrt{\rho_s^2(l_c)-\rho_s^2(z)}, \tag{2.14}$$

which can be integrated by separating ρ_s from the independent variable z [taking into account the condition $\rho_s(z=0)=0$]:

$$\bar{\sigma}z = \int_0^{\rho_s} \frac{d\rho_s'}{\sqrt{\rho_p^2(0)-\rho_s'^2(z)}\sqrt{\rho_s^2(l_c)-\rho_s'^2(z)}}. \tag{2.15}$$

This equation provides the intensity of the signal field ρ_s as a function of z in an implicit form. It is however important to notice that this solution exists only when the injected pump amplitude $\rho_p^{\text{in}} := \rho_p(z=0)$ exceeds a given threshold value ρ_p^{th}. This is best seen by making the change for the integration variable in Eq. (2.15) $\rho_s'(z) = \rho_s(l_c)\sin\theta(z)$, $0 \le \theta \le \pi/2$, with $\theta = 0$ for $z = 0$ and $\theta = \pi/2$ for $z = l_c$, by which we obtain:

$$\begin{aligned}
\bar{\sigma}z &= \int_0^{\theta(z)} \frac{\rho_s(l_c)\cos\theta' d\theta'}{\sqrt{\rho_p^2(0)-\rho_s^2(l_c)\sin^2\theta'}\sqrt{\rho_s^2(l_c)-\rho_s^2(l_c)\sin^2\theta'}} \\
\bar{\sigma}\rho_p(0)z &= \int_0^{\theta(z)} \frac{d\theta'}{\sqrt{1-\eta\sin^2\theta'}},
\end{aligned} \tag{2.16a}$$

where we introduced the pump depletion parameter

$$\eta = \frac{\rho_s^2(l_c)}{\rho_p^2(0)} = 1 - \frac{\rho_p^2(l_c)}{\rho_p^2(0)}, \qquad (0 \le \eta \le 1). \tag{2.17}$$

Setting $z = l_c$ in Eq. (2.16a) and introducing the dimensionless gain parameter $\bar{\sigma}\rho_p^{in}l_c$, where $\rho_p^{in} = \rho_p(0)$, we rewrite Eq. (2.16a) as

$$g = \int_0^{\pi/2} \frac{d\theta'}{\sqrt{1-\eta\sin^2\theta'}} := K(\eta), \tag{2.18}$$

where the function $K(\eta)$ at the r.h.s is the complete Jacobi elliptic integral of the first kind [31]. $K(\eta)$ is larger than $\pi/2$ for positive values of η, thus a non trivial stationary solution exists provided that the dimensionless gain parameter

$$g = \bar{\sigma}\rho_p^{in}l_c \;>\; g^{thr} = \frac{\pi}{2}. \tag{2.19}$$

It is now possible to express the non trivial solution (2.18) in terms of the Jacobi elliptic functions sn e cn. Considering the incomplete Jacobi elliptic integral

$$u = \int_0^{\phi} \frac{d\phi'}{\sqrt{1-\eta\sin^2\phi'}}, \tag{2.20}$$

the sn e cn functions are defined according to the relations:

$$\mathrm{sn}[u,\eta] = \sin\phi, \quad \mathrm{cn}[u,\eta] = \cos\phi. \tag{2.21}$$

For a given value of $g = \bar{\sigma}\rho_p^{in} l_c$ above the $\pi/2$ threshold, we have according to Eq. (2.16a):

$$\sin\theta(z) = \mathrm{sn}[\bar{\sigma}\rho_p^{in} z, \eta] = \mathrm{sn}[gz/l_c, K^{-1}(g)] \tag{2.22a}$$

$$\cos\theta(z) = \mathrm{cn}[\bar{\sigma}\rho_p^{in} z, \eta] = \mathrm{cn}[gz/l_c, K^{-1}(g)]. \tag{2.22b}$$

Calling ρ_p^{thr} the pump amplitude corresponding to the threshold value, i.e. such that $\bar{\sigma}\rho_p^{thr} = \pi/2$ we have $\rho_p^{in}/\rho_p^{thr} = 2g/\pi$ and from Eq. (2.17) we have

$$\rho_s^2(l_c) = \eta(\rho_p^{in})^2 = K^{-1}(g)(\rho_p^{in})^2 \tag{2.23a}$$

$$\left[\frac{\rho_s(l_c)}{\rho_p^{thr}}\right]^2 = K^{-1}(g)\frac{4g^2}{\pi^2}. \tag{2.23b}$$

It is possible now to write the solution for the evolution of the photon flux densities $I_j(z) \equiv \rho_j^2(z)$, $j = s,i,p$ normalized to the pump threshold value $I_p^{th} \equiv (\rho_p^{th})^2$:

$$\frac{I_s(z)}{I_p^{th}} = \frac{4g^2}{\pi^2}K^{-1}(g)\mathrm{sn}^2[gz/l_c, K^{-1}(g)] \tag{2.24a}$$

$$\frac{I_i(z)}{I_p^{th}} = \frac{4g^2}{\pi^2}K^{-1}(g)\mathrm{cn}^2[gz/l_c, K^{-1}(g)] \tag{2.24b}$$

$$\frac{I_p(z)}{I_p^{th}} = \frac{4g^2}{\pi^2}(1 - K^{-1}(g)\mathrm{sn}^2[gz/l_c, K^{-1}(g)]) \tag{2.24c}$$

Solutions (2.24) are plotted in Fig. 2.2. We find that the classical model with a CW pump predicts that PDC emission occurs above the MOPO threshold $g = \pi/2$, in absence of injected signal and idler fields. In this work we are interested in the quantum properties of the PDC field generated from vacuum fluctuations below the threshold (for $g < \pi/2$), where the classical description predicts that the signal and idler waves are identically equal to zero. To

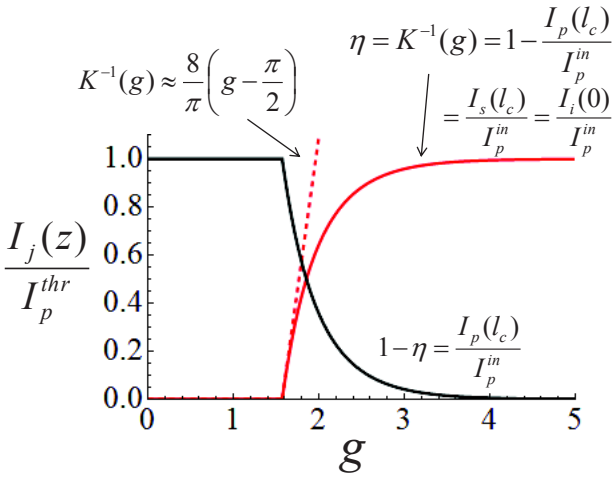

Fig. 2.2 Conversion efficiency and pump depletion of the MOPO as a function of the parametric gain g evaluated from Eq. (2.24). The classical model with a CW pump predicts that PDC emission occurs above the MOPO threshold $g = \pi/2$.

this end, we introduce in the next chapter the linearized model that describes the quantized PDC field in the undepleted CW pump regime.

2.3 Review of experimental findings

Because of the technical difficulties involved in the fabrication of periodically poled crystal with the required submicrometric poling period [14, 15], only few experimental results have been obtained until now. Only in the 2007 the first experimental realization of a MOPO was performed by C. Canalias and V. Pasiskevicius [1], and it was further investigated in [12] and [32].

In this section we will give a short review of the main experimental results obtained in the work by the group of C. Canalias.

In [1] they demonstrated the existence of a threshold for the pump intensity beyond which the system starts to oscillate coherently and a substantial fraction of the pump energy is down-converted into narrowband signal and idler fields (see Fig. 2.4). In order to do that a PPKTP sample with a poling period of 800 nm was fabricated (see Fig. 2.3) and pump pulses of several tens of picosenconds . The pump light propagated along the crystal X axis and was polarized parallel to the crystal Z axis so that the highest nonlinear coefficient, $d33$, could be exploited (see Fig. 2.5). The pump wavelength was 821.4 nm, the MOPO generated signal was at 1139.7 nm, and the idler at 2940.8 nm.

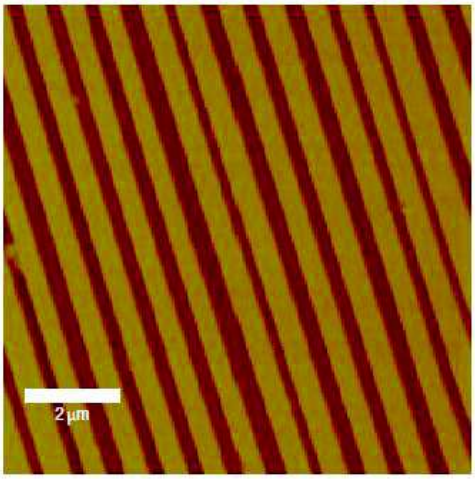

Fig. 2.3 Atomic force microscope image of the chemically etched z surface of the PPKTP crystal used in the work by Canalias, *et al*. [1].

They also pointed out that beyond threshold the co-propagating signal field is essentially a wavelength-shifted replica of the pump spectrum, while the bandwidth of the counterpropagating idler field is two orders of magnitude narrower than that of the pump. In [12] the

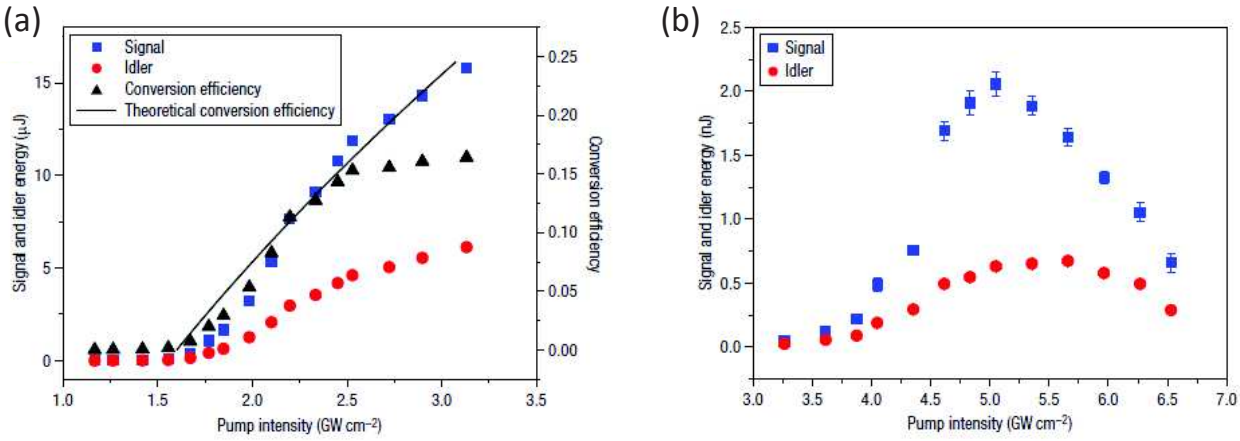

Fig. 2.4 Experimental results in [1]. (a), Dependence of the MOPO signal (blue squares) and idler (red circles) energy and energy conversion efficiency (black triangles) on the pump intensity for a 47 – *ps* pump pulse. The black curve shows the theoretical conversion efficiency. (b), Dependence of the optical parametric generation signal (blue squares) and idler (red circles) energy on the pump intensity for a 21 – *ps* pump pulse.

influence of the pump bandwidth on the MOPO operation is experimentally studied by pumping a PPKTP crystal with linearly-chirped pulses of bandwidths up to 4 THz, showing that a

broader pump spectrum decreases the conversion efficiency. Other pumping configurations are then studied, showing that a MOPO may operate even when the pump is incoherent with a phase modulation that varies randomly throughout the pulse. Regardless if the phase modulation in the pump is deterministic or stochastic, the backward parametric wave always has a bandwidth that is narrow compared to that of the forward wave. This effect is especially pronounced if the pump wavelength and the modulation period of the nonlinear medium are chosen so that the group velocities of the pump and the forward wave are exactly matched.

In [32] an experimental demonstration of self-established noncollinear interactions in a quasi-phase-matched MOPO is given. Self-establishes oscillation takes place in a very specific geometric configuration where the two possible signal-idler solutions of the energy and momentum conservation conditions become spatially degenerate and contribute coherently to the parametric gain.

For our numerical simulations we consider mainly the same configuration used in [1], i.e. a periodically poled Potassium titanyl phosphate (PPKTP) crystal in the type 0 $e-ee$ phase-matching geometry. The fields are polarized along the Z principal axis of the crystal. The pump is injected along the z-axis of the laboratory frame, which coincides with the X principal axis, as shown in Fig.(2.5).

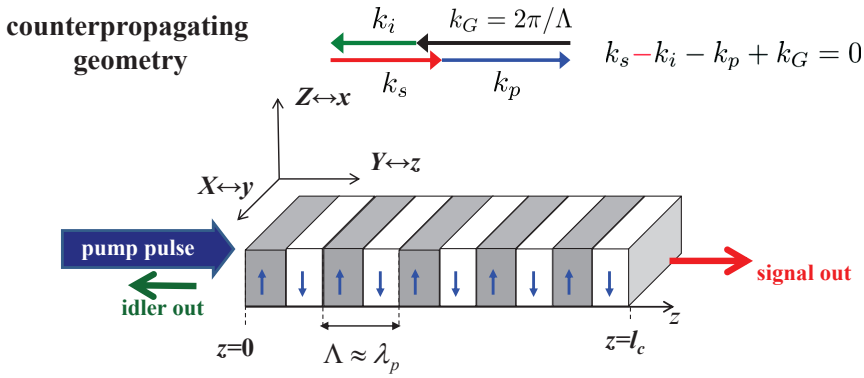

Fig. 2.5 Schematic representations of the PDC process in a KTP crystal in the counterpropagating geometry. The fields are polarized along the Z principal axis of the crystal. The pump is injected along the z-axis of the laboratory frame, which coincides with the X principal axis.

Chapter 3

Spontaneous pair production regime

In this chapter we focus on the regime of spontaneous photon pairs production, well below threshold, and analyze the temporal quantum properties of counterpropagating twin photons generated in a purely collinear configuration. We provide a detailed theoretical analysis of the effects of the spectral properties of the pump laser on the degree of entanglement of the state, identify the physical conditions under which the state may become separable, and provide a consistent interpretation of the transition from an entangled to a separable state.

As already mentioned we restrict our analysis to a purely temporal description: we consider only collinear propagation, either assuming that a small angular bandwidth is collected and the process is characterized by a single spatial mode operation, or because of a waveguiding configuration.

The coupled equations of propagation (1.47) can be written as

$$\frac{\partial}{\partial z}\hat{a}_s(\Omega,z) = \sigma \int d\Omega' \hat{a}_p(\Omega+\Omega',z)\hat{a}_i^\dagger(\Omega',z)e^{-iD(\Omega,\Omega')z}, \tag{3.1a}$$

$$\frac{\partial}{\partial z}\hat{a}_i(\Omega,z) = -\sigma \int d\Omega' \hat{a}_p(\Omega+\Omega',z)\hat{a}_s^\dagger(\Omega',z)e^{-iD(\Omega',\Omega)z}, \tag{3.1b}$$

$$\frac{\partial}{\partial z}\hat{a}_p(\Omega,z) = -\sigma \int d\Omega' \hat{a}_s(\Omega',z)\hat{a}_i(\Omega-\Omega',z)e^{iD(\Omega,\Omega-\Omega')z}. \tag{3.1c}$$

In these equations

$$D(\Omega,\Omega') = k_s(\Omega) - k_i(\Omega') - k_p(\Omega+\Omega') + \frac{2\pi}{\Lambda} \tag{3.2}$$

is the effective phase mismatch that rules the efficiency of each elementary down-conversion process, where a signal and an idler photon of frequencies $\omega_s+\Omega$, $\omega_i+\Omega'$ are generated out of a pump photon of frequency $\omega_p+\Omega+\Omega'$.

In this section we consider the ultra-low gain regime, much below the MOPO threshold, where photons pairs are generated by purely spontaneous down-conversion. In this regime, the depletion of the pump beam can be neglected and the pump field operator can be approximated by a known c-number field, corresponding to the pump pulse at the crystal input face

$$\hat{a}(\Omega,z) \to \alpha_p(\Omega,z) \approx \alpha_p(\Omega,z=0). \tag{3.3}$$

Equations (3.1a) and (3.1b) for the signal and counterpropagating idler are then replaced by :

$$\frac{\partial}{\partial z}\hat{a}_s(\Omega,z) = \frac{g}{l_c}\int \frac{d\Omega'}{\sqrt{2\pi}}\tilde{\alpha_p}(\Omega+\Omega')\hat{a}_i^{\dagger}(\Omega',z)e^{-iD(\Omega,\Omega')z} \tag{3.4a}$$

$$\frac{\partial}{\partial z}\hat{a}_i(\Omega,z) = -\frac{g}{l_c}\int \frac{d\Omega'}{\sqrt{2\pi}}\tilde{\alpha_p}(\Omega+\Omega')\hat{a}_s^{\dagger}(\Omega',z)e^{-iD(\Omega',\Omega)z} \tag{3.4b}$$

where

$$\tilde{\alpha}_p(\Omega) = \int \frac{dt}{\sqrt{2\pi}} e^{i\Omega t}\frac{\alpha(t)}{\alpha_p(t=0)} \tag{3.5}$$

is the Fourier profile of the pump pulse at the crystal input face, normalized to its temporal peak value. The dimensionless gain parameter is given by:

$$g = \sqrt{2\pi}\sigma\alpha_p(t=0)l_c\,, \tag{3.6}$$

where $\alpha_p(t=0)$ is the peak value of the pump temporal profile. We recall that in the limit of a monochromatic pump [33] $g = \pi/2$ represents the threshold for the MOPO. In this section we are interested in the limit $g \ll 1$, where Eqs.(3.4) can be solved perturbatively. Namely, we write the formal solution of (3.4), starting from the boundary conditions:

$$\hat{a}_s(\Omega,z=0) = \hat{a}_s^{\text{in}}(\Omega), \tag{3.7a}$$

$$\hat{a}_i(\Omega,z=l_c) = \hat{a}_i^{\text{in}}(\Omega), \tag{3.7b}$$

determined by the input signal and idler fields, entering the crystal from the left face at $z=0$ and from the right face at $z=l_c$, respectively. Substituting in a recursive way, we get for the

signal

$$\begin{aligned}\hat{a}_s(z,\Omega) =& \hat{a}_s^{\text{in}}(\Omega) + g\int_0^z \frac{dz'}{l_c}\int \frac{d\Omega'}{\sqrt{2\pi}}\tilde{\alpha}_p(\Omega+\Omega')\hat{a}_i^{\dagger\text{in}}(\Omega')e^{-iD(\Omega,\Omega')z'} \\ &+ g^2\int_0^z \frac{dz'}{l_c}\int_{z'}^{l_c}\frac{dz''}{l_c}\int\frac{d\Omega'}{\sqrt{2\pi}}\int\frac{d\Omega''}{\sqrt{2\pi}}\tilde{\alpha}_p(\Omega+\Omega') \\ &\qquad \times \tilde{\alpha}_p^*(\Omega'+\Omega'')\hat{a}_s^{\text{in}}(\Omega'')e^{-iD(\Omega,\Omega')z'}e^{+iD(\Omega'',\Omega')z''} \\ &+ O(g^3). \end{aligned} \tag{3.8}$$

Assuming $g \ll 1$ we can consider only the first order in g of the expression, obtaining:

$$\begin{aligned}\hat{a}_s(\Omega,z) &= \hat{a}_s^{\text{in}}(\Omega) + g\int\frac{d\Omega'}{\sqrt{2\pi}}\tilde{\alpha}_p(\Omega+\Omega')\hat{a}_i^{\dagger\text{in}}(\Omega')\int_0^z\frac{dz'}{l_c}e^{-iD(\Omega,\Omega')z'} \\ &= \hat{a}_s^{\text{in}}(\Omega) + g\int\frac{d\Omega'}{\sqrt{2\pi}}\tilde{\alpha}_p(\Omega+\Omega')\frac{z}{l_c}e^{-iD(\Omega,\Omega')\frac{z}{2}}\text{Sinc}\left[D(\Omega,\Omega')\frac{z}{2}\right]\hat{a}_i^{\dagger\text{in}}(\Omega'). \end{aligned} \tag{3.9}$$

We can do the same for the idler field obtaining:

$$\begin{aligned}\hat{a}_i(\Omega,z) &= \hat{a}_i^{\text{in}}(\Omega) + g\int\frac{d\Omega'}{\sqrt{2\pi}}\tilde{\alpha}_p(\Omega+\Omega')\hat{a}_s^{\dagger\text{in}}(\Omega')\int_0^z\frac{dz'}{l_c}e^{-iD(\Omega',\Omega)z'} \\ &= \hat{a}_i^{\text{in}}(\Omega) + g\int\frac{d\Omega'}{\sqrt{2\pi}}\tilde{\alpha}_p(\Omega+\Omega')\frac{l_c-z}{l_c}e^{-iD(\Omega',\Omega)\frac{(l_c-z)}{2}} \\ &\qquad \times \text{Sinc}\left[D(\Omega',\Omega)\frac{l_c-z}{2}\right]\hat{a}_s^{\dagger\text{in}}(\Omega). \end{aligned} \tag{3.10}$$

The equations (3.9-3.10) respectively for the propagation of the signal and idler field show a symmetry with respect to $\frac{l_c}{2}$. We can also notice that the integration variable Ω' appears in different position in the two equations: as $D(\Omega,\Omega')$ for the signal and as $D(\Omega',\Omega)$ for the idler. This fact will lead to important consequences in determining the spectral properties of the output fields.

Setting $z = l_c$ in the equation for the signal field (3.9) and $z = 0$ in the equation for the idler field (3.10) obtains a Boguliobov linear transformation that links the output to the input operators:

$$\hat{a}_s^{out}(\Omega) = \hat{a}_s^{in}(\Omega) + \int\frac{d\Omega'}{\sqrt{2\pi}}g\tilde{\alpha}_p(\Omega+\Omega')e^{-iD(\Omega,\Omega')\frac{l_c}{2}}\text{Sinc}\left[D(\Omega,\Omega')\frac{l_c}{2}\right]\hat{a}_i^{\dagger in}(\Omega'), \tag{3.11a}$$

$$\hat{a}_i^{out}(\Omega) = \hat{a}_i^{in}(\Omega) + \int\frac{d\Omega'}{\sqrt{2\pi}}g\tilde{\alpha}_p(\Omega+\Omega')e^{-iD(\Omega',\Omega)\frac{l_c}{2}}\text{Sinc}\left[D(\Omega',\Omega)\frac{l_c}{2}\right]\hat{a}_s^{\dagger in}(\Omega), \tag{3.11b}$$

or

$$\hat{a}_s^{out}(\Omega_s) = \hat{a}_s^{in}(\Omega_s) + \int d\Omega_i \Psi(\Omega_s,\Omega_i)\hat{a}_i^{\dagger in}(\Omega_i), \tag{3.12a}$$

$$\hat{a}_i^{out}(\Omega_i) = \hat{a}_i^{in}(\Omega_i) + \int d\Omega_s \Psi(\Omega_s,\Omega_i)\hat{a}_s^{\dagger in}(\Omega_s), \tag{3.12b}$$

where we introduced the *biphoton amplitude* defined as:

$$\Psi(\Omega_s,\Omega_i) = \frac{g}{\sqrt{2\pi}}\tilde{\alpha}_p(\Omega_s+\Omega_i)e^{-iD(\Omega_s,\Omega_i)\frac{l_c}{2}}\,\mathrm{Sinc}\left[D(\Omega_s,\Omega_i)\frac{l_c}{2}\right]. \tag{3.13}$$

In the low gain regime the square modulus of the biphoton amplitude $|\Psi(\Omega_s,\Omega_i)|^2$ is proportional to the joint probability distribution of finding two photons, one with frequency $\omega_s+\Omega_s$ and the other with $\omega_i+\Omega_i$.

Relations (3.12) define a unitary transformation only up to first order in g:

$$\begin{aligned}\left[\hat{a}_s^{out}(\Omega_s),\hat{a}_s^{\dagger out}(\Omega_s')\right] &= \left[\hat{a}_s^{in}(\Omega_s),\hat{a}_s^{\dagger in}(\Omega_s')\right] \\ &\quad + \int d\Omega_i d\Omega_i' \Psi(\Omega_s,\Omega_i)\Psi^*(\Omega_s',\Omega_i')\left[\hat{a}_i^{\dagger}(\Omega_i),\hat{a}_i(\Omega_i')\right] \\ &= \delta(\Omega_s-\Omega_s') + O(g^2),\end{aligned} \tag{3.14}$$

and analogously for the idler. We can also check the commutation relation for the operators:

$$\begin{aligned}&\left[\hat{a}_s^{out}(\Omega_s),\hat{a}_i^{\dagger out}(\Omega_i)\right] \\ &= \left[\hat{a}_s^{in}(\Omega_s) + \int d\Omega_i'\Psi(\Omega_s,\Omega_i')\hat{a}_i^{\dagger in}(\Omega_i'),\hat{a}_i^{in}(\Omega_i) + \int d\Omega_s'\Psi(\Omega_s',\Omega_i)\hat{a}_s^{\dagger in}(\Omega_s')\right] \\ &= \int d\Omega_s'\Psi(\Omega_s',\Omega_i)[\hat{a}_s^{in}(\Omega_s)\hat{a}_s^{\dagger in}(\Omega_s')] - \int d\Omega_i'\Psi(\Omega_s,\Omega_i')[\hat{a}_i^{in}(\Omega_i)\hat{a}_i^{\dagger in}(\Omega_i')] \\ &= \int d\Omega_s'\Psi(\Omega_s',\Omega_i)\delta(\Omega_s-\Omega_s') - \int d\Omega_i'\Psi(\Omega_s,\Omega_i')\delta(\Omega_i'-\Omega_i) = 0,\end{aligned} \tag{3.15}$$

and then the signal and idler output operators commute.

In the following, the input signal and idler field at the left and right end faces of the crystal will be taken in the vacuum state.

It is worth remarking that the quantum field formalism here employed can be replaced by an equivalent state formalism (see Appendix B for more details) where the state evolves instead of the field operators. By applying the transformation (3.12) to the input vacuum state, one obtains at the output the usual state

$$|\phi\rangle_{out} = |0\rangle + \frac{1}{2}\int d\Omega_s d\Omega_i \Psi(\Omega_s,\Omega_i)\hat{a}_s^{\dagger}(\Omega_s)\hat{a}_i^{\dagger}(\Omega_i)\,|0\rangle\,, \tag{3.16}$$

describing the superposition of the vacuum state $|0\rangle$ and of a two-photon state, where the photon pair can be generated in any of the Fourier modes Ω_s, Ω_i with probability amplitude $\Psi(\Omega_s, \Omega_i)$. In this respect, the formalism used here is equivalent to the one employed in [2, 34].

3.1 Spectral biphoton correlation

This section is devoted to the analysis of the biphotonic correlation in the spectral domain. We focus on the probability amplitude $\langle \hat{A}_s^{\text{out}}(\Omega_s), \hat{A}_i^{\text{out}}(\Omega_i) \rangle$ of finding a pair of photons at frequencies Ω_s, Ω_i at the crystal output faces. The biphoton amplitude can be obtained by means of the low gain regime solution to the propagation equation found in the previous Chapter. Using the input-output relations (3.12):

$$\begin{aligned} \langle a_s^{\text{out}}(\Omega_s) a_i^{\text{out}}(\Omega_i) \rangle &= \langle a_s^{\text{in}}(\Omega_s) \int d\Omega_s' \Psi(\Omega_s', \Omega_i) a_s^{\dagger \text{in}}(\Omega_s') \rangle \\ &= \int d\Omega_s' \Psi(\Omega_s', \Omega_i) \delta(\Omega_s - \Omega_s') \\ &= \Psi(\Omega_s, \Omega_i). \end{aligned}$$

From the definitions of the $\hat{A}_j$ operators (1.39) we obtain

$$\langle \hat{A}_s^{\text{out}}(\Omega_s) \hat{A}_i^{\text{out}}(\Omega_i) \rangle = e^{ik_s(\Omega_s) l_c} \Psi(\Omega_s, \Omega_i), \tag{3.17}$$

with $\Psi(\Omega_s, \Omega_i)$ given by Eq.(3.13). As usual, the biphoton correlation is written as the product of the pump spectral amplitude $\tilde{\alpha}_p(\Omega_s + \Omega_i)$, reflecting the energy conservation in the microscopic process, and of the phase matching function $\text{Sinc}[D(\Omega_s, \Omega_i) l_c/2] e^{-iDl_c/2}$, reflecting the generalized momentum conservation. Concerning the latter, we can expand the phase-matching function $D(\Omega_s, \Omega_i)$ in Eq.(3.2) in power series of the frequency shifts from the carriers. Down-conversion spectra are typically narrow [1, 12], as will become also clear in the following, so that one is allowed to retain only terms up to first order

$$\begin{aligned} D(\Omega_s, \Omega_i) \frac{l_c}{2} &= \frac{l_c}{2} [k_s(\Omega_s) - k_i(\Omega_i) - k_p(\Omega_s + \Omega_i) + k_G] \\ &\approx \frac{l_c}{2} \left[(k_s - k_i - k_p + k_G) + k_s' \Omega_s - k_i' \Omega_i - k_p' (\Omega_s + \Omega_i) + \cdots \right] \\ &= \frac{l_c}{2} \left[(k_s' - k_p') \Omega_s - (k_i' + k_p') \Omega_i \right] \\ &= -\left(\frac{\Omega_s}{\Omega_{gvm}} + \frac{\Omega_i}{\Omega_{gvs}'} \right), \end{aligned} \tag{3.18}$$

where the zero order term vanishes because of Eq.(1.34), and $k_i' = dk_j/d\omega\big|_{\omega=\omega_j}$, $j = s,i,p$. We thus see the appearance of the two characteristic temporal scales:

$$\tau_{gvm} \equiv \Omega_{gvm}^{-1} = \tfrac{1}{2}\left[\tfrac{l_c}{v_{gp}} - \tfrac{l_c}{v_{gs}}\right], \tag{3.19}$$

$$\tau'_{gvs} \equiv \Omega'^{-1}_{gvs} = \tfrac{1}{2}\left[\tfrac{l_c}{v_{gp}} + \tfrac{l_c}{v_{gi}}\right], \tag{3.20}$$

where $v_{gi} = 1/k_i'$ are the group velocities of the three wavepackets at the central frequencies. The first scale [Eq.(3.19)] describes the " small" temporal separation between the co-propagating waves due to their group velocity mismatch (GVM) . The second one [Eq.(3.20)] accounts for the "large"temporal separation of the counter-propagating pump and idler waves, which is ruled by the time needed by the pulse centers to cross the crystal. Closely related,

$$\tau_{gvs} = \Omega_{gvs}^{-1} = \frac{1}{2}\left[\frac{l_c}{v_{gs}} + \frac{l_c}{v_{gi}}\right], \tag{3.21}$$

describes the characteristic temporal separation between the arrival times of an idler and a signal photon at their exit faces. Clearly, since group velocities are close, $\tau_{gvs} \approx \tau'_{gvs}$, while $\tau_{gvm} \ll \tau'_{gvs}, \tau_{gvs}$, and

$$\eta = \frac{\tau_{gvm}}{\tau'_{gvs}} = \frac{\Omega'_{gvs}}{\Omega_{gvm}} \ll 1\,. \tag{3.22}$$

Therefore, the phase matching has two well separated scales of variation: as a function of the signal frequency it decays on the broad bandwidth Ω_{gvm}, while as a function of the idler frequency it decays on the narrow bandwidth Ω_{gvs}. Plots of the parameter η, for periodically poled KTP (potassium titanyl phosphate $KTiOPO_4$) and $LiNbO_3$ (lithium niobate), are shown in Fig. 3.1, where **A**,**B**,**C** are the points that will be used as examples in the following.

Notice that the three quantities Ω_{gvm}, Ω'_{gvs} and Ω_{gvs} in Eqs. (3.19-3.21) are linked by the relation

$$\frac{1}{\Omega_{gvs}} = \frac{1}{\Omega'_{gvs}} - \frac{1}{\Omega_{gvm}}. \tag{3.23}$$

Finally, a third relevant scale is the pump spectral bandwidth. For a coherent Gaussian pump

$$\alpha_p(t) = \alpha_p(0)\exp -\frac{t^2}{2\tau_p^2}, \tag{3.24}$$

the pulse duration τ_p is the inverse of the bandwidth

$$\tau_p = \frac{1}{\Delta\Omega_p}. \tag{3.25}$$

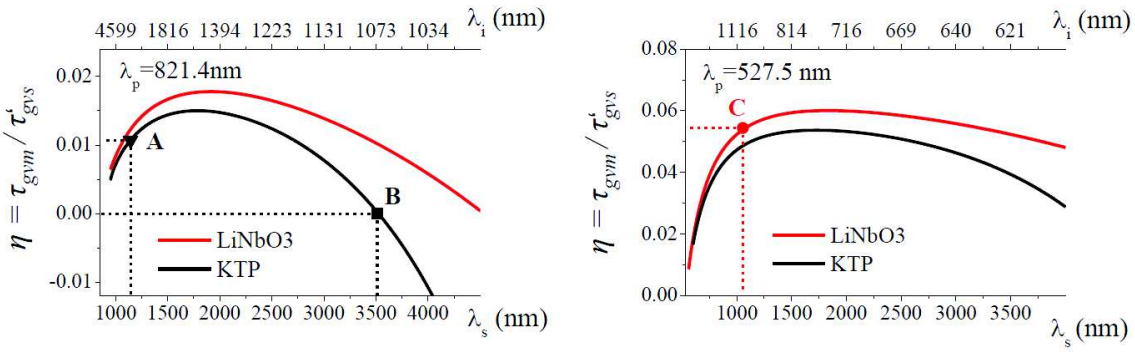

Fig. 3.1 Ratio $\eta = \tau_{gvm}/\tau'_{gvs}$ for periodically poled KTP and $LiNbO_3$, pumped in the infrared or visible, for type 0 $e \to ee$ down-conversion. Point **A** is KTP pumped at $\lambda_p = 821$nm, with $\Lambda_{pol} = 800$nm, $\lambda_s = 1141$nm, $\lambda_i = 2932$nm, corresponding to the experiment in [1] ($\tau_{gvm} = 0.27$ps, $\tau'_{gvs} = 25.5$ps). **B** is the zero GVM point for the KTP at $\lambda_p = 821$nm, corresponding to $\Lambda_{pol} = 290$nm, $\lambda_s = 3523$nm, $\lambda_i = 1071$nm, ($\tau_{gvm} = 0.0$ps, $\tau'_{gvs} = 24.7$ps). **C** is a $LiNbO_3$ slab pumped at $\lambda_p = 527.5$nm, for degenerate PDC at $\lambda_s = \lambda_i = 1055$nm, ($\tau_{gvm} = 1.68$ps,$\tau'_{gvs} = 31.2$ps). with $\Lambda_{pol} = 236$nm.

Depending on the pump bandwidth relative to the spectral scales of phase matching, different physical situations arise. The three relevant possibilities, depicted in Fig.3.2, will be studied separately in the following. In all the cases we will make use of the linear approximation for phase matching (3.18), based on the assumption that the bandwidths in play are narrow so that dispersion can be neglected. Under this approximation, the general expression (3.13) of the biphoton amplitude becomes:

$$\Psi(\Omega_s,\Omega_i) \simeq \frac{g}{\sqrt{2\pi}}\tilde{\alpha}_p\left[\Omega_s+\Omega_i\right]\mathrm{Sinc}\left(\frac{\Omega_s}{\Omega_{gvm}}+\frac{\Omega_i}{\Omega'_{gvs}}\right)e^{i\left(\frac{\Omega_s}{\Omega_{gvm}}+\frac{\Omega_i}{\Omega'_{gvs}}\right)} \tag{3.26}$$

i) Limit of a CW pump:

We assume a narrowband pump pulse, such that

$$\tau_p \gg \tau'_{gvs} \gg \tau_{gvm}, \text{ or } \Delta\Omega_p \ll \Omega'_{gvs} \ll \Omega_{gvm}\,. \tag{3.27}$$

This limit corresponds to a pump pulse that in the z direction is much longer than the crystal slab, and for a crystal of some mm length requires a pulse duration of hundreds of picoseconds or longer. In this limit the pump spectral profile $\tilde{\alpha}_p(\Omega_s+\Omega_i)$ is much narrower than the phase matching bandwidths, and the geometry of the correlation is dominated by energy conservation, which requires that the twins are generated at symmetric frequencies $\Omega_s+\Omega_i = \Omega_p \approx 0$. As a consequence, the biphoton correlation (3.13) has a sharp maximum

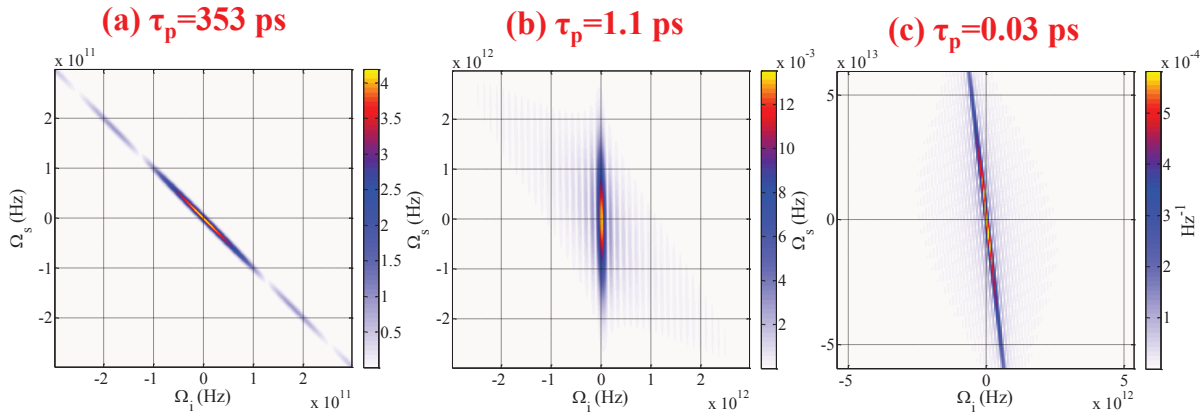

Fig. 3.2 Biphoton correlation $|\Psi|$ [Eq.(3.13)] in the plane (Ω_i, Ω_s), in various pumping regimes. Example of a 4mm PPKTP, pumped at 821.4nm, corresponding to the point **A** in Fig. 3.1, with $\tau_{gvs} = 25.2$ ps, $\tau_{gvm} = 0.27$ ps. (a) Quasi CW pump pulse $\tau_p = 253$ps. (b) Intermediate pump pulse $\tau_p = 1.1$ ps. (c) Ultrashort pump $\tau_p = 0.03$ ps . Note the different scales of the plots $10^{11} \rightarrow 10^{13}$ Hz.

along the diagonal $\Omega_s = -\Omega_i$, as shown by Fig. 3.2a. Since in this limit $\Omega_s + \Omega_i \approx 0$, the biphoton correlation (3.13) reads

$$\Psi(\Omega_s, \Omega_i) \simeq \frac{g}{\sqrt{2\pi}} \tilde{\alpha}_p(\Omega_s + \Omega_i) \mathrm{Sinc}\left[D(\Omega_s, -\Omega_s)\frac{l_c}{2}\right] e^{-iD(\Omega_s, -\Omega_s)\frac{l_c}{2}} \tag{3.28a}$$

$$\simeq \frac{g}{\sqrt{2\pi}} \tilde{\alpha}_p(\Omega_s + \Omega_i) \mathrm{Sinc}\left[D(-\Omega_i, \Omega_i)\frac{l_c}{2}\right] e^{-iD(-\Omega_i, -\Omega_i)\frac{l_c}{2}}. \tag{3.28b}$$

Using the expression for the biphoton amplitude under the linear approximation for the phase-matching (3.26) and the relation (3.23) we obtain the following approximation for the correlation

$$\Psi(\Omega_s, \Omega_i) \simeq \frac{g}{\sqrt{2\pi}} \tilde{\alpha}_p(\Omega_s + \Omega_i) \mathrm{Sinc}\left(\frac{\Omega_s}{\Omega_{gvs}}\right) e^{-i\frac{\Omega_s}{\Omega_{gvs}}} \tag{3.29}$$

$$\simeq \frac{g}{\sqrt{2\pi}} \tilde{\alpha}_p(\Omega_s + \Omega_i) \mathrm{Sinc}\left(\frac{\Omega_i}{\Omega_{gvs}}\right) e^{i\frac{\Omega_i}{\Omega_{gvs}}}. \tag{3.30}$$

ii) Limit of an ultrashort pump pulse:

We consider here the limit:

$$\tau_p \ll \tau_{gvm}, \tau'_{gvs}, \text{ or } \Delta\Omega_p \gg \Omega_{gvm}, \Omega'_{gvs}, \tag{3.31}$$

where the pump pulse is not only shorter than the crystal length, but also shorter than the average separation between the pump and signal wavepackets due their *gvm*. In our examples this corresponds to duration shorter than 100 fs. In these conditions, the pump spectral profile $\tilde{\alpha}_p(\Omega_s+\Omega_i)$ decays slowly with respect to $\mathrm{Sinc}[\bar{D}(\Omega_s,\Omega_i)l_c/2]$. In this case the bandwidths of phase matching are assumed to be much narrower than the pump bandwidth $\Omega'_{gvs} \ll \Omega_{gvm} \ll \Delta\Omega_p$, so that the phase matching function has a narrow peak, which on the slow scale of variation of the pump forces $\Omega_i = -\eta\Omega_s$, or $\Omega_s = -\Omega_i/\eta$ inside the pump argument. Therefore the biphoton correlation takes the approximated form (Fig.3.2c)

$$\Psi(\Omega_s,\Omega_i) \simeq \frac{g}{\sqrt{2\pi}}\tilde{\alpha}_p\left[\Omega_s(1-\eta)\right]\mathrm{Sinc}\left(\frac{\Omega_s}{\Omega_{gvm}}+\frac{\Omega_i}{\Omega'_{gvs}}\right)e^{i\left(\frac{\Omega_s}{\Omega_{gvm}}+\frac{\Omega_i}{\Omega'_{gvs}}\right)} \tag{3.32}$$

$$\simeq \frac{g}{\sqrt{2\pi}}\tilde{\alpha}_p\left[-\Omega_i\frac{1-\eta}{\eta}\right]\mathrm{Sinc}\left(\frac{\Omega_s}{\Omega_{gvm}}+\frac{\Omega_i}{\Omega'_{gvs}}\right)e^{i\left(\frac{\Omega_s}{\Omega_{gvm}}+\frac{\Omega_i}{\Omega'_{gvs}}\right)}. \tag{3.33}$$

When plotted in the plane (Ω_i,Ω_s) (Fig.3.2c), the function shows a sharp maximum along the line

$$\Omega_s = -\Omega_i\frac{\Omega_{gvm}}{\Omega'_{gvs}} \tag{3.34}$$

where phase matching occurs [see Eq.(3.18)], and very asymmetric spectral properties of the signal -idler photons. In the case of a long crystal, ideally with an infinite length, the width of the phase-matching tends to 0 since τ_{gvm} and τ_{gvs} become very long. Thus, in this conditions, every pump can be treated as an ultrashort pump pulse.

iii) Intermediate pump pulse:

The intermediate case, where

$$\tau'_{gvs} \gg \tau_p \gg \tau_{gvm},\ \text{or}\ \Omega'_{gvs} \ll \Delta\Omega_p \ll \Omega_{gvm}\,, \tag{3.35}$$

is the most peculiar one, because the biphoton correlation may approach a separable function of Ω_s,Ω_i (Fig.3.2b). First of all, we remark that the limit (3.35) is strictly realized only for $\eta = \tau_{gvm}/\tau'_{gvs} \to 0$, i.e for a vanishing group velocity mismatch between the pump and the signal. This condition is favorable to separability, because as $\eta \to 0$ the phase matching function tends to become a stripe parallel to the Ω_s axis [see Eq. (3.34)], but it is not a sufficient one, because of the role of the pump profile in Eq.(3.13). For a narrowband pump, as in the example in Fig.3.2a, Ψ is elongated along the diagonal $\Omega_s = -\Omega_i$, and is clearly non-factorable.

By introducing the pump frequency $\Omega_p = \Omega_s + \Omega_i$, we recast the argument of the Sinc function of the biphoton amplitude (3.13)

$$\frac{\Omega_s}{\Omega_{gvm}} + \frac{\Omega_i}{\Omega'_{gvs}} = \frac{\Omega_p}{\Omega_{gvm}} + \Omega_i \left(\frac{1}{\Omega'_{gvs}} - \frac{1}{\Omega_{gvm}} \right) \approx \frac{\Omega_i}{\Omega_{gvs}} \tag{3.36}$$

where the term Ω_p/Ω_{gvm} has been neglected because $\Delta\Omega_p/\Omega_{gvm} \ll 1$.
Concerning the pump amplitude we recast it as:

$$\begin{aligned} \tilde{\alpha}_p(\Omega_s + \Omega_i) &= \tilde{\alpha}_p \left[\Omega_s(1-\eta) + \left(\frac{\Omega_s}{\Omega_{gvm}} + \frac{\Omega_i}{\Omega'_{gvs}} \right) \Omega'_{gvs} \right] \\ &\approx \tilde{\alpha}_p \left[\Omega_s(1-\eta) \right], \end{aligned} \tag{3.37}$$

where the approximation in the second second line holds because $\left(\frac{\Omega_s}{\Omega_{gvm}} + \frac{\Omega_i}{\Omega'_{gvs}} \right)$ is the argument of the Sinc function [see Eq.(3.26)], so that it is limited to values inside the bandwidth of the Sinc, say on the order $\simeq 10$. Provided that $\Omega'_{gvs}/\Delta\Omega_p$ is small enough, this term becomes therefore negligible. With this in mind we can write the limiting behavior of the biphoton amplitude:

$$\lim_{\substack{\tau_p/\tau'_{gvs} \to 0 \\ \tau_{gvm}/\tau_p \to 0}} \Psi(\Omega_s, \Omega_i) = \frac{g}{\sqrt{2\pi}} \tilde{\alpha}_p \left[\Omega_s(1-\eta) \right] e^{i\frac{\Omega_s}{\Omega_{gvm}}} \times \mathrm{Sinc}\left(\frac{\Omega_i}{\Omega_{gvs}} \right) e^{i\frac{\Omega_i}{\Omega_{gvs}}} \tag{3.38}$$

$$\approx \frac{g}{\sqrt{2\pi}} \tilde{\alpha}_p[(\Omega_s) e^{i\frac{\Omega_s}{\Omega_{gvm}}} \times \mathrm{Sinc}\left(\frac{\Omega_i}{\Omega_{gvs}} \right) e^{i\frac{\Omega_i}{\Omega_{gvs}}}. \tag{3.39}$$

where the approximation in the last line is not mandatory, but could be useful in order to get consistent results, because clearly this limit can be realized only for $\eta = \tau_{gvm}/\tau'_{gvs} \to 0$. i.e. it becomes the product of a function of Ω_s, reproducing the pump profile, and a function of Ω_i, corresponding to the phase matching profile. This describes a non entangled biphoton state, with the signal photon generated in the same spectro- temporal mode as the pump, while the spectral mode of the idler is dictated by the phase matching "Sinc" function of width Ω_{gvs}. This qualitative picture will be confirmed by the evaluation of the Schmidt number in Sec. 3.4, and will be further interpreted and discussed in the light of the temporal correlation of biphotons described in the next section.

3.2 Interpretation: biphoton correlation in the time domain

An alternative insight into the issue of separability vs entanglement is provided by the analysis of the biphoton correlation in the temporal domain. We consider

$$\phi(t_s,t_i) = \langle \hat{A}_s^{out}(t_s)\hat{A}_i^{out}(t_i)\rangle \int \frac{d\Omega_s}{\sqrt{2\pi}} \int \frac{d\Omega_i}{\sqrt{2\pi}} e^{-i(\Omega_s t_s+\Omega_i t_i)} e^{ik_s(\Omega_s)l_c} \Psi(\Omega_s,\Omega_i)\,, \tag{3.40}$$

which is proportional to the probability amplitude of finding a signal and an idler photons at their crystal end faces at times t_s, t_i. By using the linear approximation for phase matching (3.18) and writing also $k_s(\Omega_s) = k_s + k_s'\Omega_s l_c + \cdots$, we obtain

$$\begin{aligned}\phi(t_s,t_i) = \frac{g e^{ik_s l_c}}{\sqrt{2\pi}} \int \frac{d\Omega_s d\Omega_i}{2\pi}\, \tilde{\alpha}_p(\Omega_s+\Omega_i)\mathrm{Sinc}(\Omega_s\tau_{gvm}+\Omega_i\tau_{gvs}) \\ \times e^{i(k_s'+k_p')\Omega_s\frac{l_c}{2}} e^{i(k_i'+k_p')\Omega_i\frac{l_c}{2}} e^{-i(\Omega_s t_s+\Omega_i t_i)}\,,\end{aligned} \tag{3.41}$$

and, changing the integration variable $\Omega_s \to \Omega_p = \Omega_s + \Omega_i$, it becomes:

$$\begin{aligned}\phi(t_s,t_i) = \frac{g e^{ik_s l_c}}{\sqrt{2\pi}} \int d\Omega_p\, \tilde{\alpha}_p(\Omega_p) e^{-i\Omega_p\left(t_s - \frac{k_s'+k_p'}{2}l_c\right)} \\ \times \int \frac{d\Omega_i}{2\pi}\, e^{-i\Omega_i\left[t_i - t_s - \frac{k_i'-k_s'}{2}l_c\right]} \mathrm{Sinc}(\Omega_p\tau_{gvm}+\Omega_i\tau_{gvs}).\end{aligned} \tag{3.42}$$

Introducing $\Delta t = t_i - t_s - (k_i' - k_s')\frac{l_c}{2}$ and using the identity $\mathrm{Sinc}(x) = \frac{1}{2}\int_{-1}^{1} ds\, e^{isx}$, we can calculate the Fourier transform in $d\Omega_i$. We thus obtain:

$$\begin{aligned}\phi(t_s,t_i) &= \frac{g e^{ik_s l_c}}{2\tau_{gvs}} \int \frac{d\Omega_p}{\sqrt{2\pi}}\, \tilde{\alpha}_p(\Omega_p) e^{-i\Omega_p\left(t_s - \Delta t\frac{\tau_{gvm}}{\tau_{gvs}'} - \frac{k_s'+k_p'}{2}l_c\right)} \mathrm{Rect}\left(\frac{\Delta t}{2\tau_{gvs}}\right) \\ &= \frac{g e^{ik_s l_c}}{2\tau_{gvs}} \alpha_p\left(t_s - \frac{k_s'+k_p'}{2}l_c - \Delta t\frac{\tau_{gvm}}{\tau_{gvs}}\right) \mathrm{Rect}\left(\frac{\Delta t}{2\tau_{gvs}}\right),\end{aligned} \tag{3.43}$$

where

$$\mathrm{Rect}(x) = \begin{cases} 1 & \text{for} \quad x \in \left(-\frac{1}{2},\frac{1}{2}\right) \\ 0 & \text{elsewhere} \end{cases}\,, \tag{3.44}$$

is the box function of unitary width. We introduce now the barred arguments $\bar{t}_s, \bar{t}_i$, which denote time intervals measured starting from the arrival times of the centers of the signal/idler

wavepackets. Precisely, $\bar{t}_{s,i} = t_{s,i} - t_{As,i}$, where

$$t_{As} = (k'_s + k'_p)\frac{l_c}{2} = t_{Ap} - (k'_p - k'_s)\frac{l_c}{2}, \tag{3.45}$$

$$t_{Ai} = (k'_i + k'_p)\frac{l_c}{2} = t_{Ap} - (k'_p - k'_i)\frac{l_c}{2}, \tag{3.46}$$

where $t_{Ap} = k'_p l_c$ is the time when the center of the pump pulse exits the crystal slab. Eq. (3.43) can finally be rewritten as:

$$\phi(\bar{t}_s, \bar{t}_i) = \frac{g e^{ik_s l_c}}{2\tau_{gvs}} \alpha_p \left(\bar{t}_s + \eta \frac{\bar{t}_s - \bar{t}_i}{1-\eta} \right) \mathrm{Rect}\left(\frac{\bar{t}_s - \bar{t}_i}{2\tau_{gvs}} \right) \tag{3.47}$$

Figure 3.3 shows three examples of the temporal correlation function (3.47).

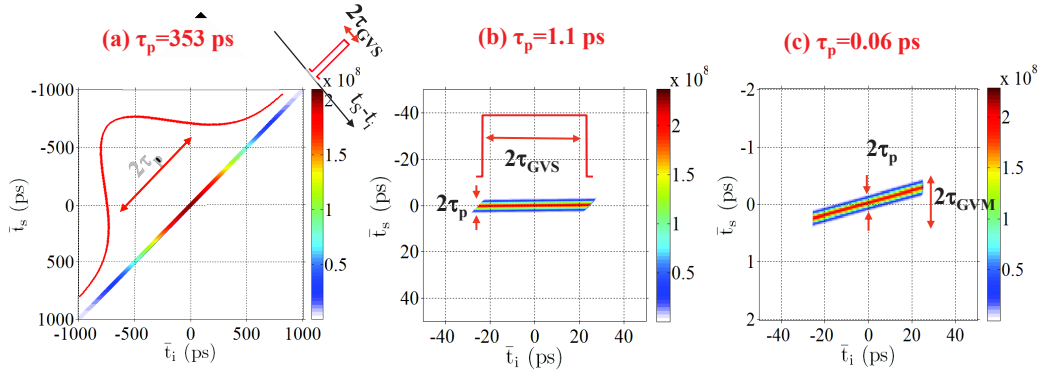

Fig. 3.3 Temporal correlation of twin photons $|\phi(\bar{t}_i, \bar{t}_s)|$, given by Eq.(3.47), plotted in the plane $(\bar{t}_i, \bar{t}_s)$. (a)High entanglement case, with $\mathcal{K} \simeq 26$, for a quasi CW pump $\tau_p = 14\tau'_{gvs}$. (b)Almost separable case with $\mathcal{K} \simeq 1.06$, for an intermediate pump $\tau_p = 0.04\tau'_{gvs} = 4\tau_{gvm}$. (c)Ultrashort pulse $\tau_p = 0.22\tau_{gvm}$, corresponding to an entangled state with $\mathcal{K} \simeq 4$. Same KTP crystal as in Fig.3.6

The general formula (3.47) can be simplified in the limit where the pump is long with respect to τ_{gvm}, i.e. in the quasi CW or intermediate limits (3.27, 3.35) , where it takes the form

$$\phi(\bar{t}_s, \bar{t}_i) \overset{\tau_p \gg \tau_{gvm}}{\simeq} g e^{ik_s l_c} \alpha_p(\bar{t}_s) \frac{1}{2\tau_{gvs}} \mathrm{Rect}\left(\frac{\bar{t}_i - \bar{t}_s}{2\tau_{gvs}} \right), \tag{3.48}$$

Indeed, when the the pump pulse is long with respect to τ_{gvm}, we have $\alpha_p\left(\bar{t}_s + \eta \frac{\bar{t}_s - \bar{t}_i}{1-\eta}\right) \approx \alpha_p(\bar{t}_s)$, because $|\bar{t}_s - \bar{t}_i|$ is limited by the box function to values smaller than τ_{gvs}, so that $\eta \frac{|\bar{t}_s - \bar{t}_i|}{1-\eta} = \frac{\tau_{gvm}}{\tau_{gvs}} |\bar{t}_s - \bar{t}_i| \leq \tau_{gvm} \ll \tau_p$.

Formula (3.49) shows that in the limit of a negligible GVM, the distribution of separations $\bar{t}_s - \bar{t}_i$ between the arrival times of the twin photons is entirely described by the box function of width $2\tau_{gvs}$. This form of the temporal correlation clearly reflects the spontaneous character of the process, where photon pairs can be generated at any point of the crystal with uniform probability. Thus, assuming for simplicity that the the twins travel with the same group velocities $v_{gs} = v_{gi}$, the separation between their arrival times ranges with uniform probability from zero, when the two photons are generated at the center of the crystal up to $\pm\tau_{gvs} = l_c/v_g$, when they are generated at each of the end faces. [1]

The CW pump limit (Fig.3.3a) corresponds to the situation where the pump pulse is much longer than the maximal temporal separation τ_{gvs} between the twins. In this case, the usual picture of the temporal entanglement of twin photons holds: the time when a signal or idler photon is individually detected has a large indeterminacy, because a photon pair can be generated at any time along the pump pulse. However, from the arrival time of one of the members of the pair one can infer the arrival time of the other with a much smaller uncertainty τ_{gvs}, which represents the mean uncertainty in the arrival time of one photon provided its twin have been detected, i.e. the *correlation time*. This kind of correlation is basically what predicted in Ref. [33] for a strictly monochromatic pump.

However, when the pump pulse shorten below τ_{gvs} (Fig.3.3b) this description ceases to be valid, because the localization of the pump pulse provides a timing information on the arrival time of the signal that is more precise than the uncertainty in the temporal separation of the twins. Indeed when the pump pulse is much shorter than τ_{gvs}, but still long enough that GVM is negligible, the signal wavepacket overlaps almost exactly with the pump pulse during propagation, and the uncertainty in the arrival time of the signal is just the pulse duration. This is much smaller than the conditional uncertainty τ_{gvs} by which the arrival time of the idler can be inferred from that of the signal, so that the arrival times of the members of the pair appear completely uncorrelated. Indeed, the temporal correlation in Fig.3.3b is approximately:

$$\phi(\bar{t}_s, \bar{t}_i) \simeq g e^{ik_s l_c} \alpha_p(\bar{t}_s) \frac{1}{2\tau_{gvs}} \mathrm{Rect}\left(\frac{\bar{t}_i}{2\tau_{gvs}}\right), \tag{3.49}$$

which is a factorable function of $\bar{t}_s, \bar{t}_i$.

Notice that when the pump pulse is so short that GVM starts to be important (Fig.3.3c), there is again a loss of absolute timing information, because in this case the arrival time of the signal cannot be inferred from that of the pump with a precision better than τ_{gvm}. In

[1] Precisely, when the two photons are generated at the crystal center $t_s - t_i = t_{As} - t_{Ai} = (k'_s - k'_i)l_c/2 \approx 0$, and the delay between their arrival times ranges uniformly between i) $t_s - t_i = t_{As} - t_{Ai} - \tau_{gvs} = -k'_i l_c$, when they are generated at the right end face of the slab, and ii) $t_s - t_i = t_{As} - t_{Ai} + \tau_{gvs} = k'_s l_c$ when the photon pair is generated at the left end face.

contrast, the arrival time of the signal *conditioned* to a photon count in the idler arm can be predicted within the short pump duration τ_p, and the state becomes again entangled. This can be better understood by looking the correlation function (3.47), which for $\tau_p \ll \tau_{gvm}$ can be rewritten as

$$\phi(\bar{t}_s,\bar{t}_i) = \frac{g e^{ik_s l_c}}{2\tau_{gvs}} \alpha_p \left(\frac{\bar{t}_s - \eta\bar{t}_i}{1-\eta}\right) \mathrm{Rect}\left(\frac{\bar{t}_s - \bar{t}_i}{2\tau_{gvs}}\right) \tag{3.50}$$

$$\simeq \frac{g e^{ik_s l_c}}{2\tau_{gvs}} \alpha_p \left(\frac{\bar{t}_s - \eta\bar{t}_i}{1-\eta}\right) \mathrm{Rect}\left(\frac{\bar{t}_s}{2\tau_{gvm}}\right). \tag{3.51}$$

where the last line has been obtained by substituting $\bar{t}_i = \bar{t}_s/\eta$ inside the argument of the box function (valid because the pump profile is much narrower than both τ_{gvs} and τ_{gvm}). From formula (3.51) we see that, provided that an idler photon is detected, say at time $\bar{t}_i$, the arrival time of the signal can be predicted as $\bar{t}_s = \eta\bar{t}_i$ within the narrow uncertainty of the pump duration τ_p (see also Fig.3.3c). However when the idler is not detected, the overall uncertainty in the signal arrival time is the larger width τ_{gvm} of the box function. Clearly this argument predicts an entangled state, with the number of modes scaling as τ_{gvm}/τ_p, in agreement with formula (3.89).

3.3 Spectral coherence

This section is devoted to the spectral coherence properties, studied by means of the first order coherence functions

$$G_s^{(1)}(\Omega,\Omega') = e^{-i[k_s(\Omega')-k_s(\Omega)]l_c} \langle \hat{A}_s^{\dagger\,out}(\Omega)\hat{A}_s^{out}(\Omega')\rangle, \tag{3.52}$$

$$G_i^{(1)}(\Omega,\Omega') = \langle \hat{A}_i^{\dagger\,out}(\Omega)\hat{A}_i^{out}(\Omega')\rangle, \tag{3.53}$$

(where a propagation phase factor is present in the first definition just for convenience of notation). From the input-output relations (3.12) one has:

$$G_s^{(1)}(\Omega_s,\Omega_s') = \int d\Omega_i \int d\Omega_i' \Psi^*(\Omega_s,\Omega_i)\Psi(\Omega_s',\Omega_i')\langle \hat{a}^{\mathrm{in}}(\Omega_i)\hat{a}^{\dagger\mathrm{in}}(\Omega_i')\rangle$$

$$= \int d\Omega_i \Psi^*(\Omega_s,\Omega_i)\Psi(\Omega_s',\Omega_i), \tag{3.54}$$

$$G_i^{(1)}(\Omega_i,\Omega_i') = \int d\Omega_s \int d\Omega_s' \Psi^*(\Omega_s,\Omega_i)\Psi(\Omega_s',\Omega_i')\langle \hat{a}^{\mathrm{in}}(\Omega_s)\hat{a}^{\dagger\mathrm{in}}(\Omega_s')\rangle$$

$$= \int d\Omega_s \Psi^*(\Omega_s,\Omega_i)\Psi(\Omega_s,\Omega_i'). \tag{3.55}$$

i.e. the coherence functions are convolution integrals over the biphoton amplitude Ψ, given by Eq(3.13) . The knowledge of the $G_j^{(1)}$ is sufficient to determine all the statistical properties of the marginal distributions. For example, the autocorrelation of the light intensities $\hat{I}_j = \hat{A}_j^\dagger \hat{A}_j$ is given by

$$\begin{aligned}
\langle \hat{I}_j(\Omega)\hat{I}_j(\Omega')\rangle &= \langle \hat{A}_j^\dagger(\Omega)\hat{A}_j(\Omega)\hat{A}_j^\dagger(\Omega')\hat{A}_j(\Omega')\rangle \\
&= \delta(\Omega-\Omega')\langle \hat{A}_j^\dagger(\Omega)\hat{A}_j(\Omega)\rangle + \langle \hat{A}_j^\dagger(\Omega)\hat{A}_j^\dagger(\Omega')\hat{A}_j(\Omega)\hat{A}_j(\Omega')\rangle \\
&= \delta(\Omega-\Omega')\langle \hat{I}_j(\Omega)\rangle + \langle \hat{A}_j^\dagger(\Omega)\hat{A}_j(\Omega)\rangle\langle \hat{A}_j^\dagger(\Omega')\hat{A}_j(\Omega')\rangle \\
&\quad + \langle \hat{A}_j^\dagger(\Omega)\hat{A}_j(\Omega')\rangle\langle \hat{A}_j^\dagger(\Omega')\hat{A}_j(\Omega)\rangle \\
&= \delta(\Omega-\Omega')\langle \hat{I}_j(\Omega)\rangle + \langle \hat{I}_j(\Omega)\rangle\langle \hat{I}_j(\Omega')\rangle + \left|G_j^{(1)}(\Omega,\Omega')\right|^2, \qquad (3.56)
\end{aligned}$$

where $\langle \hat{I}_j(\Omega)\rangle = G_j^{(1)}(\Omega,\Omega)$. This relation, which is a consequence of the factorization theorem of Gaussian moments, is typical of thermal-like statistics. As a matter of fact, the marginal distributions of the output signal-idler light are thermal-like Gaussian, when there is vacuum at the input. In the low-gain regime considered here, the dominant term is the first one, i.e. the "shot-noise" term δ-correlated in frequencies,

$$\langle \hat{I}_j(\Omega)\hat{I}_j(\Omega')\rangle \overset{g\ll 1}{\approx} \delta(\Omega-\Omega')\langle \hat{I}_j(\Omega)\rangle. \qquad (3.57)$$

Therefore, as well known in this regime the statistics of photon counts in each arm is Poissonian.
On the other side, the convolution integrals in Eqs. (3.54), (3.55) indicate that an autocorrelation of spectral fluctuations inside each individual signal or idler wave exists because of second order processes, that involve the probability amplitudes of generating at two pairs of photons.

In the following we shall illustrate the three relevant cases. The coherence functions will be evaluated both numerically (Fig.3.4) and analytically. In the first case, the complete Sellmeier relations [23] will be used to compute the integrals in (3.54), (3.55), while the linear approximation for phase matching will be exploited to derive approximated analytical formulas.

i) Limit of a CW pump:

Column (a) of Fig.3.4 shows an example of the signal and idler coherence functions in the plane (Ω,Ω'), numerically computed in the case of a long pump pulse $\tau_p \simeq 14\tau'_{gvs}$.
In the limit $\tau_p \gg \tau'_{gvs}$, approximated expressions for the coherence functions can be calculated

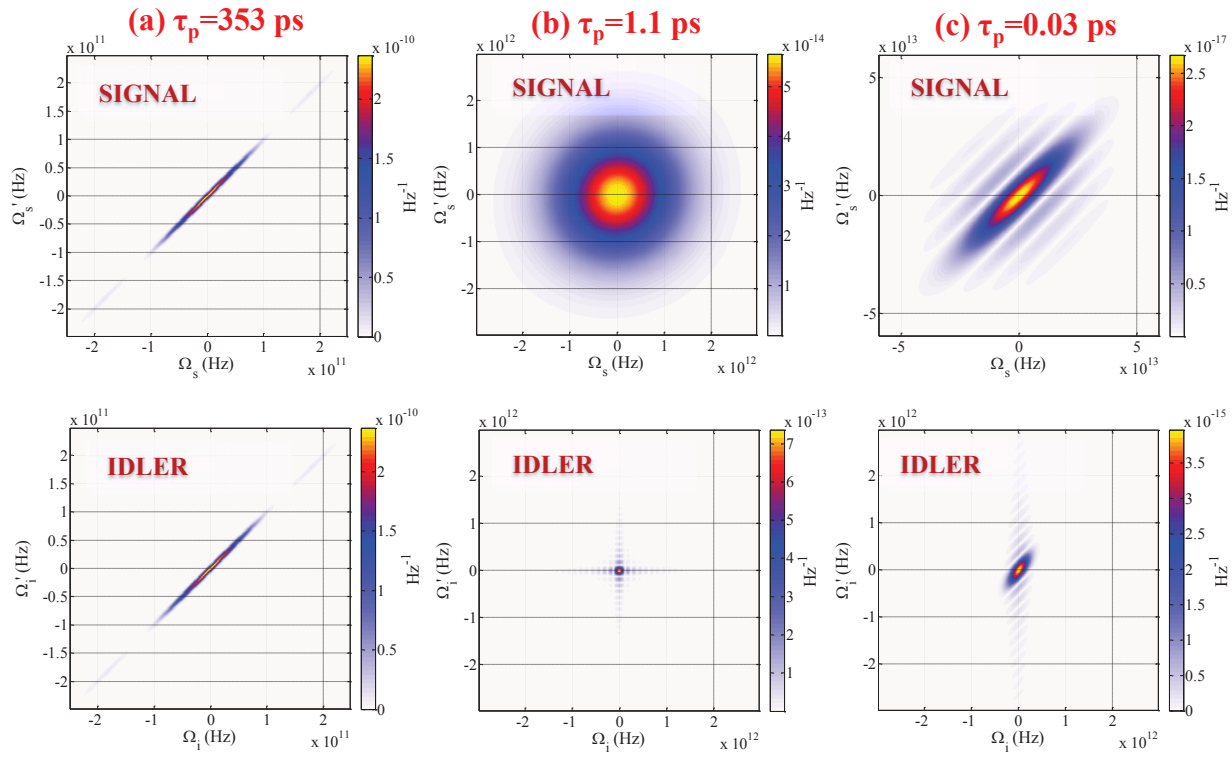

Fig. 3.4 Coherence functions $|G(\Omega,\Omega')|$ of the forward signal and backward propagating idler are plotted in the upper and lower row, respectively, for different pumping regime . Column (a) Quasi CW pump pulse $\tau_p = 353$ps. (b) Intermediate pump pulse $\tau_p = 1.1$ ps. (c) Ultrashort pump $\tau_p = 0.03$ ps. Same KTP crystal slab as in Fig.3.2 (point **A** in Fig. 3.1), with $\tau_{gvs} = 25.2$ ps, $\tau_{gvm} = 0.27$ ps. Note the different scales in the panels

by inserting the formulas for the biphoton correlation (3.29) and (3.30), valid in this limit, into Eqs. (3.54) and (3.55), respectively:

$$G_s^{(1)}(\Omega,\Omega') \approx \int d\Omega_i \, \frac{g^2}{2\pi} \tilde{\alpha}_p^*(\Omega_s+\Omega_i)\tilde{\alpha}_p(\Omega_s'+\Omega_i) \times \mathrm{Sinc}\left(\frac{\Omega_s}{\Omega_{gvs}}\right) e^{i\frac{\Omega_s}{\Omega_{gvs}}} \mathrm{Sinc}\left(\frac{\Omega_s'}{\Omega_{gvs}}\right) e^{-i\frac{\Omega_s'}{\Omega_{gvs}}}. \tag{3.58}$$

Since the phase matching bandwidths in this limit do not depend on the integration variable we can consider the integral of the pump spectral profiles and, exploiting the definition given

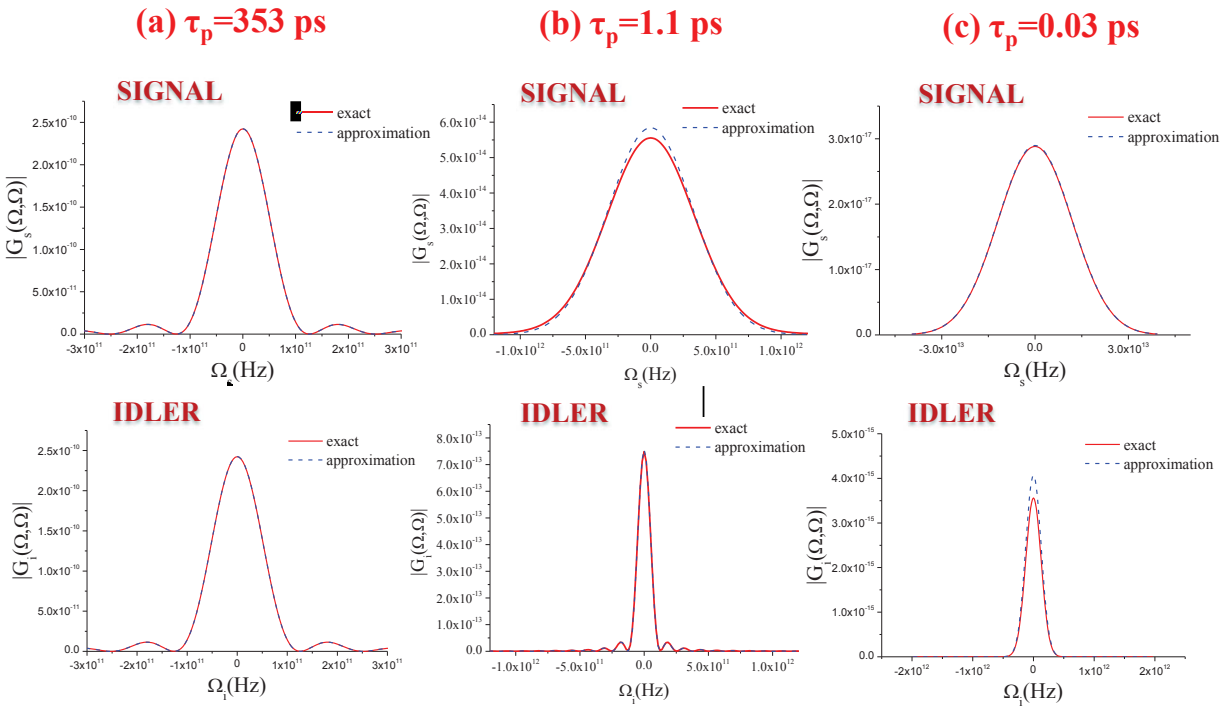

Fig. 3.5 Emission spectra $G^{(1)}(\Omega,\Omega)=\tilde{\mathcal{I}}(\Omega)$ [Eq.(6.5)] of the forward signal and backward propagating idler are plotted in the upper and lower row, respectively, for different pumping regime . Column (a) Quasi CW pump pulse $\tau_p = 353$ps. (b) Intermediate pump pulse $\tau_p = 1.1$ ps. (c) Ultrashort pump $\tau_p = 0.03$ ps. Same KTP crystal slab as in Fig.3.2 (point **A** in Fig. 3.1), with $\tau_{gvs} = 25.2$ ps, $\tau_{gvm} = 0.27$ ps. Note the different scales in the panels. In all the figures "'exact"' refers to results obtained from the definition of coherence given in Eq. (3.54,3.55), while "'approximation"' refers to the analytical calculations in the following.

in Eq. (3.5), we get

$$\begin{aligned}
&\int d\Omega_i \tilde{\alpha}_p^*(\Omega_s+\Omega_i)\tilde{\alpha}_p(\Omega_s'+\Omega_i) \\
&\qquad = \frac{1}{2\pi}\int d\Omega_i \int dt \int dt' \, \frac{\alpha_p^*(t)}{\alpha_p^*(0)} e^{-i(\Omega_s+\Omega_i)t} \frac{\alpha_p(t')}{\alpha_p(0)} e^{-i(\Omega_s'+\Omega_i)t}, \\
&\qquad = \int dt \left|\frac{\alpha_p(t)}{\alpha_p(0)}\right|^2 e^{i(\Omega_s'-\Omega_s)t}, \\
&\qquad = 2\pi\tilde{\mathcal{I}}_p(\Omega_s'-\Omega_s),
\end{aligned} \tag{3.59}$$

where $\tilde{\mathcal{I}}_p(\Omega) = \int \frac{dt}{2\pi} e^{i\Omega t} \left|\alpha_p(t)/\alpha_p(0)\right|^2$ is the Fourier transform of the pump intensity profile. Moreover we notice that in this limit the pump spectral profile is much narrower than the phase

matching bandwidths and this forces $\Omega_s = \Omega'_s$ in the phase matching functions. Eq. (3.58) thus becomes (for the idler field we can find the same result)

$$G_s^{(1)}(\Omega,\Omega') \approx G_i^{(1)}(\Omega,\Omega') \overset{\tau_p \gg \tau'_{gvs}}{\longrightarrow} \tilde{\mathcal{I}}_p(\Omega'-\Omega)\, g^2 \mathrm{Sinc}^2\left(\frac{\Omega}{\Omega_{gvs}}\right). \tag{3.60}$$

These results may be considered the more refined version of the much simpler CW model analyzed in [33], with the narrow peak $\tilde{\mathcal{I}}_p(\Omega'-\Omega)$ being the finite counterpart of the singular Dirac δ appearing in the strictly CW pump model 4.
For a quasi-CW pump the counter-propagating signal and idler photons are predicted to have identical spectral coherence properties. In particular, by looking at the $G^{(1)}$ functions along the diagonal $\Omega' = \Omega$ we see that their spectra $\langle \hat{I}_j(\Omega)\rangle = \langle \hat{A}_j^\dagger(\Omega)\hat{A}_j(\Omega)\rangle$

$$\begin{aligned}\langle \hat{I}_s(\Omega)\rangle = \langle \hat{I}_i(\Omega)\rangle &= \tilde{\mathcal{I}}_p(0)\, g^2 \mathrm{Sinc}^2\left(\frac{\Omega}{\Omega_{gvs}}\right) \\ &\simeq \frac{g^2\tau_p}{\sqrt{2\pi}}\mathrm{Sinc}^2\left(\frac{\Omega}{\Omega_{gvs}}\right),\end{aligned} \tag{3.61}$$

are identical and entirely determined by the narrow bandwidth of phase matching Ω_{gvs} . This bandwidth is in turn the inverse of the characteristic separation τ_{gvs} between the arrival time of an idler and a signal photon at their crystal end faces, which roughly corresponds to the *long* transit time of light along the crystal slab, because they propagate in opposite directions. As already noticed in [33], and as will be further discussed in Sec3.2 this is clearly a big difference with the copropagating case. There, the temporal uncertainty between the arrival times of the idler and signal photon is short, because determined at most by the group velocity dispersion or mismatch, which results in the huge down-conversion bandwidths that characterize the standard co-propagating configuration. These approximated formulas show a good agreement with the numerical results obtained from the definition in Eq. (3.54,3.55) using the complete Sellmeier relation [35], see Fig. 3.5

On the other side, when studied as a function of $\Omega' - \Omega$ the $G^{(1)}$ gives the characteristic size of spectral fluctuations, i.e. the spectral *coherence length*. This is determined by the pump bandwidth, more precisely by the width $\sqrt{2}\Delta\Omega_p$ of $\tilde{\mathcal{I}}_p(\Omega'-\Omega)$, which is much narrower than the spectral bandwidths Ω_{gvs}. We can heuristically estimate the number of modes by counting the number of coherence length contained in the spectrum: therefore, for such a long pulse we expect each signal and idler photon to be generated in a highly incoherent and multimode state, with the number of modes $\propto \frac{\Omega_{gvs}}{\Delta\Omega_p} = \frac{\tau_p}{\tau_{gvs}}$.

ii) Ultrashort pump pulse:

When the pump pulse shorten below the transit time τ'_{gvs} along the crystal slab, the spectral properties of the counterpropagating idler and signal change drastically, becoming strongly asymmetric. First we consider the case of an ultrashort pulse, $\tau_p \ll \tau_{gvm}$ (i.e. such that pump and the signal tend to split apart during propagation). The asymmetry between the forward and backward propagating photons can be clearly appreciated in the third column of Fig. 3.4, which plots their coherence functions for $\tau_p \approx 0.1\tau_{gvm}$.
Approximated expressions for the coherence functions are derived also in this case, by using the limit behavior of the biphoton correlation described by Eqs. (3.32) and (3.33). Since in this limit the pump spectral profile do not depend on the integration variable:

$$G_s^{(1)}(\Omega,\Omega') \approx \frac{g^2}{2\pi}\left|\tilde{\alpha}_p[\Omega_s(1-\eta)]\right|^2 \int d\Omega_i \,\mathrm{Sinc}\left(\frac{\Omega_s}{\Omega_{gvm}}+\frac{\Omega_i}{\Omega'_{gvs}}\right) e^{i\frac{\Omega_s}{\Omega_{gvm}}+\frac{\Omega_i}{\Omega'_{gvs}}} \times \mathrm{Sinc}\left(\frac{\Omega'_s}{\Omega_{gvm}}+\frac{\Omega_i}{\Omega'_{gvs}}\right) e^{-i\frac{\Omega'_s}{\Omega_{gvm}}+\frac{\Omega_i}{\Omega'_{gvs}}}. \quad (3.62)$$

We change the integration variable introducing $\bar{\Omega} = \Omega_s/\Omega_{gvs} + \Omega_i/\Omega'_{gvs}$, $\Omega_i = \bar{\Omega}\Omega'_{gvs} - \Omega_s\Omega'_{gvs}/\Omega_{gvm}$. The integral to evaluate in Eq.(3.68) become:

$$\begin{aligned} G_s^{(1)}(\Omega,\Omega') &\approx \int d\bar{\Omega}\,\Omega'_{gvs}\mathrm{Sinc}\left(\bar{\Omega}\right)\mathrm{Sinc}\left(\bar{\Omega}+\frac{\Omega'_s-\Omega_s}{\Omega_{gvm}}\right)e^{-i\bar{\Omega}}e^{i\left(\bar{\Omega}+\frac{\Omega'_s-\Omega_s}{\Omega_{gvm}}\right)} \\ &= \Omega'_{gvs}e^{i\left(\frac{\Omega'_s-\Omega_s}{\Omega_{gvm}}\right)}\int d\bar{\Omega}\int_{-1}^{1}ds\,\frac{1}{2}e^{-i\bar{\Omega}s}\int_{-1}^{1}ds'\,\frac{1}{2}e^{i\bar{\Omega}s'}e^{-\frac{\Omega'_s-\Omega_s}{\Omega_{gvm}}s'} \\ &= \frac{\pi}{2}\Omega'_{gvs}e^{i\left(\frac{\Omega'_s-\Omega_s}{\Omega_{gvm}}\right)}\int_{-1}^{1}ds\int_{-1}^{1}ds'\,\delta(s-s')e^{-\frac{\Omega'_s-\Omega_s}{\Omega_{gvm}}s'} \\ &= \pi\Omega'_{gvs}e^{i\left(\frac{\Omega'_s-\Omega_s}{\Omega_{gvm}}\right)}\mathrm{Sinc}\left(\frac{\Omega'_s-\Omega_s}{\Omega_{gvm}}\right). \end{aligned} \quad (3.63)$$

The coherence function in the ultra-short pump limit results

$$G_s^{(1)}(\Omega,\Omega') \overset{\tau_p\ll\tau_{gvm}}{\longrightarrow} \frac{g^2\Omega'_{gvs}}{2}\left|\tilde{\alpha}_p[\Omega(1-\eta)]\right|^2\mathrm{Sinc}\left(\frac{\Omega'-\Omega}{\Omega_{gvm}}\right)e^{-i\left(\frac{\Omega'-\Omega}{\Omega_{gvm}}\right)} \quad (3.64)$$

This formula predicts that the spectrum of the forward propagating signal

$$\langle\hat{I}_s(\Omega)\rangle = \frac{g^2\Omega'_{gvs}}{2}\left|\tilde{\alpha}_p[\Omega(1-\eta)]\right|^2 \quad (3.65)$$

is a replica of the pump spectrum with a scale factor $\frac{1}{1-\eta} = \frac{k'_p+k'_i}{k'_i+k'_s}$ on the order unity. The coherence length of the signal (the characteristic size of spectral fluctuations) is instead

determined by the width of the narrower sinc function, $l_{coh,s} \approx \Omega_{gvm}$. From this picture we thus expect that the signal photon, when detected independently from its twin, is in a incoherent multimode state, with the number of modes $\propto \frac{\Delta\Omega_p}{(1-\eta)\Omega_{gvm}}$.
In a similar way, for the idler photon we get:

$$G_i^{(1)}(\Omega,\Omega') \overset{\tau_p \ll \tau_{gvm}}{\longrightarrow} \frac{g^2\Omega_{gvm}}{2}\left|\tilde{\alpha}_p[-\Omega\frac{1-\eta}{\eta}]\right|^2 \times \mathrm{Sinc}\left(\frac{\Omega'-\Omega}{\Omega'_{gvs}}\right) e^{-i\left(\frac{\Omega'-\Omega}{\Omega'_{gvs}}\right)}. \qquad (3.66)$$

This formula predicts an idler bandwidth much narrower than the pump, precisely it predicts that the idler spectrum follows the pump spectrum with a scale factor $\frac{\eta}{1-\eta} = \frac{k'_p-k'_s}{k'_i+k'_s} \ll 1$. The coherence length of the idler is $l_{coh,i} \approx \Omega'_{gvs}$, so that the number of temporal modes is predicted to scale as $\frac{\eta\Delta\Omega_p}{(1-\eta)\Omega'_{gvs}} = \frac{\Delta\Omega_p}{(1-\eta)\Omega_{gvm}}$, which is the same number as for the signal (as it must be because the signal and idler are the two members of the same entangled state, and their reduced states must exhibit the same Schmidt dimensionality, see next section) .These approximated formulas have been checked with the numerical results and show an excellent match, see Fig. 3.5.

Notice that this particular scaling of the bandwidths of the forward and backward propagating waves with the pump bandwidth is well known in the literature concerning the MOPO. There, the same scaling factors, $\frac{k'_p+k'_i}{k'_i+k'_s}$ for the forward-propagating signal and $\frac{k'_p-k'_s}{k'_i+k'_s}$ for the backward propagating idler, are predicted to occurr [1, 16], by using arguments based on the phase-matching characteristic of the process. Here, however, the analysis concerns the quantum properties of the single photons generated well below the MOPO threshold. Moreover, at difference with the classical analysis in [1], such a scaling with the pump spectrum is predicted only in rather extreme conditions, corresponding to an ultrashort pump pulse $\tau_p \ll \tau_{gvm}$. Notice that this limit imposes a precise and not trivial constraint on the minimum observable bandwidth of the idler photon: the behavior described by Eq.(3.66) is indeed realized only for $\tau_p \ll \tau_{gvm}$, or for $\Delta\Omega_p \gg \Omega_{gvm}$, so that it requires that the idler bandwidth

$$\delta\Omega_i \simeq \frac{\eta}{1-\eta}\Delta\Omega_p \gg \frac{\eta}{1-\eta}\Omega_{gvm} = \Omega_{gvs} \qquad (3.67)$$

iii) Intermediate pump pulse:

When $\tau_{gvm} \ll \tau_p \ll \tau'_{gvs}$, the properties of the twin photons are actually intermediate between the two former cases, with the forward propagating signal photon replicating the pump spectrum, while the coherence properties of the backward propagating idler are determined by phase matching. These features are clearly exhibited by the central column (b) of Fig.3.4, which plots a numerically computed example of the coherence functions for $\tau_p = 0.04\tau'_{gvs} \approx 4\tau_{gvm}$, short with respect to the transit time along the slab, but long enough

that GVM does not play a relevant role.
The observed features are a straightforward consequence of the separable form (3.39) of the biphoton amplitude which holds in this limit. Indeed, by using Eq.(3.39), in the limit $\tau_p/\tau'_{gvs} \to 0$, $\tau_{gvs}/\tau_p \to 0$ we obtain:

$$G_s^{(1)}(\Omega,\Omega') \approx \frac{g^2}{2\pi}\tilde{\alpha}_p^*[\Omega_s(1-\eta)]\tilde{\alpha}_p[\Omega'_s(1-\eta)]\int d\Omega_i \,\mathrm{Sinc}^2\left(\frac{\Omega_i}{\Omega'_{gvs}}\right). \tag{3.68}$$

Since $\int dx\,\mathrm{Sinc}^2 x = \pi$ we obtain

$$G_s^{(1)}(\Omega,\Omega') \to \frac{g^2\Omega_{gvs}}{2}\tilde{\alpha}_p^*\left[\Omega\,(1-\eta)\right]\tilde{\alpha}_p\left[\Omega'\,(1-\eta)\right]. \tag{3.69}$$

For the idler in a similar way we obtain:

$$G_i^{(1)}(\Omega,\Omega') \to \frac{g^2\tau_p}{\sqrt{2\pi}}\mathrm{Sinc}\left(\frac{\Omega}{\Omega_{gvs}}\right)\mathrm{Sinc}\left(\frac{\Omega'}{\Omega_{gvs}}\right)e^{i\frac{\Omega'-\Omega}{\Omega'_{gvs}}} \tag{3.70}$$

Thus in this case the signal spectrum is a replica of the broad pump spectrum

$$I_s(\Omega) \propto \left|\tilde{\alpha}_p\left[\Omega\,(1-\eta)\right]\right|^2, \tag{3.71}$$

while the idler spectrum is determined by the much narrower phase-matching function

$$I_i(\Omega) \propto \mathrm{Sinc}^2\left(\frac{\Omega}{\Omega_{gvs}}\right), \tag{3.72}$$

as shown in Fig. 3.5.

Precisely, the signal spectrum is described by the same formula (3.65) as in the ultrashort pump case, while the idler spectral properties are described by the same formula (6.5) that holds in the CW pump limit. However, notice that in the present case the coherence properties are remarkably different, as the two coherence functions are perfectly symmetrical along the two diagonals $\Omega \pm \Omega'$: as can be easily inferred from Eqs. (3.69) and (3.70) the two coherence lengths are $l_{coh,s} \approx \Delta\Omega_p$ and $l_{coh,i} \approx \Omega_{gvs}$, i.e. they are equal to the respective spectral widths. This is in accordance with the separability of the biphoton state, which corresponds to single-mode, almost coherent reduced states for each of the two twin photon taken separately.

We conclude this section observing that the results (6.5), (3.67) and (3.70) implies that in any pumping regime the idler bandwidth cannot be narrower than the phase matching

bandwidth Ω_{gvs}, a limitation that arises from the imperfect momentum conservation due to the finite length of the crystal slab.

3.4 Schmidt number of entanglement

So far our considerations about the number of modes and the degree of entanglement of the system have been qualitative. A quantitative measure of the entanglement is offered by the so-called Schmidt number [36, 37], which is recognized to give an estimate of the number of Schmidt modes participating in the entangled state, i.e. of the effective dimensionality of the entanglement [38].

First of all, as usual, we consider the state conditioned to a photon count

$$|\phi_c\rangle = \int d\Omega_s d\Omega_i \Psi(\Omega_s,\Omega_i)\hat{a}_s^\dagger(\Omega_s)\hat{a}_i^\dagger(\Omega_i)\,|0\rangle\ , \tag{3.73}$$

where with respect to the true output state (3.16), the vacuum term has been dropped. Then, we introduce the Schmidt number, as the inverse of the purity of the state of each separate subsystem

$$\mathcal{K} = \frac{1}{\mathrm{T}r\{\rho_s^2\}} = \frac{1}{\mathrm{T}r\{\rho_i^2\}} \tag{3.74}$$

where ρ_s, ρ_i are the reduced density matrix of the signal and idler , e.g. $\rho_s = \mathrm{T}r_i\{|\phi_C\rangle\langle\phi_C|\}$.

We will derive in the following an integral formula for the Schmidt number in the case of a two-particle state of the form (3.73).
First of all the state (3.73) is not normalized, in fact

$$\langle\phi_c|\phi_c\rangle = \int d\Omega_s \int d\Omega_i\ |\Psi(\Omega_s,\Omega_i)|^2 = \int d\Omega\ G_s^{(1)}(\Omega,\Omega) = \int d\Omega\ G_i^{(1)}(\Omega,\Omega) = N. \tag{3.75}$$

The system conditional density matrix is

$$\rho = \frac{|\phi_c\rangle\langle\phi_c|}{\langle\phi_c|\phi_c\rangle} \tag{3.76}$$

and the reduced density matrix of the system 1 (say the signal component) can be calculated (see Appendix A for details) as

$$\rho_1 = Tr_2\{\rho\} = \frac{1}{N}\int d\Omega \int d\Omega'\ G(\Omega,\Omega')A_s^\dagger(\Omega)|0\rangle_{11}\langle 0|A_s(\Omega'). \tag{3.77}$$

Because of the symmetry of the state with respect to $1 \to 2$, the reduced density matrix of the idler component has exactly the same form). Notice that in the limit where the coherence

function become a Dirac delta, which holds in the limit of a monochromatic plane-wave-pump, the reduced density matrix of each subsystem reduces to a sum of projectors onto 1-photon states.
Next we calculate the purity of such a reduced state:

$$Tr_1\{\rho_1^2\} = \frac{1}{N^2}\left[\int d\Omega \int d\Omega' \, |G(\Omega,\Omega')|^2\right]. \tag{3.78}$$

An integral formula for the Schmidt number, as e.g derived in [39] (see also [8]), can be therefore written as:

$$\mathcal{K} = \frac{N^2}{B}, \tag{3.79}$$

where

$$\begin{aligned} B &= \int d\Omega \int d\Omega' \, |G(\Omega,\Omega')|^2 \\ &= \int d\Omega_s \int d\Omega_s' \int d\Omega_i \int d\Omega_i' \;\; \Psi(\Omega_s,\Omega_i)\Psi(\Omega_s',\Omega_i')\Psi^*(\Omega_s,\Omega_i')\Psi^*(\Omega_s',\Omega_i). \end{aligned} \tag{3.80}$$

As can be easily checked, $\mathcal{N}$ is the expectation value (first order moment) of the photon number operator $\hat{N}_j = \int d\Omega \hat{I}_j(\Omega)$ in either the signal or idler arm

$$\mathcal{N} = \langle \hat{N}_s \rangle = \langle \hat{N}_i \rangle \tag{3.81}$$

The quantity at denominator is instead linked to the second order moment of the photon number. By performing the integral of Eq.(3.56) over the two spectral arguments, one gets:

$$B = \int d\Omega \int d\Omega' |G_j^{(1)}(\Omega,\Omega')|^2 = \langle : \hat{N}_j^2 : \rangle - \langle \hat{N}_j \rangle^2 \qquad (j = s,i) \tag{3.82}$$

where the symbol : : indicates normal ordering. In terms of the normalized $g^{(2)}$ coefficient:

$$g^{(2)} = \frac{\langle : \hat{N}_j^2 : \rangle}{\langle \hat{N}_j \rangle^2} = 1 + \frac{1}{\mathcal{K}} \tag{3.83}$$

In this way, as recognized in [40, 41], the Schmidt number can be related to measurable statistical properties of light. In particular, formula (3.83) is well know to describe the statistics of multi-mode thermal light, with $\mathcal{K}$ playing the role of the "degeneracy factor" characterizing the effective number of independent modes in a thermal beam.

Figure 3.6 shows our results for the Schmidt number. The solid lines plot the "exact" results, where $\mathcal{K}$ has been calculated by numerically performing the integrals involved in (3.75), (3.80), with the phase matching calculated via the complete Sellmeier relations. The red dashed lines in plot (a) and (b) are asymptotic behaviors, analytically derived

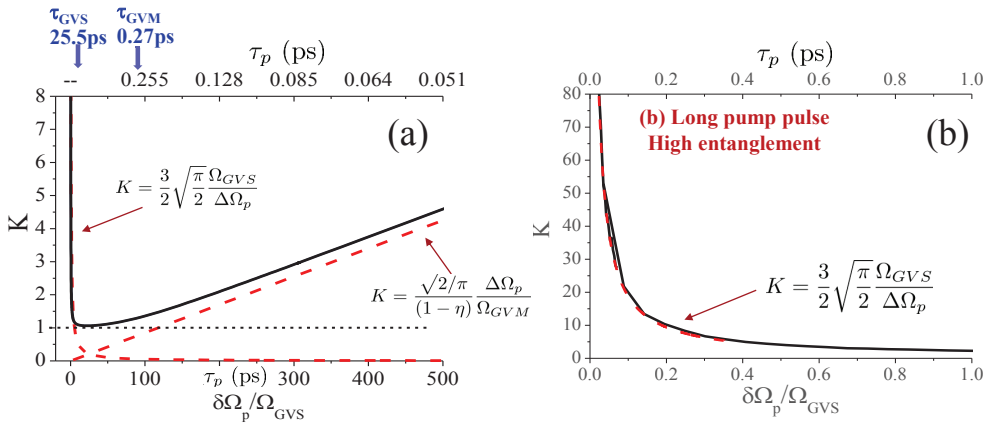

Fig. 3.6 Schmidt number, as a function of the pump spectral bandwidth (lower axis) or duration (upper axis). (b)is an inset of (a), showing the transition from high entanglement for a long pump $\tau_p \gg \tau'_{gvs}$ to an almost separable state for $\tau'_{gvs} \gg \tau_p \gg \tau_{gvm}$. The red dashed lines in (a) and (b) are the calculated asymptotic behaviors. 4 mm PPKTP **A** in Fig.3.1, with $\tau'_{gvs} = 25.5$ ps $\tau_{gvm} = 0.27$ps, $\eta = 0.01$, other parameters as in Fig.3.2

by exploiting the linear approximation for phase matching. In particular, by using the approximated formula (3.3) for the coherence function, and performing the integrals involved in (3.75) and (3.80), one obtains the limit of the Schmidt number for a long pump pulse. In particular:

$$\begin{aligned} N = \int d\Omega_s \, |G_s^{(1)}(\Omega_s, \Omega_s)| &= g^2 \tilde{\mathcal{I}}_p(0) \int d\Omega_s \, \mathrm{Sinc}^2\left(\frac{\Omega_s}{\Omega'_{gvs}}\right) \\ &= g^2 \Omega'_{gvs} \pi \int \frac{dt}{2\pi} \, e^{-\frac{t^2}{\tau_p^2}} \\ &= \frac{\sqrt{\pi}}{2} g^2 \frac{\Omega'_{gvs}}{\Delta\Omega_p}, \end{aligned} \tag{3.84}$$

and, introducing $\delta = \Omega'_s - \Omega_s$

$$B = \int d\Omega_s \int d\Omega'_s \, |G_s^{(1)}(\Omega_s, \Omega'_s)|^2 = g^4 \int d\delta \, |\tilde{\mathcal{I}}_p(\delta)|^2 \int d\Omega_s \, \mathrm{Sinc}^4 \left(\frac{\Omega_s}{\Omega'_{gvs}} \right),$$
$$= \frac{1}{3} \sqrt{\frac{\pi}{2}} g^4 \frac{\Omega'_{gvs}}{\Delta\Omega_p}, \tag{3.85}$$

where we use $\int_{-\infty}^{+\infty} dx \, \mathrm{Sinc}^2 x = \pi$ and $\int_{-\infty}^{+\infty} dx \, \mathrm{Sinc}^4 x = 2\pi/3$. From Eq.(3.79) we thus obtain:

$$\mathcal{K} \overset{\tau_p \gg \tau'_{gvs}}{\longrightarrow} \frac{3}{2} \sqrt{\frac{\pi}{2}} \frac{\Omega'_{gvs}}{\Delta\Omega_p} \tag{3.86}$$

For an ultrashort pump pulse, the asymptotic behavior of $\mathcal{K}$ is calculated by using formula (3.66) or (3.64), for either the signal or the idler coherence function (identical results are indeed obtained). In this case

$$\begin{aligned} N = \int d\Omega_s \, |G_s^{(1)}(\Omega_s, \Omega_s)| &= g^2 \frac{\Omega'_{gvs}}{2} \int d\Omega_s \, |\tilde{\alpha}_p[\Omega(1-\eta)]|^2 \\ &= \frac{g^2}{2} \frac{\Omega'_{gvs}}{(1-\eta)} \frac{\pi}{\Delta\Omega_p} \end{aligned} \tag{3.87}$$

and, introducing $\delta = \Omega'_s - \Omega_s$,

$$B = \int d\Omega_s d\Omega'_s \, |G_s^{(1)}(\Omega_s, \Omega'_s)|^2 = g^4 \frac{\Omega'^2_{gvs}}{4} \int d\delta \, \mathrm{Sinc}^2 \left(\frac{\delta}{\Omega_{gvm}} \right) \int d\Omega_s \, |\tilde{\alpha}_p[\Omega(1-\eta)]|^2,$$
$$= \pi g^4 \frac{\Omega'^2_{gvs}}{4} \frac{\Omega_{gvm}}{1-\eta} \int d\bar{\Omega} \, |\bar{\alpha}_p(\bar{\Omega})|^4,$$
$$= \pi \frac{g^4}{4} \sqrt{\frac{\pi}{2}} \frac{\Omega_{gvm}}{1-\eta} \frac{\Omega'^2_{gvs}}{\delta\Omega_p^3}, \tag{3.88}$$

where we introduced $\bar{\Omega} = \Omega(1-\eta)$. From Eq.(3.79) we thus obtain:

$$\mathcal{K} \overset{\tau_p \ll \tau'_{gvm}}{\longrightarrow} \frac{1}{1-\eta} \sqrt{\frac{2}{\pi}} \frac{\Delta\Omega_p}{\Omega_{gvm}} \tag{3.89}$$

The calculated asymptotes are well in accordance with our qualitative estimates of the number of modes in Sec.3.3, based on the ratio between the spectral bandwidth and the coherence length.

This shape of the curve, showing a minimum of $\mathcal{K}$ for a given value of the pump bandwidth and linear asymptotes at small and large values of the bandwidth, is commonplace, with a

qualitatively similar curve characterizing also the co-propagating case in either temporal [8] or spatial [42] or even spatio-temporal [39] domains. The novelty here is that the minimum value of $\mathcal{K}$ is very close to unity, and remains close to unity for a rather large range of $\Delta\Omega_p$ (see panel (c) in Fig.3.6). This represents indeed a big difference compared to the copropagating case, where in order to generate separable biphotons very special matching conditions have to be chosen, corresponding to a zero group velocity mismatch between the pump and one of the twin photons, which can be realized only in type II interactions [5, 43].

In the backward propagating case the conditions for separability are very easily approached, and rely entirely on the fact that $\eta = \tau_{gvm}/\tau'_{gvs}$ is naturally a very small quantity, because the temporal separations τ_{gvm}, τ'_{gvs} between the co-propagating and the counterpropagating waves are on well separated time scales.

Indeed, a more refined calculation shows that the minimum value of $\mathcal{K}$, reached for a pump duration intermediate between τ_{gvm} and τ'_{gvs} is $K_{min} = 1 + O(\eta)$. Calculations (plotted as the blue dash-dot line in Fig.3.6c) are performed by means of a Gaussian approximation of the Sinc function of phase matching, similarly to what done in [5],

$$\mathrm{Sinc}\frac{D(\Omega_s,\Omega_i)l_c}{2} \approx e^{-\gamma\left(\frac{D(\Omega_s,\Omega_i)l_c}{2}\right)}, \tag{3.90}$$

where γ is an appropriate fitting parameter. Requiring e.g. that the sinc and the Gaussian functions shares the same FWHM, one obtains $\gamma = 0.193$. Considering the pump pulse given by Eq. (3.24) one can obtain the corresponding approximation for the biphoton amplitude:

$$\psi(\Omega_s,\Omega_i) \approx \frac{g\tau_p}{\sqrt{2\pi}} e^{i(\tau_{gvm}\Omega_s + \tau'_{gvs}\Omega_i)} e^{-c_{11}\Omega_s^2 - c_{22}\Omega_i^2 - 2c_{12}\Omega_s\Omega_i}, \tag{3.91}$$

where we introduced the real coefficients

$$c_{11} = \frac{\tau_p^2}{2} + \gamma\tau_{gvm}^2, \tag{3.92}$$

$$c_{22} = \frac{\tau_p^2}{2} + \gamma\tau_{gvs}'^2, \tag{3.93}$$

$$c_{12} = \frac{\tau_p^2}{2} + \gamma\tau_{gvm}\tau'_{gvs}. \tag{3.94}$$

Using approximation (3.91) to calculate the Schmidt number according to Eq. (3.79), we find

$$\mathcal{K} = \sqrt{\frac{c_{11}c_{22}}{c_{11}c_{22} - c_{12}^2}} \tag{3.95}$$

$$= \frac{1}{1-\eta}\sqrt{1 + \eta^2 + \frac{1}{2\gamma}\frac{\tau_p}{\tau'_{gvs}} + 2\gamma\left(\frac{\tau_{gvm}}{\tau_p}\right)^2}. \tag{3.96}$$

As a function of the pump duration τ_p, it is easily seen that $\mathcal{K}$ takes its minimum for

$$\tau_p^{min} = \sqrt{2\gamma|\tau_{gvm}\tau'_{gvs}|}. \tag{3.97}$$

For positive values of η, the minimum of $\mathcal{K}$ is thus given by:

$$\mathcal{K}_{min} = \frac{1+\eta}{1-\eta} \approx 1+2\eta. \tag{3.98}$$

This result suggests that a high degree of purity can be achieved provided $\eta = \tau_{gvm}/tau'_{gvs}$

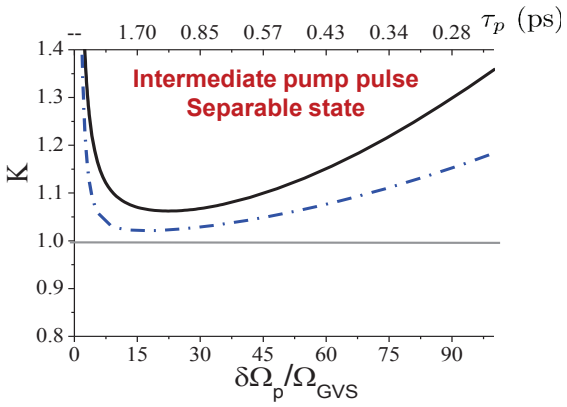

Fig. 3.7 Schmidt number, as a function of the pump spectral bandwidth (lower axis) or duration (upper axis). This graph is an inset of Fig. 3.6(a) , showing the minimum value of the Schmidt number reached for $\tau'_{gvs} \gg \tau_p \gg \tau_{gvm}$, i.e. for an almost separable state. The blue dash-dot line in is the result of a Gaussian approximation. 4 mm PPKTP **A** in Fig.3.1, with $\tau'_{gvs} = 25.5$ ps $\tau_{gvm} = 0.27$ps, $\eta = 0.01$, other parameters as in Fig. 3.2

is sufficiently small. This condition is naturally met in the counter-propagating geometry since the characteristic GVM time between the signal and the pump field, τ_{gvm}, is typically two order of magnitudes smaller than τ'_{gvs} (see Fig. 3.1). Separability is thus nearly complete for pump pulse durations close τ_{min}, within τ_{gvm} and τ_{gvs}, in agreement with the numerical results shown in Fig. 3.6 and the analytical approximation (3.39) or (3.49) for the biphoton correlation.

It is worth to notice that relations (3.97) and (3.98) still hold in the standard copropagating geometry provided τ'_{gvs} is replaced with the GVM time between the idler and the pump field. The condition for obtaining a nearly separable state is in this case far more difficult to satisfy, since the two GVM time scales are generally comparable. As already mentioned, co-propagating twin photons can be prepared in a nearly separable state without resorting to

post-selection only through a careful matching of the group-velocities (see e.g. [5] for more details).

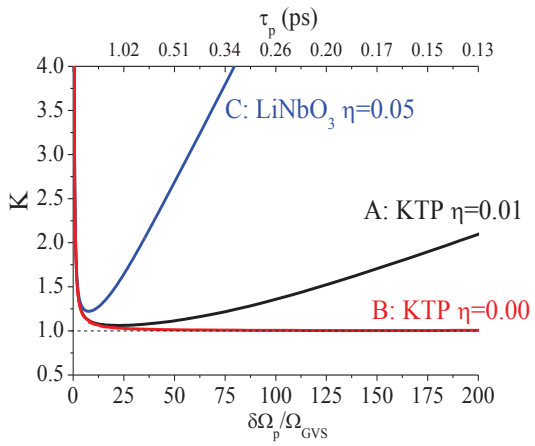

Fig. 3.8 Role of GVM in determining the purity of the state: Schmidt number for different crystals and/or different phase matching conditions, corresponding to the points **A**, **B**, **C** in Fig.3.1: **A**) 4 mm KTP with τ_{gvm}=0.27ps, τ'_{gvs}=25.5ps, $\rightarrow \eta = 0.01$ (same as in Figs.3.2-3.6).**B**) 4 mm KTP, with τ_{gvm}=0, τ'_{gvs}=24.7ps, $\rightarrow \eta = 0$. **C**) 4 mm $LiNbO_3$ with τ_{gvm}=1.68ps, τ'_{gvs}=31.2ps, $\rightarrow \eta = 0.05$

Chapter 4

Stimulated pair production regime

In this chapter we investigate the coherence and correlation properties of the twin beams generated in the MOPO below threshold, pumped by a stationary monochromatic field. In particular the analysis is devoted to the transition from the regime far from threshold, where purely spontaneous downconversion is the main source of twin photon pairs, up to a regime close to threshold where the combined effect of stimulated PDC and distributed feedback affects dramatically the properties of the light source. In the last section of the chapter we give an intuitive picture explaining the transition between these two regimes and illustrate the divergence of the correlation time and the critical slowing down phenomenon of temporal fluctuations occurring when approaching the transition towards coherent oscillations.

In order to perform an analytical treatment of the propagation equations (3.4), we limit ourselves to the case of a perfectly monochromatic pump wave of frequency ω_p, assuming its intensity is sufficiently far from the MOPO threshold so that the undepleted pump approximation holds. Accordingly, we treat the pump field as a classical c-number field [see Eq. (3.3)] by setting

$$\alpha_p(\Omega, z=0) = \alpha_p \sqrt{2\pi}\delta(\Omega). \tag{4.1}$$

In this limit, the linearized propagation equations (3.4) reduce to

$$\begin{aligned} \frac{\partial}{\partial z}\hat{a}_s(\Omega,z) &= \sqrt{2\pi}\bar{\sigma}\alpha_p \int d\Omega'\ \delta(\Omega+\Omega')\hat{a}_i^\dagger(\Omega',z)e^{-iD(\Omega,\Omega')z} \\ &= \sqrt{2\pi}\bar{\sigma}\alpha_p \hat{a}_i^\dagger(-\Omega,z)e^{-iD(\Omega,-\Omega)z} \qquad (4.2a) \\ \frac{\partial}{\partial z}\hat{a}_i(\Omega,z) &= -\sqrt{2\pi}\bar{\sigma}\alpha_p \int d\Omega'\ \delta(\Omega+\Omega')\hat{a}_s^\dagger(\Omega',z)e^{-iD(\Omega',\Omega)z} \\ &= -\sqrt{2\pi}\bar{\sigma}\alpha_p \hat{a}_s^\dagger(-\Omega,z)e^{-iD(-\Omega,\Omega)z}, \qquad (4.2b) \end{aligned}$$

where we introduced the phase-mismatch function in the perfectly monochromatic pump limit

$$\bar{D}(\Omega) := D(\Omega,-\Omega) = k_s(\Omega) - k_i(-\Omega) - k_p + k_G, \tag{4.3}$$

and the dimensionless parametric gain

$$g = \sqrt{2\pi}\bar{\sigma}|\alpha_p| l_c, \tag{4.4}$$

the propagation equations, in the plane wave pump approximation (PWP), thus read:

$$\frac{\partial}{\partial z}\hat{a}_s(\Omega,z) = +\frac{g}{l_c}\hat{a}_i^\dagger(-\Omega,z)e^{-i\bar{D}(\Omega)z}e^{i\phi_p} \tag{4.5a}$$

$$\frac{\partial}{\partial z}\hat{a}_i(\Omega,z) = -\frac{g}{l_c}\hat{a}_s^\dagger(-\Omega,z)e^{-i\bar{D}(-\Omega)z}e^{i\phi_p} \tag{4.5b}$$

where $\phi_p = \arg[\alpha_p]$ is the pump phase at $z = 0$. Taking the conjugate of the second equation, with the substitution $\Omega \to -\Omega$, we finally obtain:

$$\frac{\partial}{\partial z}\hat{a}_s(\Omega,z) = +\frac{g}{l_c}\hat{a}_i^\dagger(-\Omega,z)e^{-i\bar{D}(\Omega)z}e^{i\phi_p} \tag{4.6a}$$

$$\frac{\partial}{\partial z}\hat{a}_i^\dagger(-\Omega,z) = -\frac{g}{l_c}\hat{a}_s(\Omega,z)e^{i\bar{D}(\Omega)z}e^{-i\phi_p}. \tag{4.6b}$$

The system boundary conditions differ from those found in more common co-propagating geometries. The input field operators, assumed in the vacuum state, are indeed defined at different transverse planes: the left face of the crystal $(z = 0)$ for the forward propagating signal wave and the right face $(z = l_c)$ for the back-propagating idler wave.

$$\overline{a}_s(\Omega, z = 0) = \overline{a}_s^{\text{in}}(\Omega) \tag{4.7a}$$

$$\overline{a}_i(\Omega, z = l_c) = \overline{a}_i^{\text{in}}(\Omega). \tag{4.7b}$$

We have then a signal field that is injected at the input face of the crystal $z = 0$ in its vacuum state and propagates from the left to the right and an idler field which is injected at the output face of the crystal $z = l_c$ and propagates in the opposite direction.

We perform a rotating frame transformation in order to eliminate the exponential terms:

$$\hat{a}_s(\Omega,z) = \overline{a}_s(\Omega,z)e^{-i\frac{\bar{D}(\Omega)}{2}z}e^{i\phi_p} \tag{4.8a}$$

$$\hat{a}_i^\dagger(-\Omega,z) = \overline{a}_i^\dagger(-\Omega,z)e^{i\frac{\bar{D}(\Omega)}{2}z}e^{-i\phi_p}. \tag{4.8b}$$

Substituting these expressions into Eq. (4.6) and writing them in the matricial form we obtain:

$$\frac{\partial}{\partial z}\begin{bmatrix} \overline{a}_s(\Omega,z) \\ \overline{a}_i^{\dagger}(-\Omega,z) \end{bmatrix} = \begin{bmatrix} i\frac{\bar{D}(\Omega)}{2} & +\frac{g}{l_c} \\ -\frac{g}{l_c} & -i\frac{\bar{D}(\Omega)}{2} \end{bmatrix}\begin{bmatrix} \overline{a}_s(\Omega,z) \\ \overline{a}_i^{\dagger}(-\Omega,z) \end{bmatrix}. \tag{4.9a}$$

The eigenvalues associated to this linear system are found to be

$$\lambda_{1,2} = \pm i\frac{\gamma(\Omega)}{l_c}, \quad \text{with } \gamma(\Omega) = \sqrt{g^2 + \frac{\bar{D}^2(\Omega)l_c^2}{4}} > 0. \tag{4.10}$$

Noticing that $\lambda_{1,2}$ are purely imaginary at all frequencies, we look for solutions of the form:

$$\begin{cases} \overline{a}_s(\Omega,z) = c_1\cos\left(\frac{\gamma}{l_c}z\right) + s_1\sin\left(\frac{\gamma}{l_c}z\right) \\ \overline{a}_i^{\dagger}(-\Omega,z) = c_2\cos\left(\frac{\gamma}{l_c}z\right) + s_2\sin\left(\frac{\gamma}{l_c}z\right). \end{cases} \tag{4.11}$$

with the constants c_1, c_2, s_1 and s_2 which are to be determined imposing the boundary conditions (4.7). In particular

$$\begin{cases} \overline{a}_s(\Omega, z=0) = c_1 \\ \overline{a}_i^{\dagger}(-\Omega, z=0) = c_2. \end{cases} \tag{4.12}$$

Taking the derivatives of (4.11) and using Eqs. (4.5b)

$$\left.\frac{\partial\overline{a}_s(\Omega,z)}{\partial z}\right|_{z=0} = \frac{\gamma}{l_c}s_1 = i\frac{\overline{D}}{2}\overline{a}_s(\Omega,0) + \frac{g}{l_c}\overline{a}_i^{\dagger}(-\Omega,0) \tag{4.13a}$$

$$\left.\frac{\partial\overline{a}_i(-\Omega,z)}{\partial z}\right|_{z=0} = \frac{\gamma}{l_c}s_2 = -i\frac{\overline{D}}{2}\overline{a}_i^{\dagger}(-\Omega,0) - \frac{g}{l_c}\overline{a}_s(\Omega,0) \tag{4.13b}$$

From which we obtain [taking into account definition (4.7)]

$$s_1 = i\frac{\overline{D}l_c}{2\gamma}\overline{a}_s(\Omega,0) + \frac{g}{\gamma}\overline{a}_i^{\dagger}(-\Omega,0) \tag{4.14a}$$

$$s_2 = -i\frac{\overline{D}l_c}{2\gamma}\overline{a}_i^{\dagger}(-\Omega,0) + \frac{g}{\gamma}\overline{a}_s(\Omega,0) \tag{4.14b}$$

Coming back to Eq. (4.11) and substituing the constants c_1, c_2, s_1, s_2, it is possible to derive a general expression for the field operators at a generic z:

$$\overline{a}_s(\Omega,z) = \left[\cos\left(\frac{\gamma}{l_c}z\right) + i\frac{\bar{D}}{2\gamma}\sin\left(\frac{\gamma}{l_c}z\right)\right]\overline{a}_s(\Omega,0) + \frac{g}{\gamma}\sin\left(\frac{\gamma}{l_c}z\right)\overline{a}_i^\dagger(-\Omega,0) \tag{4.15}$$

$$\overline{a}_i^\dagger(-\Omega,z) = \left[\cos\left(\frac{\gamma}{l_c}z\right) - i\frac{\bar{D}}{2\gamma}\sin\left(\frac{\gamma}{l_c}z\right)\right]\overline{a}_i^\dagger(-\Omega,0) - \frac{g}{\gamma}\sin\left(\frac{\gamma}{l_c}z\right)\overline{a}_s^\dagger(\Omega,0). \tag{4.16}$$

Setting $z = l_c$ in these equations, some simple manipulation allows to express the output field $\hat{a}_s^{\text{out}} = \overline{a}_s(\Omega, l_c)$ and $\hat{a}_i^{\text{out}} = \overline{a}_i(\Omega,0)$ in terms of the input field $\hat{a}_s^{\text{in}} = \overline{a}_s(\Omega,0)$, $\hat{a}_i^{\text{in}} = \overline{a}_i(\Omega,l_c)$ in the form of a unitary Bogoliubov transformation.

$$\hat{a}_s^{\text{out}}(\Omega) = U_s'(\Omega)\hat{a}_s(\Omega) + V_s'(\Omega)\hat{a}_i^\dagger(-\Omega) \tag{4.17a}$$

$$\hat{a}_i^{\text{out}}(\Omega) = U_i'(\Omega)\hat{a}_i(\Omega) + V_i'(\Omega)\hat{a}_s^\dagger(-\Omega) \tag{4.17b}$$

with

$$U_s'(\Omega) = \frac{1}{\cos\gamma(\Omega) - i\frac{\bar{D}(\Omega)l_c}{2\gamma(\Omega)}\sin\gamma(\Omega)}e^{-i\frac{\bar{D}(\Omega)l_c}{2}} \tag{4.18a}$$

$$V_s'(\Omega) = g\frac{\sin\gamma(\Omega)}{\gamma(\Omega)}\frac{1}{\cos\gamma(\Omega) - i\frac{\bar{D}(\Omega)l_c}{2\gamma(\Omega)}\sin\gamma(\Omega)}e^{i\phi_p}e^{-i\bar{D}(\Omega)l_c} \tag{4.18b}$$

$$U_i'(\Omega) = \frac{1}{\cos\gamma(-\Omega) + i\frac{\bar{D}(-\Omega)l_c}{2\gamma(-\Omega)}\sin\gamma(-\Omega)}e^{i\frac{\bar{D}(-\Omega)}{2}l_c} \tag{4.18c}$$

$$V_i'(\Omega) = g\frac{\sin\gamma(-\Omega)}{\gamma(-\Omega)}\frac{1}{\cos\gamma(-\Omega) + i\frac{\bar{D}(-\Omega)l_c}{2\gamma(-\Omega)}\sin\gamma(-\Omega)}e^{i\phi_p}. \tag{4.18d}$$

Considering the complete field operators [see Eq. (1.39)]

$$\hat{A}_s^{\text{out}}(\Omega) = e^{ik_s(\Omega)l_c}\hat{a}_s^{\text{out}}(\Omega) \tag{4.19a}$$

$$\hat{A}_i^{\text{out}}(\Omega) = \hat{a}_i^{\text{out}}(\Omega). \tag{4.19b}$$

the unitary Bogoliubov transformation takes the form, equivalent to the one in [33]:

$$\hat{A}_s^{\text{out}}(\Omega) = U_s(\Omega)\hat{A}_s^{\text{in}}(\Omega) + V_s(\Omega)\hat{A}_i^{\text{in}\dagger}(-\Omega) \tag{4.20a}$$

$$\hat{A}_i^{\text{out}}(\Omega) = U_i(\Omega)\hat{A}_i^{\text{in}}(\Omega) + V_i(\Omega)\hat{A}_s^{\text{in}\dagger}(-\Omega). \tag{4.20b}$$

If we introduce the functions $\phi(\Omega)$, $\beta(\Omega)$, and $\gamma(\Omega)$, defined by:

$$\phi(\Omega) = \frac{1}{\cos\gamma(\Omega) - i\frac{\bar{\mathcal{D}}(\Omega)l_c}{2\gamma(\Omega)}\sin\gamma(\Omega)} \tag{4.21}$$

$$\beta(\Omega) = [k_s(\Omega) + k_i(-\Omega) - (k_s + k_i)]\frac{l_c}{2} \tag{4.22}$$

$$\gamma(\Omega) = \sqrt{g^2 + \frac{\bar{\mathcal{D}}^2(\Omega)l_c^2}{4}}, \tag{4.23}$$

the gain coefficients $U(\Omega)$ and $V(\Omega)$ can be written as trigonometric functions of the form:

$$U_s(\Omega) = e^{ik_s l_c} e^{i\beta(\Omega)}\phi(\Omega) \tag{4.24a}$$

$$V_s(\Omega) = e^{i(k_s - k_i)l_c} g e^{i\phi_p}\frac{\sin\gamma(\Omega)}{\gamma(\Omega)}\phi(\Omega) \tag{4.24b}$$

$$U_i(\Omega) = e^{ik_i l_c} e^{i\beta(-\Omega)}\phi^*(-\Omega) \tag{4.24c}$$

$$V_i(\Omega) = g e^{i\phi_p}\frac{\sin\gamma(-\Omega)}{\gamma(-\Omega)}\phi^*(-\Omega) \tag{4.24d}$$

and satisfy the following unitarity conditions

$$|U_j(\Omega)|^2 - |V_j(\Omega)|^2 = 1, \qquad j = s,i \tag{4.25a}$$

$$U_s(\Omega)V_i(-\Omega) = U_i(-\Omega)V_s(\Omega) \tag{4.25b}$$

Notice that $U_j(\Omega)$ and $V_j(\Omega)$ diverge when approaching $g = \pi/2$, the value of the parametric gain corresponding to the MOPO threshold in the stationary CW pump regime [27].

4.1 Coherence and correlation

The quantity of primary interest, which characterizes the twin beams correlation in the spectral domain, is the so-called biphoton correlation:

$$\psi(\Omega_s, \Omega_i) \equiv \langle \hat{A}_s^{\text{out}}(\Omega_s)\hat{A}_i^{\text{out}}(\Omega_i)\rangle. \tag{4.26}$$

This definition is substantially equivalent to the one in (3.17), a part from a phase factor $e^{ik_s l_c}$ which is taken into account in the definition of the input-output functions (4.24) just for convenience of notation.

Assuming that the signal and the idler input fields are in the vacuum state, and using the input-output relations written in Eq. (4.20), we obtain the following expression for the

biphoton correlation:

$$\psi(\Omega_s,\Omega_i) = \delta(\Omega_s+\Omega_i)U_s(\Omega_s)V_i(-\Omega_s) \tag{4.27}$$

$$= \delta(\Omega_s+\Omega_i)e^{i[\phi_p+k_s l_c]}e^{i\beta(\Omega)}\bar{\psi}(\Omega_s), \tag{4.28}$$

where the $\delta(\Omega_s+\Omega_i)$ function expresses the perfect signal-idler frequency correlation of the monochromatic pump limit. Here we introduced the spectral correlation density

$$\bar{\psi}(\Omega_s) = g\,\mathrm{sinc}[\gamma(\Omega_s)]|\phi(\Omega)|^2 \tag{4.29}$$

$$= g\,\mathrm{sinc}[\gamma(\Omega_s)]\left[1+|V_s(\Omega_s)|^2\right]. \tag{4.30}$$

The last identity has been obtained from the explicit expression of $U_s(\Omega)$ and $V_i(\Omega)$ given in Eqs. (4.24) and the unitarity condition (4.25).

Other important quantities are the signal and idler coherence functions

$$G_j^{(1)}(\Omega_j,\Omega_j') = \langle \hat{A}_j^{\dagger\mathrm{out}}(\Omega_j)\hat{A}_j^{\mathrm{out}}(\Omega_j')\rangle \quad j=s,i \tag{4.31}$$

This definition is equivalent to the one in (3.52,3.53) a part from a phase factor.

From the input-output relations (4.20) it is possible to obtain the following expression for the coherence function:

$$\langle A_s^{\dagger\mathrm{out}}(\Omega_s)A_s^{\mathrm{out}}(\Omega_s')\rangle = \delta(\Omega_s-\Omega_s')|V_s(\Omega_s)|^2 \tag{4.32}$$

$$= \langle A_i^{\dagger\mathrm{out}}(-\Omega_s)A_i^{\mathrm{out}}(-\Omega_s')\rangle. \tag{4.33}$$

We wish also to investigate the behavior of these quantities in the time domain. Precisely, introducing the output temporal fields $\hat{A}_j^{\mathrm{out}}(t) = \int \frac{d\Omega}{\sqrt{2\pi}}e^{-i\Omega t}\hat{A}_j^{\mathrm{out}}(\Omega)$, it is possible to write the temporal correlation as:

$$\psi(t_s,t_i) \equiv \langle \hat{A}_s^{\mathrm{out}}(t_s)\hat{A}_i^{\mathrm{out}}(t_i)\rangle \tag{4.34}$$

$$= ge^{i[\phi_p+k_s l_c]}\int\frac{d\Omega}{2\pi}e^{-i\Omega(t_s-t_i)}\left\{e^{i\beta(\Omega)}\times\mathrm{sinc}[\gamma(\Omega)][1+|V_s(\Omega)|^2]\right\}. \tag{4.35}$$

This function represents the probability amplitude of finding a signal and idler photon at their exit faces at times t_s,t_i. The temporal coherence is in turn characterized by

$$G_s^{(1)}(t_s,t_s') \equiv \langle \hat{A}_s^{\dagger\mathrm{out}}(t_s)\hat{A}_s^{\mathrm{out}}(t_s')\rangle \tag{4.36}$$

$$= \int\frac{d\Omega}{2\pi}e^{i\Omega(t_s-t_s')}|V_s(\Omega)|^2 = G_i^{(1)}(t_s',t_s). \tag{4.37}$$

Note that both ψ and $G^{(1)}$ depend only on the difference $t_s - t'_s$, as it should be for a stationary model.

Approximated analytical expressions of these quantities can be obtained both in the purely spontaneous regime (for $g \ll \frac{\pi}{2}$) and close to the threshold (for $g \to \frac{\pi}{2}$) by considering the behavior of the intensity spectrum in these two important limiting cases. The purely spontaneous regime is quite straightforward and it is given by

$$S(\Omega) \equiv |V_s(\Omega)|^2 = \frac{4g^2 \sin^2 \gamma(\Omega)}{\bar{\mathcal{D}}^2(\Omega) l_c^2 + 4g^2 \cos^2 \gamma(\Omega)} \tag{4.38}$$

$$\xrightarrow{g \to 0} g^2 \mathrm{sinc}^2 \frac{\bar{\mathcal{D}}(\Omega) l_c}{2}. \tag{4.39}$$

In order to obtain the limit close to the threshold (for $g \to \frac{\pi}{2}$) we apply the following expansion of

$$\cos^2 \gamma(\Omega) = \cos^2 \sqrt{g^2 + \left(\frac{\bar{\mathcal{D}} l_c}{2}\right)^2}$$

in even power of $\bar{\mathcal{D}} l_c/2$

$$\cos^2 \gamma(\Omega) = \cos^2 g - \frac{\sin g \cos g}{g} \left(\frac{\bar{\mathcal{D}}(\Omega) l_c}{2}\right)^2 + \mathcal{O}\left(\frac{\bar{\mathcal{D}}(\Omega) l_c}{2}\right)^4. \tag{4.40}$$

for evaluating the denominator of the spectrum $|V_s(\Omega)|^2$ given by relation (4.38). Keeping only term up to second order we obtain the following approximated expression

$$S(\Omega) = |V_s(\Omega)|^2 \approx \frac{\sin^2 \gamma(\Omega)}{\cos^2 g} \frac{1}{1 + \frac{2 - \sin 2g}{2g^2 \cos^2 g} \left(\frac{\bar{\mathcal{D}}(\Omega) l_c}{2}\right)^2} \qquad \text{for } |\bar{\mathcal{D}}(\Omega) l_c| \ll 1 \tag{4.41}$$

which holds for small value of the phase-mismatch. The key factor lies in that the multiplicative factor of $\bar{\mathcal{D}}^2(\Omega) l_c^2/4$ becomes very large close to threshold, having in this limit

$$\frac{2 - \sin 2g}{2g^2 \cos^2 g} \approx \frac{4}{\pi^2 \varepsilon^2} \gg 1 \quad \text{for } \varepsilon = \frac{\pi}{2} - g \ll 1. \tag{4.42}$$

As a consequence, the spectrum $|V_s(\Omega)|^2$ is already reduced by a factor $1/\varepsilon^2 \gg 1$ with respect to its peak value $\tan^2 g$ as soon as the phase-mismatch becomes on the order of unity,

i.e for $|\bar{\mathcal{D}}(\Omega)l_c| \sim 1$. It is thus legitimate to use the following approximation

$$S(\Omega) = |V(\Omega)|^2 \approx \frac{\sin^2\gamma(\Omega=0)}{\cos^2 g} \frac{1}{1-\frac{2-\sin 2g}{2g^2\cos^2 g}\left(\frac{\bar{\mathcal{D}}(\Omega)l_c}{2}\right)^2} \tag{4.43}$$

$$\approx \frac{4g^2\sin^2 g}{4g^2\cos g + \bar{\mathcal{D}}^2(\Omega)l_c^2} \tag{4.44}$$

where in the last approximation we took into account that the multiplicative factor of $(\bar{\mathcal{D}}(\Omega)l_c/2)^2$ is almost equal to unity when $g \to \pi/2$. Though strictly valid only for frequencies satisfying the condition $|\bar{\mathcal{D}}(\Omega)l_c/2| \ll 1$ for which $\mathrm{sinc}\gamma(\Omega) := \mathrm{sinc}\sqrt{g^2+(\bar{\mathcal{D}}l_c/2)^2} \approx \mathrm{sinc}\, g$, relation (4.44) can be extended to the whole frequency domain for the purpose of analytical calculations. According to the previous discussion, $|V_s|^2$ seen as a function of $\bar{\mathcal{D}}l_c/2$ is indeed negligible everywhere except for a narrow neighborhood of width $\sim \varepsilon$ around $\bar{\mathcal{D}}l_c = 0$. This neighborhood translates to a frequency interval on the order of $\varepsilon\,\Omega_{gvs}$ when the linear approximation for the phase-matching function (4.49) is taken into account.

We can write:

$$S(\Omega) \equiv |V_s(\Omega)|^2 = \frac{4g^2\sin^2\gamma(\Omega)}{\bar{\mathcal{D}}^2(\Omega)l_c^2 + 4g^2\cos^2\gamma(\Omega)} \tag{4.45}$$

$$\approx \begin{cases} g^2\mathrm{sinc}^2\dfrac{\bar{\mathcal{D}}(\Omega)l_c}{2} & \text{for } g \to 0 \quad (4.46) \\ \dfrac{4g^2\sin^2 g}{\bar{\mathcal{D}}^2(\Omega)l_c^2 + 4g^2\cos^2 g} & \text{for } g \to \frac{\pi}{2} \quad (4.47) \end{cases}$$

Performing the expansion of the phase-matching function $\bar{\mathcal{D}}(\Omega)$ (4.3) and keeping terms up to the first order (phase matching bandwidths in the counterpropagating case are in fact extremely narrow) we obtain the approximated relation:

$$\frac{\bar{\mathcal{D}}(\Omega)l_c}{2} = \frac{l_c}{2}(k_s' + k_i')\Omega + \frac{l_c}{4}(k_s'' - k_i'')\Omega^2 + \cdots \tag{4.48}$$

$$\approx \frac{\Omega}{\Omega_{gvs}}, \tag{4.49}$$

where

$$\Omega_{gvs}^{-1} \equiv \tau_{gvs} = \frac{1}{2}\left[\frac{l_c}{v_{gs}} + \frac{l_c}{v_{gi}}\right]. \tag{4.50}$$

The inverse τ_{gvs} of the characteristic bandwidth Ω_{gvs} involves the sum of the inverse group velocities rather than their difference: τ_{gvs} is on the order of the photon transit time across the crystal and represents the typical time delay between counter-propagating twin photon in

the spontaneous regime. As we shall see in the next section, in this regime Ω_{gvs} represents the width of the PDC spectrum.

Another useful approximation needed to perform analytical calculations is the linearization of the phase (4.22) of the biphoton spectral correlation (4.26)

$$\beta(\Omega) \simeq (k_s' - k_i')\frac{l_c}{2}\Omega = \Delta t_A \Omega. \tag{4.51}$$

Here

$$|\Delta t_A| = \left| \frac{l_c}{2v_{gs}} - \frac{l_c}{2v_{gi}} \right| \ll \tau_{gvs} \tag{4.52}$$

represents the difference of the transit times along the crystal for a pair of counter propagating signal and idler photons generated at the crystal center at the reference frequencies.

4.2 Low gain regime, $g \ll \frac{\pi}{2}$

We start our analysis from the low gain regime, i.e. $g \ll \frac{\pi}{2}$, where the dominant process is the spontaneous production of photon pairs and distributed feedback does not enter into play.

4.3 Biphoton correlation

We consider first the field correlation defined by Eq. (4.26) and given by expression (4.28). In the regime of purely spontaneous PDC, $|V_s(\Omega)|^2$ is on the order of $g^2 \ll 1$ according to Eq. (4.39). Its contribution in the expression of the correlation density (4.30) is therefore negligible and we have in this limit:

$$\lim_{g\to 0} \bar{\psi}(\Omega_s) = g \,\mathrm{sinc}\left(\frac{\bar{\mathcal{D}}(\Omega_s) l_c}{2}\right) \tag{4.53}$$

$$\approx g \,\mathrm{sinc}\left(\frac{\Omega_s}{\Omega_{gvs}}\right), \tag{4.54}$$

where in the last equality we used the linearized approximation for the phase-matching (4.49).

The temporal correlation can be calculated by Fourier transforming the spectral correlation [see Eq. (4.35)]. By using the approximations (4.51) and (4.54) we recover the result of Suhara for the temporal correlation in the coincidence count regime [33]. It is given by the

box-shaped temporal correlation of width $2\tau_{gvs}$:

$$\psi(\Delta t) = g e^{i[k_s l_c + \phi_p]} \int \frac{d\Omega}{2\pi} e^{-i\Omega(\Delta t - \Delta t_A)} \mathrm{sinc}\left(\frac{\Omega}{\Omega_{gvs}}\right) \tag{4.55}$$

$$= g \frac{e^{i[k_s l_c + \phi_p]}}{2\tau_{gvs}} \mathrm{Rect}\left[\frac{\Delta t - \Delta t_A}{2\tau_{gvs}}\right], \tag{4.56}$$

with $\Delta t = t_s - t_i$.

This function describes a flat distribution of the temporal delays Δt between the signal and idler arrival times, ranging between $-\tau_{gvs} + \Delta t_A = -\frac{l_c}{v_{gi}}$ and $\tau_{gvs} + \Delta t_A = \frac{l_c}{v_{gs}}$. As it will be further discussed in Sec. 4.8, this flat distribution reflects the spontaneous character of the emission in the low gain regime: each photon pair is generated independently from the others, and the process can take place at any point of the crystal with uniform probability.

The red curve in Fig. 4.1b is the approximate solution (4.56), the blue curve is obtained from the numerical integration of Eq. (4.35). All the numerical examples reported here and in the following have been obtained for a 4 mm long KTP crystal using the Sellmeier dispersion formula found in [23, 35]. Here we consider the same configuration as in [1]: Type 0 $e \to ee$ phase matching for $\lambda_p = 821.4$nm, $\lambda_s = 1.141$nm, $\lambda_i = 2.932$nm. In this configuration $\tau_{gvs} = 25.2$ps, $\Delta t_A = -0.55$ps.

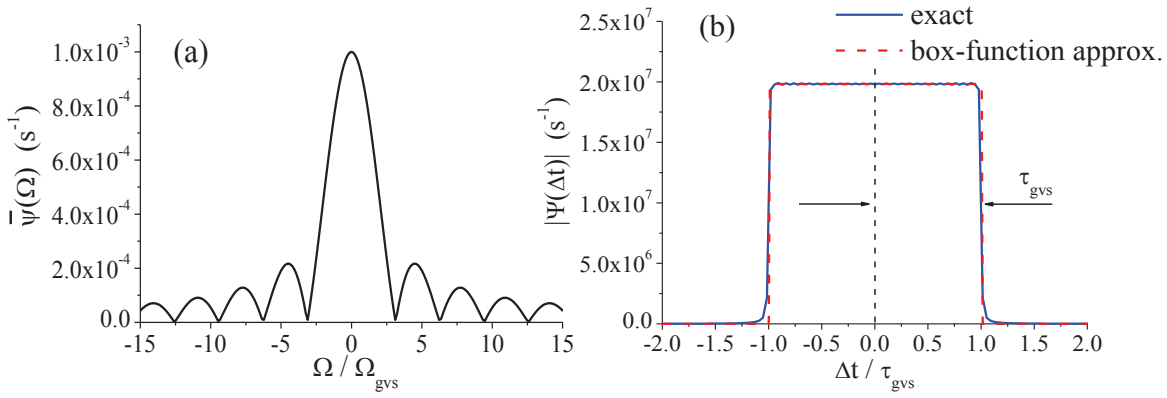

.

Fig. 4.1 Biphoton correlation in the spontaneous PDC regime with $g = 10^{-3}$ (a) in the spectral and (b) in the temporal domain. In all the figures "exact" refers to results obtained from the input-output relations (4.20), without the use of the linear approximations (4.49,4.52)

4.4 Coherence function

In the purely spontaneous regime, the signal and idler spectra [Eq.(4.38)] are well approximated by Eq.(4.39) and (4.49):

$$S(\Omega) = |V_s(\Omega)|^2 \approx g^2 \operatorname{sinc}^2\left(\frac{\Omega}{\Omega_{gvs}}\right) \tag{4.57}$$

and exhibit the usual squared sinc shape characteristic of the coincidence count regime of PDC.

The coherence function in the time domain is obtained by Fourier transforming the spectrum [Eq.(4.57)].

Using the identity

$$\operatorname{sinc}(u) = \frac{1}{2}\int_{-1}^{1} e^{iut}dt, \tag{4.58}$$

the Fourier transform of the spectrum in the coincidence count regime can be written as

$$G_s^{(1)}(\Delta t) = \int \frac{d\Omega}{2\pi} e^{i\Omega\Delta t}|V(\Omega)|^2 \tag{4.59}$$

$$= g^2 \int \frac{d\Omega}{2\pi} e^{i\Omega\Delta t}\operatorname{sinc}^2(\tau_{gvs}\Omega) \tag{4.60}$$

$$= \frac{g^2}{4}\int_{-1}^{1} ds \int_{-1}^{1} ds' \int \frac{d\Omega}{2\pi} e^{i[s\tau_{gvs}+s'\tau_{gvs}+\Delta t]\Omega} \tag{4.61}$$

Using the relation $\int_{-\infty}^{\infty} e^{ius}ds = 2\pi\delta(u)$ and making the substitution $t' = s'\tau_{gvs}$ for the evaluation of the integral in s' we find

$$G_s^{(1)}(\Delta t) = \frac{g^2}{4\tau_{gvs}}\int_{-1}^{1} ds \int_{-\tau_{gvs}}^{\tau_{gvs}} dt\, \delta(t + s\tau_{gvs} + \Delta t) \tag{4.62}$$

$$= \frac{g^2}{4\tau_{gvs}}\int_{-1}^{1} ds \operatorname{Rect}\left(\frac{s - \Delta t/\tau_{gvs}}{2}\right)\operatorname{Rect}\left(\frac{s}{2}\right) \tag{4.63}$$

$$= \frac{g^2}{2\tau_{gvs}} T\left(\frac{\Delta t}{2\tau_{gvs}}\right), \tag{4.64}$$

where T is the triangular function defined by:

$$T(x) = \begin{cases} 1 - |x| & \text{if } x \in (-1,1) \\ 0 & \text{elsewhere} \end{cases} \tag{4.65}$$

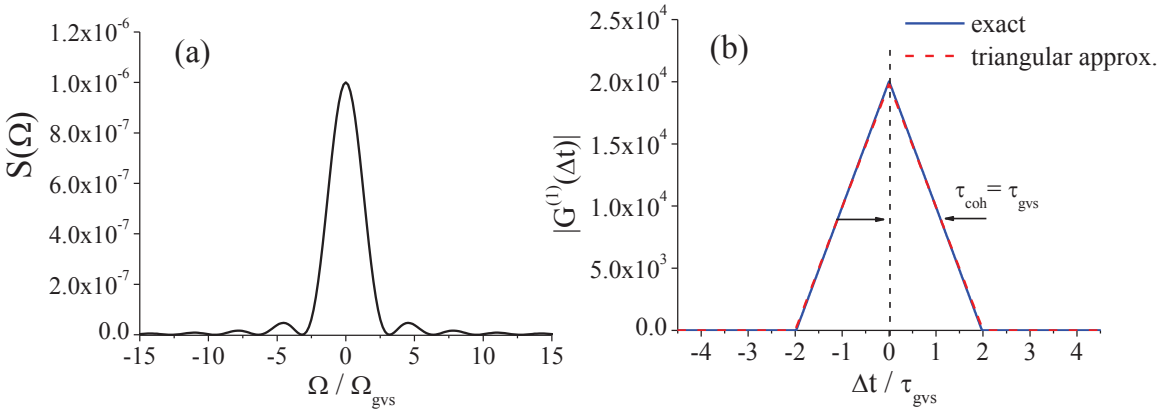

Fig. 4.2 (a) PDC spectrum at the crystal output faces in the low gain regime, (b) coherence function in the time domain. In both cases $g = 10^{-3}$.

and has the shape of a triangle of base $(-2\tau_{gvs}, 2\tau_{gvs})$. Therefore the coherence time, taken as the HWHM of the coherence function, is given by half of the sum of the propagation times of the signal and idler photons along the crystal

$$\tau_{coh} = \tau_{gvs}. \tag{4.66}$$

4.5 High-gain regime (threshold region), $g \to \frac{\pi}{2}$

We now consider the regime of stimulated PDC, which occurs when approaching the MOPO threshold from below, i.e. for small positive value of $\varepsilon = \frac{\pi}{2} - g$. In this regime, the spectrum is well approximated by the Lorentzian function:

$$\lim_{g\to\pi/2} |V_s(\Omega)|^2 = \frac{g^2 \sin^2 g}{(\Omega^2/\Omega_{gvs}^2) + g^2 \cos^2 g}, \tag{4.67}$$

as can be inferred from Eqs. (4.44) and (4.49). Such a Lorentzian is characterized by a peak of width (half width at half maximum)

$$\Delta\Omega_L = \Omega_{gvs} g \cos g \approx \frac{\pi\varepsilon}{2}\Omega_{gvs} \to 0, \quad \text{for } \varepsilon \to 0 \tag{4.68}$$

which shrinks progressively as the threshold is approached.

4.6 Field correlation

Based on the Lorentzian approximation (4.67) for $|V_s(\Omega)|^2$ valid close to threshold, we can write the spectral correlation density in Eq. (4.30) as

$$\bar{\psi}(\Omega_s) \approx g\,\mathrm{sinc}[\gamma(\Omega_s)]\left[1+\frac{g^2\sin^2 g}{(\Omega_s^2/\Omega_{gvs}^2)+g^2\cos^2 g}\right] \tag{4.69}$$

$$\approx g\,\mathrm{sinc}[\gamma(\Omega_s)]+\frac{g^2\sin^3 g}{(\Omega_s^2/\Omega_{gvs}^2)+g^2\cos^2 g}, \tag{4.70}$$

where in the last line we substituted $g\,\mathrm{sinc}[\gamma(\Omega_s)]$ in the second term with $\sin g$, since the $\mathrm{sinc}[\gamma(\Omega_s)]$ varies on a scale Ω_{gvs} which is much broader than the narrow width $\Delta\Omega_L \approx \frac{\pi\varepsilon}{2}\Omega_{gvs}$ of the Lorentzian close to threshold. The contribution of stimulated PDC, which increases dramatically close to threshold because of distributed feedback, is responsible of the emergence of this extremely narrow peak [second term in Eq. (4.70)]. In contrast the smaller contribution [first term in Eq. (4.70)], similar to the one found in the low gain regime (4.54), originates from purely spontaneous PDC and extends on a much broader emission bandwidth on the order of Ω_{gvs}. Figure 4.3a and 4.3b show the spectral density correlation at an intermediate gain regime and close to threshold respectively. In the latter case the narrow Lorentzian contribution of width $\Delta\Omega_L$ [second term of Eq. (4.70)] is clearly dominant with respect to the purely spontaneous contribution. Using approximation (4.70), we find the following expression for the twin beam correlation in the temporal domain:

$$\psi(\Delta t) \approx g e^{i[k_s l_c+\phi_p]}\left\{\int\frac{d\Omega}{2\pi}e^{-i\Omega(\Delta t-\Delta t_A)}\mathrm{sinc}\left[\gamma(\Omega)\right] + \int\frac{d\Omega}{2\pi}e^{-i\Omega(\Delta t-\Delta t_A)}\frac{g^2\sin^3 g}{\tau_{gvs}^2\Omega^2+g^2\cos^2 g}\right\}, \tag{4.71}$$

where $\Delta t = t_s - t_i$. The first term in Eq. (4.71) is on the order of g/τ_{gvs} and originates from purely spontaneous PDC. The peak value of the second term is $g/(2\tau_{gvs}\cos g) \approx g/(2\tau_{gvs}\varepsilon) \to \infty$ for $\varepsilon \to 0$, and therefore dominates over the first. Thus, we rewrite the biphoton amplitude in a compact form close to threshold, neglecting the spontaneous PDC emission term:

$$\psi(\Delta t) = \frac{g^2\sin^3 g}{2\pi\tau_{gvs}^2}e^{ik_s l_c}\int d\Omega\,\frac{e^{i\Omega\bar{t}}}{\Omega^2+\xi^2}, \tag{4.72}$$

Here we have introduced the simplified notation $\bar{t} = \Delta t - \Delta t_A$ and $\xi = \frac{g\cos g}{\tau_{gvs}}$ and, as already stated, we have set the sinc function equal to $\mathrm{sinc}\,\xi\,(\Omega = 0) = \mathrm{sinc}\,g$ as its width is larger than that of the Lorentzian by a factor $\varepsilon \ll 1$. We can evaluate the integral using the residues

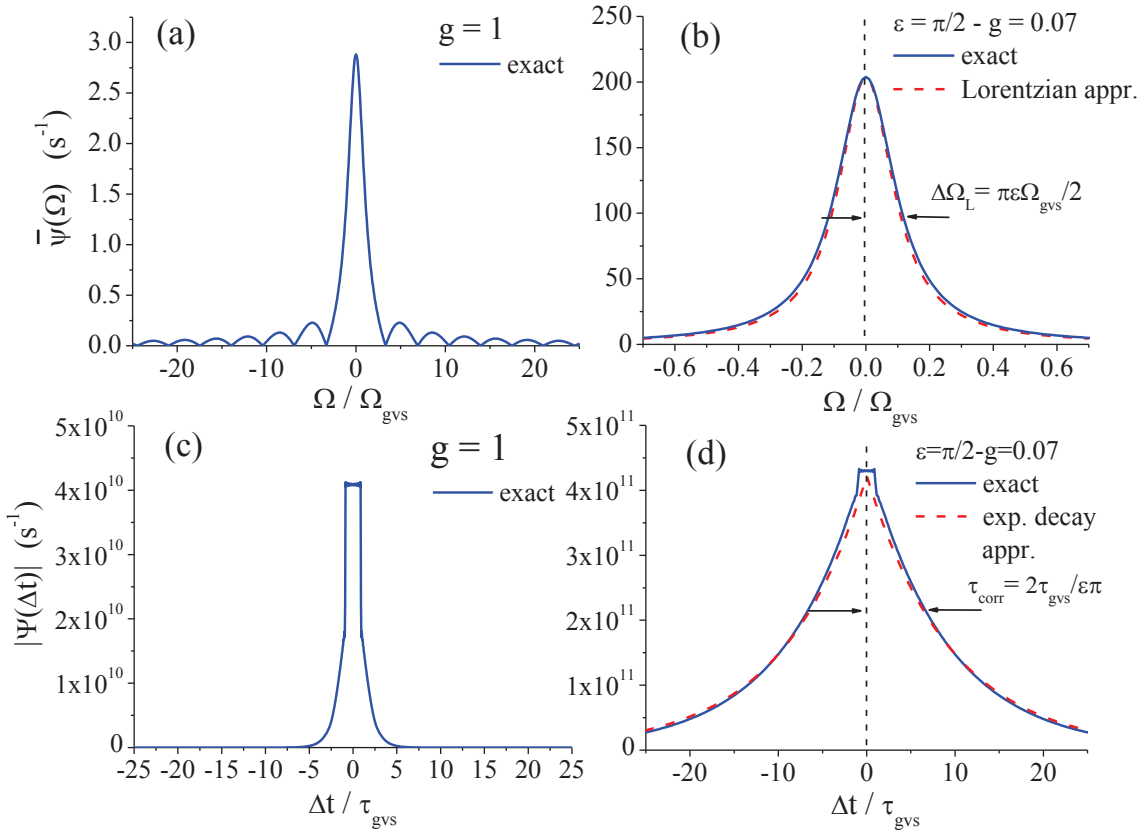

Fig. 4.3 Spectral correlation density (a) at intermediate gain regime ($g = 1$) with both stimulated and spontaneous PDC contributing equally. (b) Close to threshold ($\varepsilon = \pi/2 - g = 0.07$) where stimulated PDC is dominant. Biphoton correlation in the temporal domain (c) at intermediate gain and (d) close to threshold.

method: the analytical continuation of the Lorentizan function in the complex plane has the two poles at $\Omega = \pm i\xi$. For $\bar{t} > 0$ we consider a counter-clockwise contour in the upper-half plane and only the residue at $\Omega = +i\xi$ gives a contribution:

$$\int_{-\infty}^{+\infty} d\Omega \frac{e^{i\Omega\bar{t}}}{\Omega^2+\xi^2} = 2\pi i \sum_{\mathrm{Re}[\Omega]>0} \mathrm{Res}\left[\frac{e^{i\Omega\bar{t}}}{\Omega^2+\xi^2}\right] \tag{4.73a}$$

$$= 2\pi i \mathrm{Res}\left[\frac{e^{i\Omega\bar{t}}}{(\Omega+i\xi)(\Omega-i\xi)}\right]_{\Omega=i\xi} \tag{4.73b}$$

$$= \frac{\pi}{\xi} e^{-\Omega\xi\bar{t}} \tag{4.73c}$$

Similarly, for $\bar{t} < 0$ we consider a clockwise contour in the lower-half plane and only the residue at $\Omega = -i\xi$ contributes to the integral:

$$\int_{-\infty}^{+\infty} d\Omega \frac{e^{i\Omega\bar{t}}}{\Omega^2+\xi^2} = \frac{\pi}{\xi} e^{\Omega\xi\bar{t}} \tag{4.74}$$

The result for both positive and negative values of $\bar{t}$ can thus be written as:

$$\int_{-\infty}^{+\infty} d\Omega \frac{e^{i\Omega\bar{t}}}{\Omega^2+\xi^2} = \frac{\pi}{\xi} e^{\Omega\xi|\bar{t}|} \tag{4.75}$$

Finally, inserting this result in Eq. (4.72) and substituting the values for $\bar{t}$ and ξ, we obtain the approximation (4.76) for the biphoton amplitude close to the MOPO threshold.

Thus, close to threshold, we approximately have

$$\psi(\Delta t) \approx \frac{e^{i[k_s l_c+\phi_p]}}{2\tau_{gvs}} \frac{g\,\sin^3 g}{\cos g} e^{-g\cos g\frac{|\Delta t-\Delta t_A|}{\tau_{gvs}}}. \tag{4.76}$$

The correlation time which characterizes the decaying exponential in Eq. (4.76)

$$\tau_{corr} = \frac{\tau_{gvs}}{g\cos g} \approx \frac{2\tau_{gvs}}{\pi\varepsilon} \to \infty \quad \text{for} \quad \varepsilon \to 0. \tag{4.77}$$

goes to infinity for $\varepsilon \to 0$, a feature which reflects the establishment of a feedback effect (see Sec. 4.8) and which is typical in phase transitions. This behavior is illustrated in Figs. 4.3c - 4.3d which display the temporal correlation. In the intermediate regime (Fig. 4.3c) where spontaneous and stimulated PDC contribute equally, tails reminiscent of the exponential decay found close to threshold emerge at the basis of the box-shaped correlation characterizing spontaneous PDC. Close to threshold (Fig. 4.3d) the size of those tails strongly increases and the correlation is well approximated by the dominant stimulated PDC contribution (4.76).

4.7 Coherence function

Close to threshold the PDC emission spectra of the signal and idler fields are well approximated by the Lorentzian function written in Eq. (4.67). The spectrum peak value $|V_s(\Omega=0)|^2 = \tan^2 g$ diverges for $g \to \frac{\pi}{2}$, while its width shrinks to zero for $\varepsilon \to 0$, as for the biphoton correlation, as shown in Fig. 4.4a. Clearly, this description will loose its validity for small but finite values of ε, when pump depletion enters into play.

By performing the Fourier transform of the Lorentzian spectrum (4.67) we obtain the temporal coherence function in the time domain within the same order of approximation:

$$G_s^{(1)}(\Delta t) = \frac{g}{2\tau_{gvs}} \frac{\sin^2 g}{\cos g} e^{-g\cos g \frac{|\Delta t|}{\tau_{gvs}}}. \tag{4.78}$$

In contrast to the low gain limit described in Sec. 4.2, as the MOPO threshold is approached, $G^{(1)}(\Delta t)$ becomes almost indistinguishable from the biphoton correlation (4.76), apart from the small temporal shift Δt_A related to the different group velocities of the signal and the idler fields. Approaching threshold, thus, the coherence and the correlation reflect one the properties of the other because of the cascading processes characteristic of the stimulated regime of pair production. The coherence time which characterizes the decaying exponential in Eq. (4.78) is the same of the correlation time defined in Eq. (4.77) and goes to infinity for $\varepsilon \to 0$, i.e.

$$\tau_{coh} \approx \frac{\tau_{gvs}}{g\cos g} \approx \frac{2\tau_{gvs}}{\varepsilon\pi} \xrightarrow{\varepsilon\to 0} \infty \tag{4.79}$$

Figure 4.4 shows (a) the progressive narrowing of the spectrum and (b) the correspondent broadening of the temporal coherence function for decreasing values of ε, a clear manifestation of the critical slowing down of field fluctuations occurring close to threshold.

4.8 An intuitive picture

In this section we want to give an intuitive explanation of the results obtained in sections VI and VII.

Fig. 4.5 schematically represents in the (z,t)-plane the propagation of photon pairs originating from a PDC event occurring at time $t = 0$. It considers both a regime of purely spontaneous PDC (Fig. 4.5a) and a regime of higher parametric gain where secondary processes due to stimulated PDC take place (Fig. 4.5b).

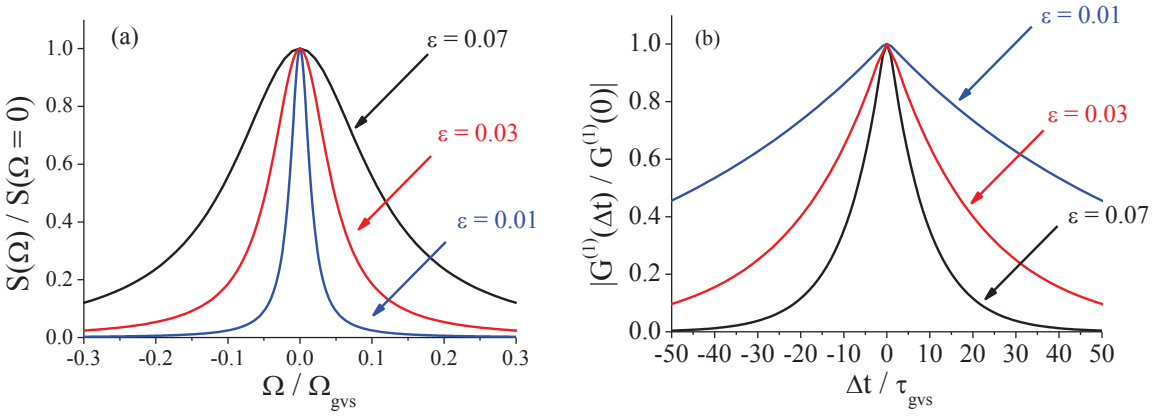

Fig. 4.4 (a) Spectrum and (b) temporal coherence function for decreasing values of $\varepsilon = \pi/2 - g$. The curves in (b) have been obtained through the numerical evaluation of the integrals in Eq. (4.37).

In the first case (Fig. 4.5a), the temporal delay $\Delta t = t_s - t_i$ between the arrival times of the twin photons at their output faces cannot be larger than $\approx \tau_{gvs}$. If the photon pair is produced close to the crystal center $z = \frac{l_c}{2}$, the two counter-propagating photons exit the crystal almost simultaneously (more precisely with a small delay $\Delta t_A = \frac{l_c}{v_{gs}} - \frac{l_c}{v_{gi}}$ due to a possible mismatch of their group velocities). If the pair is produced at $z = l_c$, the signal exits immediately, and the idler arrives at its exit face at $t = l_c/v_{gi}$, thus $\Delta t = -l_c/v_{gi}$. If the pair is produced at $z = 0$, conversely, the idler exits immediately while the signal exits the crystal at $t = l_c/v_{gs}$, thus $\Delta t = +l_c/v_{gs}$. The difference of the arrival times is thus strictly within the interval $\left[-\frac{l_c}{v_{gi}}, \frac{l_c}{v_{gs}}\right] = [\Delta t_A - \tau_{gvs}, \Delta t_A + \tau_{gvs}] \approx [-\tau_{gvs}, \tau_{gvs}]$, since $\Delta t_A \ll \tau_{gvs}$. Well below threshold, where stimulated PDC is negligible, each photon pair is generated independently from the others and the probability of generating a pair is uniform along the crystal length. As a consequence, the distribution of time delays between the two extrema is flat, which explains the box-shaped correlation function displayed in Fig. 4.1b.

When stimulated PDC becomes relevant, the range of allowed values of Δt is no more strictly limited to the interval $[-\frac{l_c}{v_{gi}}, \frac{l_c}{v_{gs}}]$. This is shown in Fig. 4.5b where a few secondary processes take place triggered by the first spontaneous pair. It is clear from this picture that the exit times of a signal and an idler photon originating from two different elementary processes can differ by a value greater than τ_{gvs}. If we look for example at photons i and s'', we notice that the increase of the correlation time beyond τ_{gvs} originates from the backpropagation of photon i'. Therefore, the increase of correlation time can be attributed to the effects of the distributed feedback, created by the combination of backpropagation and stimulated pair generation. The situation described in Fig. 4.5b corresponds to an intermediate gain regime

where purely spontaneous and stimulated pairs contribute to the same extent and the biphoton correlation retains its box shaped structure, but with tails developing at the basis, as in the example of Fig. 4.3c.
When approaching threshold ($g \to \frac{\pi}{2}$) stimulated pair production becomes the dominant mechanism, and a correlation between the signal and idler fields is transferred back and forth along the crystal because of the cascading processes. The closer the threshold, the longer the chain of cascading processes, and the longer becomes the correlation time. In this conditions, the correlation function exhibits the exponential decay shown in Fig. 4.3d [see Eq. (4.76)], with a correlation time in principle approaching infinity [Eq. (4.77)].

The same feedback mechanism is responsible for the increase of the coherence time on approaching the threshold. A correlation among signal photons (photons s, s',...,s''' in Fig. 4.5b) or idler photons (photons i, i',...,i'''), generated in different elementary processes exists only because of stimulated PDC, and the coherence time increases as more and more processes are cascaded. Close to threshold, the coherence function is also well approximated by a decaying exponential [see Eq.(4.78) and Fig.4.4b]. Its characteristic decay time $\tau_{coh} = \tau_{corr}$ becomes much larger than τ_{gvs} for $g \to \frac{\pi}{2}$ [Eq. 4.79)], as the number of secondary events increases dramatically when approaching the MOPO threshold.

In this way, the onset of coherence above the MOPO threshold is anticipated below threshold by longer and longer coherence times, in principle approaching infinity, which originate from the distributed feedback estabilished by backpropagation in the stimulated gain regime.

4.9 Numerical simulations, crossing the threshold

In this section we present some preliminary numerical investigation illustrating the behavior of the MOPO emission during the transition from below to above threshold. Our aim is to solve the nonlinear propagation equation (1.47) written for the corresponding c-number fields $a_j(\Omega, z)$.

$$\frac{\partial}{\partial z} a_{s+}(\boldsymbol{w}, z) = +\sigma \int d\boldsymbol{w'} a_p(\boldsymbol{w}+\boldsymbol{w'}, z) a^*_{i-}(\boldsymbol{w'}, z) e^{-iD(\boldsymbol{w},\boldsymbol{w'})z} \tag{4.80a}$$

$$\frac{\partial}{\partial z} a_{i-}(\boldsymbol{w}, z) = -\sigma \int d\boldsymbol{w'} a_p(\boldsymbol{w}+\boldsymbol{w'}, z) a^*_{s+}(\boldsymbol{w'}, z) e^{-iD(\boldsymbol{w'},\boldsymbol{w})z} \tag{4.80b}$$

$$\frac{\partial}{\partial z} a_{p+}(\boldsymbol{w}, z) = -\sigma \int d\boldsymbol{w'} a_{s+}(\boldsymbol{w'}, z) a_{i-}(\boldsymbol{w}-\boldsymbol{w'}, z) e^{iD(\boldsymbol{w'},\boldsymbol{w}-\boldsymbol{w'})z}. \tag{4.80c}$$

In our numerical model the injected pump beam is treated as a classical coherent field while the vacuum fluctuations at the signal and idler input plane are simulated with Gaussian white

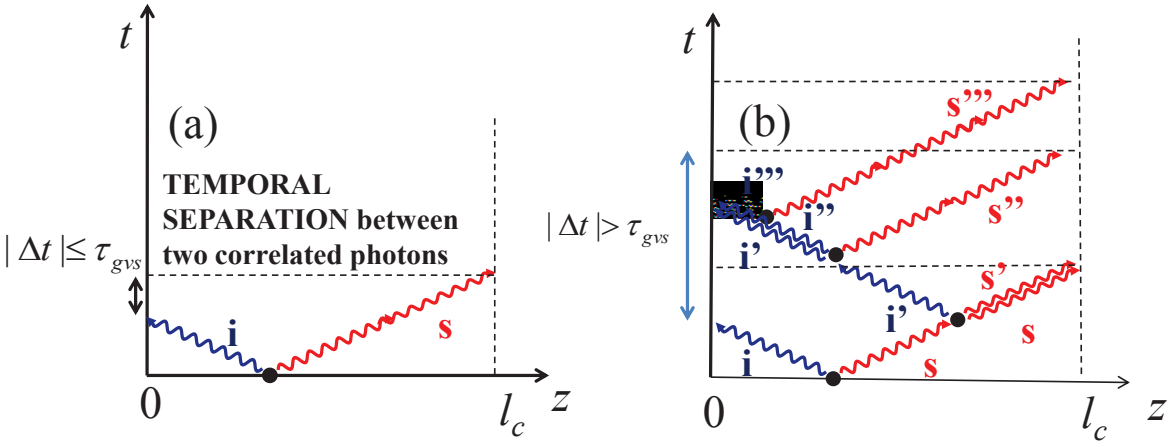

Fig. 4.5 Photon pairs originating from a first PDC event at $t = 0$ (a) in the purely spontaneous regime and (b) in an intermediate regime where secondary events are triggered by the first one. In case (a) the temporal delay $|\Delta t|$ between the arrival times of two correlated photons cannot exceed τ_{gvs}, because they originate from the same PDC event. In case (b) $|\Delta t|$ can exceed τ_{gvs} due to secondary processes.

noise corresponding to the vacuum fluctuations in the Wigner representation framework [44]. The boundary conditions imposed by the counterpropagating configuration requires the use of an iterative integration scheme which is illustrated in the next section.

In order to separate the linear and the nonlinear part of Eqs. (1.47), we consider the transformation

$$b_s(\Omega,z) = e^{i\delta k_{sz}(\Omega)z} a_s(\Omega,z), \tag{4.81a}$$
$$b_i(\Omega,z) = e^{i-\delta k_{iz}(\Omega)z} a_i(\Omega,z), \tag{4.81b}$$
$$b_p(\Omega,z) = e^{i\delta k_{pz}(\Omega)z} a_p(\Omega,z), \tag{4.81c}$$

where $\delta k_{jz} = k_{jz}(\Omega) - k_j$ $(j = p,s,i)$. The propagation equations for the new fields become:

$$\frac{\partial}{\partial z} b_s(\Omega,z) = i\delta k_s(\Omega) b_s(\Omega,z) + \sigma \int d\Omega' b_p(\Omega+\Omega',z) b_i^*(\Omega',z), \tag{4.82a}$$
$$\frac{\partial}{\partial z} b_i(\Omega,z) = -i\delta k_i(\Omega) b_i(\Omega,z) - \sigma \int d\Omega' b_p(\Omega+\Omega',z) b_s^*(\Omega',z), \tag{4.82b}$$
$$\frac{\partial}{\partial z} b_p(\Omega,z) = i\delta k_p(\Omega) b_p(\Omega,z) - \sigma \int d\Omega' b_s(\Omega',z) b_i(\Omega-\Omega',z). \tag{4.82c}$$

A common way to numerically solve a system of nonlinear partial differential equations is to perform a split-step method in order to treat the linear and the nonlinear parts of the equations separately. In particular Eqs. (4.82) can be rewritten in the form

$$\frac{\partial}{\partial z} b(\Omega, z) = (\mathcal{L} + \mathcal{N}) b(\Omega, z), \tag{4.83}$$

where $\mathcal{L}$ and $\mathcal{N}$ are operators that represents respectively the linear and the nonlinear part of the equation. Applying both operators at once is not possible during numerical integration. An obvious shortcut will be to apply the operators in turn as follows

$$b(\Omega, z + \Delta z) = e^{\mathcal{L}\Delta z} e^{\mathcal{N}\Delta z} b(\Omega, z). \tag{4.84}$$

However, this may drastically decrease accuracy of the numerical solution as the linear and nonlinear operators do not commute: it can be showed that $e^{(\mathcal{L}+\mathcal{N})\Delta z} = e^{\mathcal{L}\Delta z} \cdot e^{\mathcal{N}\Delta z} + O(z^2)$, where the $O(z^2)$ term is equal to zero only if $\mathcal{L}$ and $\mathcal{N}$ commute. The operation performed in Eq.(4.84) is called *Lie splitting*. The local truncation error $O(z^2)$ can be reduced to $O(z^3)$ by using the symmetric *Strang splitting* [45]:

$$b(\Omega, z + \Delta z) = e^{\mathcal{L}\frac{\Delta z}{2}} e^{\mathcal{N}\Delta z} e^{\mathcal{L}\frac{\Delta z}{2}} b(\Omega, z). \tag{4.85}$$

We perform the linear step in the frequency domain and the nonlinear in the time domain, exploiting the fact that the convolution integral reduce to simple products in direct space. The scheme is the following: we start with the three input fields (a_s, a_i, a_p) in the temporal domain, with a_s, a_i simulated by Gaussian noise. We perform a Fourier transform of each field (we use FFT for this purpose) and we compute the half linear step in the frequency domain. After that we back-transform the fields and compute the nonlinear evolution with a finite different method (we use a second-order Runge-Kutta method). Then we perform again a Fast Fourier Transform coming back to the frequency domain and compute the final half linear step. If we repeat this cycle for increasing steps in z we can find the evolution of the fields along the crystal.

The main problem to face in implementing the code is represented by the fact that signal and idler field propagates in opposite direction with respect to the pump and the signal, so that the boundary conditions for the signal a_s, the idler field a_i, and the pump field a_p are

defined on different planes (4.7)

$$a_p(z=0,t) = \bar{a}_p(t) \quad \text{(coherent field)} \tag{4.86a}$$
$$a_s(z=0,t) = \bar{a}_p(t) \quad \text{(vacuum field)} \tag{4.86b}$$
$$a_p(z=l_c,t) = \bar{a}_p(t) \quad \text{(vacuum field).} \tag{4.86c}$$

Accordingly, the split-step algorithm for the idler field must be applied starting from its input value at $z = l_c$ and marching backward till $z = 0$, while the signal and pump fields are integrated forward from $z = 0$ to $z = l_c$. Because of the counterpropagating geometry, it is not possible to implement the usual forward marching integration schemes commonly adopted for unidirectional propagation, since fields values that have not yet been evaluated are needed when applying each integration step (4.85). For this reason we have to resort to an iterative method, starting from an initial guess for the three fields along the propagation axis z. The simplest choice for this initial guess is to extend the input field (4.86) to the whole crystal length $0 < z < l_c$. We then apply the split-step algorithm in order to evaluate a first approximation for the three fields, integrating forward from the $z = 0$ for the pump and the signal fields, backward from $z = l_c$ for the idler field so that boundary conditions (4.86) are automatically satisfied. The procedure is then repeated iteratively using each times the new found values of the fields until convergence is attained.

A schematic view of the iterative method can be given by:

$$b_s^{(n)}(z_j+\Delta z) = \hat{S}_s(\Delta z)\left\{b_s^{(n-1)}(z_j)\right\} \qquad z_j = 0,\cdots,l_c \tag{4.87a}$$
$$b_i^{(n)}(z_j-\Delta z) = \hat{S}_i(-\Delta z)\left\{b_i^{(n-1)}(z_j)\right\} \qquad z_j = l_c,\cdots,0 \tag{4.87b}$$
$$b_p^{(n)}(z_j+\Delta z) = \hat{S}_p(\Delta z)\left\{b_p^{(n-1)}(z_j)\right\} \qquad z_j = 0,\cdots,l_c \tag{4.87c}$$

where n is the index of the iterative cycle and

$$\hat{S}_j(\Delta z) = e^{\mathcal{L}_j\frac{\Delta z}{2}} e^{\mathcal{N}_j\Delta z} e^{\mathcal{L}_j\frac{\Delta z}{2}} \quad \text{where } j = p,s,i. \tag{4.88}$$

The expectation values of the observables of interest are then evaluated by performing averages over different realizations obtained by changing the initial vacuum noise.

We present here some preliminary simulations obtained by considering a stationary CW pump. With respect to a pulsed regime, this configuration is less demanding in terms of CPU time and also offers the possibility to check the validity of the numerical method below threshold, where an analytical solution is known.

Fig. (4.6) shows the PDC intensity spectrum defined in Eq. 4.44 for two different gain values, $g = 1.0$ (intermediate gain regime), $g = \pi/2 - 0.07$ (high gain regime). We thus see that below threshold the numerical algorithm reproduces almost exactly the analytical results found in the previous chapters.

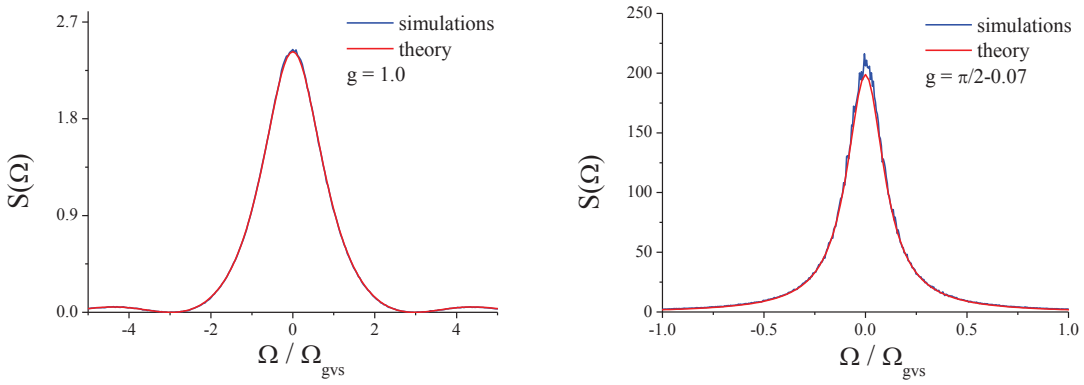

Fig. 4.6 PDC spectrum at the crystal exit faces for $g = 1.0$ and $g = \pi/2 - 0.07$. The comparison between the analytical results [see Eq. (4.44)] and the numerical ones shows a good agreement.

We are interested in studying the region beyond threshold where no analytical results are known except for the mean photon fluxes intensity predicted from the classical model (2.24). With the numerical algorithm we can reproduce for example the result obtained for the pump depletion, which is shown in Fig. 4.7. We see that the agreement between analytical and numerical results is good in the region over the threshold up to gains $g \lesssim 2.5$, while over this critical value of the gain the iterative methods does not converge toward a stationary solution. Further investigations are needed in order to establish whether this unstable behavior originates from shortcoming of our numerical method or has some deeper physical meaning.

The spectra over the threshold region are shown in Fig. 4.8, for three different values of the gain. Conversely to what we obtained in the previous chapter, where we showed a narrowing of the spectra when approaching the threshold for coherent emission, here we predict a broadening of the spectra moving away from the threshold. The spectra are shown in Fig. 4.8: Concerning the correlation function, its behavior is substantially identical to the coherence spectra shown in Fig. 4.8, since they reflect one the properties of the other because of the cascading processes characteristic of the stimulated regime of pair production.

We can notice that the broadening of the spectra over the threshold seems to be symmetrical with respect to the narrowing below threshold, as shown in Fig. 4.9. Notice also that the

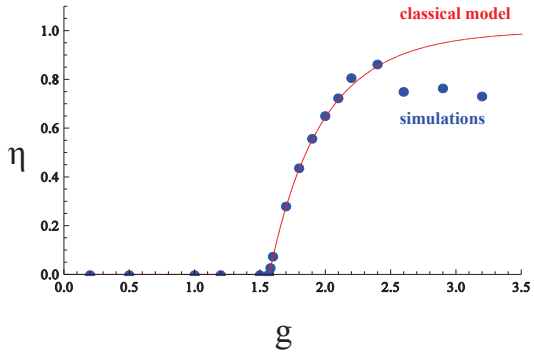

Fig. 4.7 Pump depletion η as a function of the parametric gain g evaluated from Eq. (2.24) (red line), and via the numerical algorithm (blue dotted line).

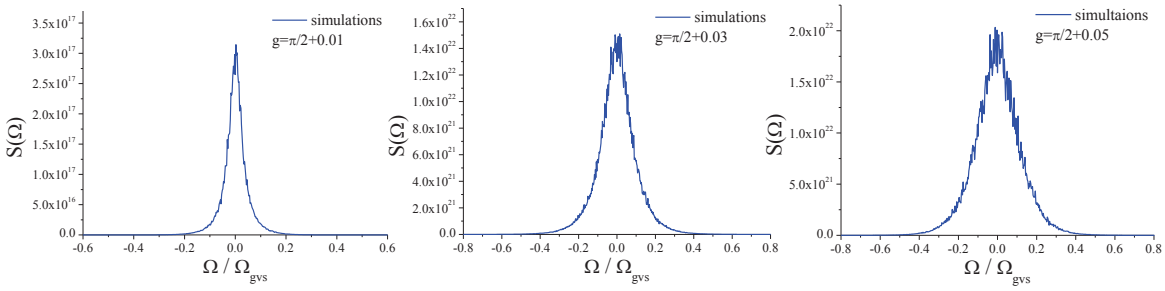

Fig. 4.8 Spectra over threshold for increasing values of $\varepsilon = \pi/2 - g$. The curves have been obtained through the numerical iterative algorithm.

spectra FWHM obtained numerically (blue square) fits very well the analytical prediction (4.68) below threshold (red dashed line).

While the evolution of the spectra and of the correlation function approaching threshold from the below follows a quite intuitive behavior, justified in the previous section, we do not have a straightforward physical explanation for the behavior of the spectra beyond threshold and further investigations are needed in order to characterize the properties of coherence and correlation of the generated twin beams.

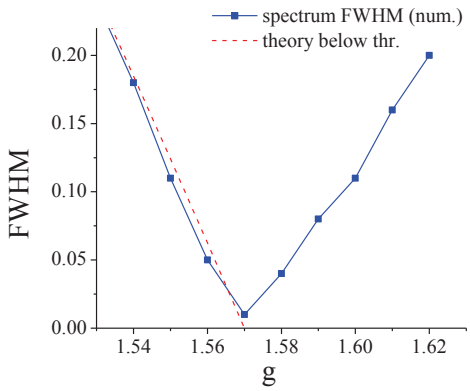

Fig. 4.9 Evolution of the FWHM of the emission spectra crossing threshold. The red dashed line represents the analytical prediction (4.68) below threshold.

The algorithm in principle allows to investigate also the case of an undepleted pump, but further investigations are required.

Chapter 5

Quadrature correlations in the MOPO below threshold

In this chapter we turn our attention to the genuinely quantum characteristic of the source in the vicinity of the threshold, namely to its potentiality to generate Einstein-Podolsky-Rosen (EPR) correlations [46] in the vicinity of the threshold. As for any down-conversion process, also for this particular configuration it is possible to obtain nonclassical correlation into a pair of orthogonal field quadratures of the degenerated twin beams [47], which can be large enough to provide a realization of the original EPR paradox. In particular the backward geometry exhibits the presence of the threshold so that the quantum noise is allowed to diverge in proper observables, allowing noise suppression in the conjugate observable.

In order to detect EPR correlations, we need to perform measurements of the field quadratures that, in the time domain, for the individual signal and idler fields, are defined by the relations:

$$\hat{X}_s(t) = \hat{A}_s^{\text{out}}(t)e^{-i\phi_s} + \hat{A}_s^{\text{out}\dagger}(t)e^{+i\phi_s} \tag{5.1a}$$

$$\hat{Y}_s(t) = \frac{\hat{A}_s(t)^{\text{out}}e^{-i\phi_s} - \hat{A}_s^{\text{out}\dagger}(t)e^{+i\phi_s}}{i} \tag{5.1b}$$

$$\hat{X}_i(t) = \hat{A}_i^{\text{out}}(t)e^{-i\phi_i} + \hat{A}_i^{\text{out}\dagger}(t)e^{+i\phi_i} \tag{5.1c}$$

$$\hat{Y}_i(t) = \frac{\hat{A}_i^{\text{out}}(t)e^{-i\phi_i} - \hat{A}_i^{\text{out}\dagger}(t)e^{+i\phi_i}}{i}. \tag{5.1d}$$

The two orthogonal quadratures $\hat{X}_j(t)$, $\hat{Y}_j(t)$ obey the commutation relations $[\hat{X}_j(t), \hat{Y}_k(t')] = 2i\delta_{j,k}\delta(t,t')$, $j,k = i,s$.

The general idea for the detection of a field quadrature is to mix the signal field with a strong coherent field, called "'local oscillator"' field. The most used method is the *bal-*

anced homodyne detection, described e.g. in [48]. By changing ϕ, which can be done by changing the phase of the local oscillator, an arbitrary quadrature of the signal field can be measured. Notice that in Eq. (5.1) $\hat{Y}(\phi) = \hat{X}(\phi + \frac{\pi}{2})$ so that the $Y-$quadrature is simply the $X-$quadrature rotated by an angle $\pi/2$. Thus, without loss of generality, we limit our analysis to the $X-$quadratures. Definition (5.1) depends implicitly on the choice of the phases ϕ_s, ϕ_i, but for brevity of notation we will omit to write explicitely the dependence on ϕ_j in the following.
For convenience of calculation we introduce the Fourier transform of the quadrature operators:

$$\hat{X}_j(\Omega) = \int \frac{dt}{\sqrt{2\pi}} e^{i\Omega t} \hat{X}_j(t) \tag{5.2}$$

$$= \hat{A}_j^{\text{out}}(\Omega) e^{-i\phi_j} + \hat{A}_j^{\text{out}\dagger}(-\Omega) e^{+i\phi_j}. \tag{5.3}$$

Notice that this relation define not hermitian operators (unless $\Omega = 0$), which are hence not observables.

The amount of quadrature noise in the spectral domain can be characterized as usual by the so-called *fluctuations spectrum*

$$\Sigma_j(\Omega) = \int_{-\infty}^{\infty} d\tau\, e^{i\Omega\tau} \langle \hat{X}_j(t) \hat{X}_j(t+\tau) \rangle, \quad j = s, i \tag{5.4}$$

i.e. by the Fourier transform of the temporal correlation of quadrature operators. This definition is appropriate for a stationary system, for which the two-time temporal correlation depends only on the difference of times. Using the definition (5.2), it is useful to write those spectra in terms of the signal and idler spectral correlation functions $\langle X_j(\Omega) X_j(\Omega') \rangle$:

$$\Sigma_j(t) = \int d\Omega' e^{-i(\Omega+\Omega')t} \langle X_j(\Omega') X_j(\Omega) \rangle, \quad j = s, i. \tag{5.5}$$

By using the input-output relations (4.20) and the fact that the input operators are in the vacuum state, we obtain the following expression for the signal and idler field self-correlation in the spectral domain:

$$\langle \hat{X}_s(\Omega) \hat{X}_s(\Omega') \rangle = \delta(\Omega + \Omega') \left[1 + |V_s(\Omega)|^2 + |V_s(-\Omega)|^2 \right], \tag{5.6}$$

$$\langle \hat{X}_i(\Omega) \hat{X}_i(\Omega') \rangle = \delta(\Omega + \Omega') \left[1 + |V_i(\Omega)|^2 + |V_i(-\Omega)|^2 \right]. \tag{5.7}$$

Similarly, the signal-idler cross-correlation is given by

$$\langle \hat{X}_s(\Omega)\hat{X}_i(\Omega')\rangle = \delta(\Omega+\Omega')\left[U_s(\Omega)V_i(-\Omega)e^{-i(\phi_s+\phi_i)} + U_s^*(-\Omega)V_i^*(\Omega)e^{i(\phi_s+\phi_i)}\right]. \quad (5.8)$$

Substituting expressions (5.6)-(5.7) into Eq.(5.5) we obtain for the signal and idler spectra

$$\Sigma_s(\Omega) = \Sigma_i(\Omega) = 1 + |V_s(\Omega)|^2 + |V_i(\Omega)|^2. \quad (5.9)$$

where we used the identities $|V_s(-\Omega)|^2 = |V_i(\Omega)|^2$ and $|U_s(-\Omega)|^2 = |U_i(\Omega)|^2$, which can be inferred from unitarity conditions (4.25).

The first "1" term in Eq. (5.9) corresponds to the shot noise level. We see that the signal and idler quadratures taken individually do not depends on the choice of ϕ_s and ϕ_i and display no squeezing at any gain. In the stimulated PDC regime we are considering (with $|V_j|^2$ taking large values close to threshold), the quadrature noise for each beam is well above the shot noise and the marginal statistics of each beam is thermal like.

To observe EPR correlation, we must consider instead appropriate combinations of the signal and idler modes. With this purpose, we consider the sum and the difference between frequency conjugate components of the twin beams:

$$\hat{c}_\pm(t) = \frac{\hat{A}_s(t)e^{-i\phi_s} \pm \hat{A}_i(t+\Delta t)e^{-i\phi_i}}{\sqrt{2}}, \quad (5.10)$$

so that the Bogoliubov transformation (4.17) decouples into two independent squeeze transformations, implying that the $\pm$ modes are thus individually squeezed, and their squeezing ellipses [49] are oriented along orthogonal directions. This implies the simultaneous presence of correlation and anticorrelation in two orthogonal quadrature operators of the twin beams. We define the corresponding X-quadrature

$$\hat{X}_\pm = \frac{\hat{c}_\pm(t) + \hat{c}_\pm(t-\Delta t)}{\sqrt{2}} = \frac{\hat{X}_s(t) \pm \hat{X}_i(t-\Delta t)}{\sqrt{2}}, \quad (5.11)$$

where, in order to be as general as possible, we introduced a possible offset Δt between the times at which the two quadratures are measured.

As it will become clear in the following, this offset may be useful to optimize the amount of EPR correlation. In the frequency domain we have:

$$\hat{X}_{\pm}(\Omega) = \int \frac{d\Omega}{\sqrt{2\pi}} e^{i\Omega t} \frac{\hat{X}_s(t) \pm \hat{X}_i(t-\Delta t)}{\sqrt{2}} \tag{5.12}$$

$$= \frac{\hat{X}_s(\Omega) \pm e^{i\Omega\Delta t}\hat{X}_i(\Omega)}{\sqrt{2}}. \tag{5.13}$$

The spectral correlation of $\hat{X}_{\pm}(\Omega)$ can be expressed as a linear combination of correlation functions of the signal and idler quadratures:

$$\langle \hat{X}_{\pm}(\Omega)\hat{X}_{\pm}(\Omega')\rangle = \frac{1}{2}\Big\{ \langle \hat{X}_s(\Omega)\hat{X}_s(\Omega')\rangle + e^{i(\Omega+\Omega')\Delta t}\langle \hat{X}_i(\Omega)\hat{X}_i(\Omega')\rangle \\ \pm e^{i\Omega\Delta t}\langle \hat{X}_i(\Omega)\hat{X}_s(\Omega')\rangle \pm e^{i\Omega'\Delta t}\langle \hat{X}_s(\Omega)\hat{X}_i(\Omega')\rangle \Big\} \tag{5.14}$$

Subtituting the results (5.6)-(5.8) we obtain after some long but straightforward calculations

$$\langle \hat{X}_{\pm}(\Omega)\hat{X}_{\pm}(\Omega')\rangle = \frac{\delta(\Omega+\Omega')}{2}\Big[|U_s(\Omega) \pm V_i^*(-\Omega)e^{i\Omega\Delta t}e^{i(\phi_s+\phi_i)}|^2 \\ + |U_s(-\Omega) \pm V_i^*(\Omega)e^{-i\Omega\Delta t}e^{i(\phi_s+\phi_i)}|^2 \Big]. \tag{5.15}$$

The corresponding squeezing spectra, defined as

$$\Sigma_{\pm}(\Omega) = \int_{-\infty}^{+\infty} d\tau e^{i\Omega\tau}\langle \hat{X}_{\pm}(t)\hat{X}_{\pm}(t+\tau)\rangle \tag{5.16}$$

$$= \int_{-\infty}^{+\infty} d\Omega' e^{-i(\Omega+\Omega')t}\langle \hat{X}_{\pm}(\Omega)\hat{X}_{\pm}(\Omega')\rangle, \tag{5.17}$$

describe the degree of correlation ("-" sign) and anticorrelation ("+" sign) between the field quadratures of the twin beams at the crystal output faces. According to our definitions, the correlation / anticorrelation of the quadrature fluctuations are below the standard quantum limit when $\Sigma_{\pm}(\Omega)$ is below unity, the value "1" representing the shot-noise level characterizing two uncorrelated beams. If we consider the case of frequency degeneracy (by choosing the poling period Λ such that the PDC emission takes place at the degenerate frequency $\omega_s = \omega_i = \omega_p/2$), we notice that the generation of squeezed light is not as straightforward as in a standard degenerate OPO where a single degenerate squeezed mode exits the cavity from one of the cavity mirrors [47]. We expect however that that the two counter-propagating beams can be in principle be recombined through a beam 50:50 in order to produce two independently squeezed beams.

Substituting (5.15) into (5.17) we obtain the following analytical expressions

$$\Sigma_{\pm}(\Omega) = \frac{1}{2}[\sigma_{\pm}(\Omega) + \sigma_{\pm}(-\Omega)], \tag{5.18}$$

where

$$\sigma_{\pm}(\Omega) = |U_s(\Omega) \pm V_i^*(-\Omega)e^{i\Omega\Delta t}e^{i(\phi_s+\phi_i)}|^2 \tag{5.19}$$

$$= |U_s(\Omega)|^2 + |V_i(-\Omega)|^2 \pm 2|U_s(\Omega)V_i(-\Omega)|\cos[2\theta(\Omega) - \Omega\Delta t - \phi_s - \phi_i], \tag{5.20}$$

and the *angle of squeezing* θ is defined by the relation:

$$2\theta(\Omega) = \arg[U_s(\Omega)V_i(-\Omega)]. \tag{5.21}$$

As expected for the EPR state, the degree of correlation and anticorrelation in orthogonal quadratures are identical: $\Sigma_-(\Omega) \to \Sigma_+(\Omega)$, provided that $\phi_s \to \phi_s + \pi/2$ and $\phi_i \to \phi_i + \pi/2$ (more correctly, one actually needs to displace the sum of the phases by π: $\phi_s + \phi_i \to \phi_s + \phi_i + \pi$). The maximum amount of squeezing is obtained by appropriately selecting the local oscillator phases ϕ_s and ϕ_i. Because of the lack of symmetry $\Omega \to -\Omega$ it is impossible to optimize the phase for noise reduction in both terms $\sigma_{\pm}(\Omega)$ and $\sigma_{\pm}(-\Omega)$ except for $\Omega = 0$. It turns out, however, to be possible to optimize the phase for counterpropagating PDC, provided that Δt is properly chosen, at least as long as the linear approximation for phase matching holds. For example, for the difference mode S_-, the optimal choice would be

$$\phi_s + \phi_i = \begin{cases} 2\theta(\Omega) - \Omega\Delta t & \text{for } \sigma_-(\Omega) \\ 2\theta(-\Omega) + \Omega\Delta t & \text{for } \sigma_-(-\Omega). \end{cases} \tag{5.22}$$

[for the sum mode $\sigma_+(\Omega)$ the relation is identical, if we consider a displacement of the sum of the phases by π]. We notice that the presence of the offset in (5.22) is useful, because if we explicit the form of the coefficients U_s and V_i [see Eqs. (4.24)] we have:

$$\phi_s + \phi_i = 2\theta(\Omega) - \Omega\Delta t = \arg[U_s(\Omega)V_i(-\Omega)] - \Omega\Delta t \tag{5.23}$$

$$= k_s l_c + \phi_p + \beta(\Omega) - \Omega\Delta t + \arg[\mathrm{Sinc}\gamma(\Omega)] \tag{5.24}$$

$$\approx k_s l_c + \phi_p + \Omega(\Delta t_A - \Delta t) + \arg[\mathrm{Sinc}\gamma(\Omega)], \tag{5.25}$$

where we used the linear approximation for the phase β (4.51). We can thus compensate the linear component of the phase (5.25) for both $\sigma_-(\Omega)$ and $\sigma_-(-\Omega)$ simultaneously by

considering a temporal delay [see Eq. (4.52)]

$$\Delta t = \Delta t_A \equiv \frac{l_c}{2v_{gs}} - \frac{l_c}{2v_{gi}}. \tag{5.26}$$

Fig. 5.1a shows the best attainable degree of correlation $\Sigma_{\pm}(\Omega)$ between field quadratures of the twin beams, as a function of the frequency. The quadrature angles are chosen as in (5.25), setting a temporal delay as in (5.26). We see that $\Sigma_{\pm}$ is minimized at any frequency, and the noise never goes above the shot noise level "1". We can notice that the last term in (5.25) is either equal to 0 or to π depending on the sign of $\mathrm{Sinc}\gamma(\Omega)$. In particular

$$\arg[\mathrm{Sinc}\gamma(\Omega)] = 0 \ \text{ if } \ |\Omega| \lesssim \sqrt{\pi^2 - g^2}\Omega_{gvs} \sim 2.72\Omega_{gvs}, \ \text{ for } g \to \frac{\pi}{2}, \tag{5.27}$$

[this can be easily inferred using approximation (4.49) for the phase-matching function in order to evaluate the first node of $\mathrm{Sinc}\gamma(\Omega)$], while the MOPO characteristic emission bandwidth becomes much smaller than Ω_{gvs} when approaching treshold (see Chap. 4, Fig. 4.4a).

The maximum amount of squeezing within a bandwidth on the order of Ω_{gvs} can thus be written as

$$\phi_s + \phi_i = \begin{cases} k_s l_c + \phi_p & \text{for } \Sigma_- \\ k_s l_c + \phi_p + \pi & \text{for } \Sigma_+ \end{cases} \tag{5.28}$$

[the anti-squeezing spectra are obtained again by considering the orthogonal quadratures (with $\phi_j \to \phi_j + \pi/2$)].

Figures 5.1b and 5.2 show the squeezing spectra $\Sigma^S_{\pm}(\Omega)$ and anti-squeezing spectra $\Sigma^A_{\pm}(\Omega)$ respectively, when the phases are fixed as $\phi_s + \phi_i = k_s l_c + \phi_p$. In these numerical examples we consider a 1 *cm* LiNbO3 crystal ($\Omega_{gvs} = 1,3 \cdot 10^{10}\ s^{-1}$, $\Omega_{gvm} = 7,23 \cdot 10^{11}\ s^{-1}$), pumped at $\lambda_p = 800$ *nm* and with a poling period $\Lambda = 354.7$ *nm* leading to emission at the degenerate wavelength $\lambda_s = \lambda_i = 1600$ *nm*. We see from Fig 5.1 that we have a large amount of squeezing within a bandwidth on the order of $\Delta\Omega_{squeeze} = \sqrt{\pi^2 - g^2}\Omega_{gvs} \sim 2.72\Omega_{gvs}$ corresponding to the first node of $\mathrm{Sinc}\gamma(\Omega)$. We verified that even without the optimization of the temporal delay (5.26). i.e. taking $\Delta t = 0$, the amount of squeezing remains almost unchanged. This can be understood by noticing that the linear term $\Delta t_A \Omega$ in (5.25) becomes relevant only at frequencies on the order of $\Delta\Omega_{squeeze}$.

In contrast, the spectrum of the antisqueezed shown in Fig. 5.2 is characterized by the much narrower bandwidth $\sim \varepsilon\Omega_{gvs}$ which goes to zero for $\varepsilon = \pi/2 - g \to 0$, a feature reflecting the narrowing of the MOPO spectrum and the critical slowing down of temporal fluctuations occurring close to threshold.

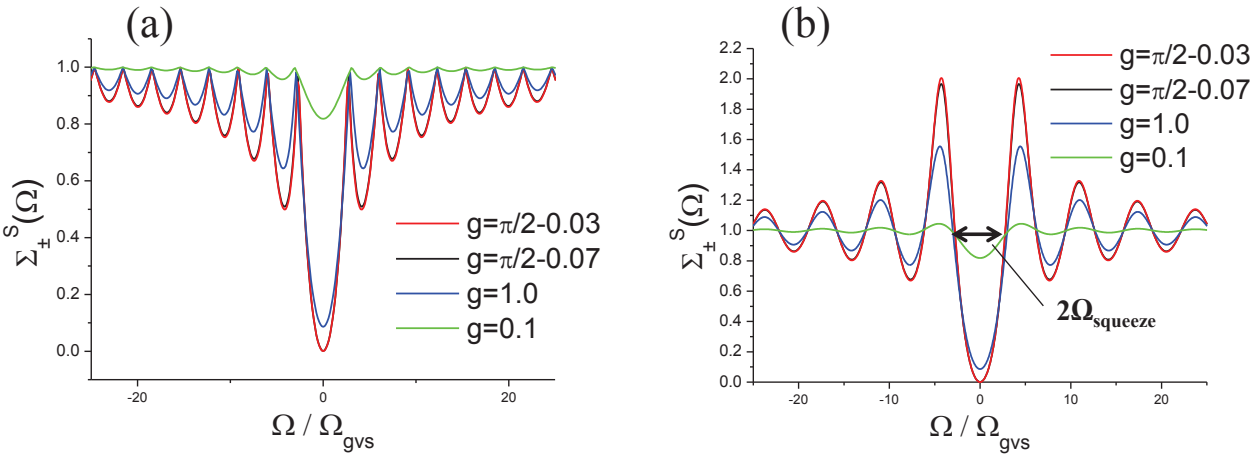

Fig. 5.1 Squeezing spectrum $\Sigma^S_{\pm}(\Omega)$ in the sum or difference modes for different values of the parametric gain g as a function of Ω/Ω_{gvs}. In (a) the quadrature angles are optimized for best squeezing (5.25), while in (b) they are fixed as $\phi_s + \phi_i = k_s l_c + \phi_p$. A large amount of squeezing is obtained for $g \to \pi/2$ with a squeezing bandwidth on the order of Ω_{gvs}.

It is also interesting to evaluate the amount of squeezing and anti-squeezing at $\Omega = 0$, $\Sigma^S_{\pm}(0)$ and $\Sigma^A_{\pm}(0)$, which provide the X-quadrature fluctuations noise of the c_+ and c_- modes (5.10) in the limit of long measurement times. Close to threshold, for $\varepsilon \equiv \pi/2 - g \ll 1$, it can be easily verified from definitions (4.21)-(4.24) that $|U_s(0)| \approx |V_i(0)| \approx 1/\varepsilon \gg 1$ and we have thus for the squeezed quadrature case

$$\Sigma^S_{\pm}(0) = [|U_s(0)| - |V_i(0)|]^2 = \frac{1}{[|U_s(0)| + |V_i(0)|]^2} \approx \frac{\varepsilon^2}{4} \tag{5.29}$$

while for the orthogonal anti-squeezed quadratures

$$\Sigma^A_{\pm}(0) = [|U_s(0)| + |V_i(0)|]^2 \approx \frac{4}{\varepsilon^2}, \tag{5.30}$$

where we used the unitarity condition (4.25).

Figure 5.3 shows the plots of $\Sigma_{\pm}(0)$, for the squeezed and anti-squeezed case, as a function of g evaluated from the exact formula (5.20) (blue line) and from approximation (5.29) - (5.30) holding for small ε (dashed red line). From figure 5.3 we see that perfect squeezing is reached at threshold but also for gains $g \approx 1$ the level of squeezing is reasonably good. Such a behavior of the squeezing spectra close to threshold is very similar to that found in standard optical parametric oscillators enclosed in a resonant cavity.

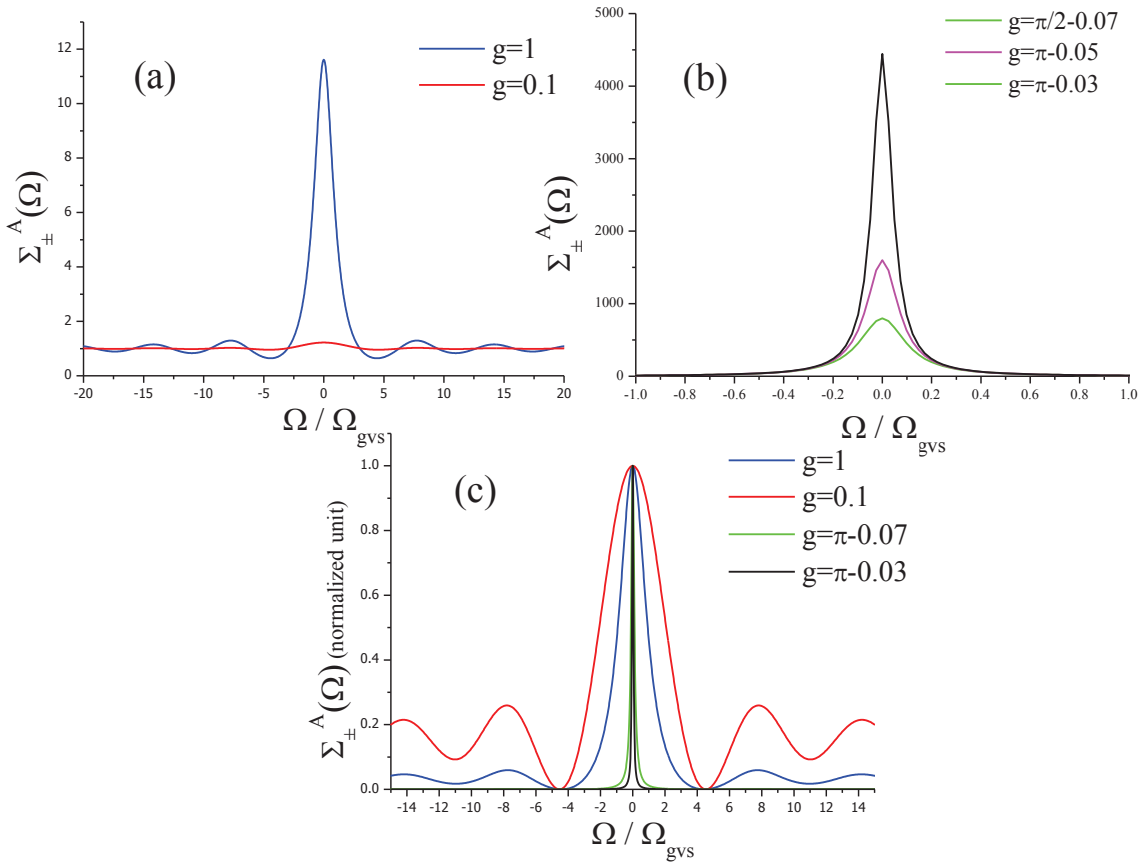

Fig. 5.2 Anti-squeezing spectrum $\Sigma_{\pm}^{A}(\Omega)$ in the sum or difference modes for different values of the parametric gain g as a function of Ω/Ω_{gvs}. Its width $\sim \varepsilon\Omega_{gvs}$ shrinks to zero when approaching threshold. This is evident in (c) where spectra have been normalized to their peak values.

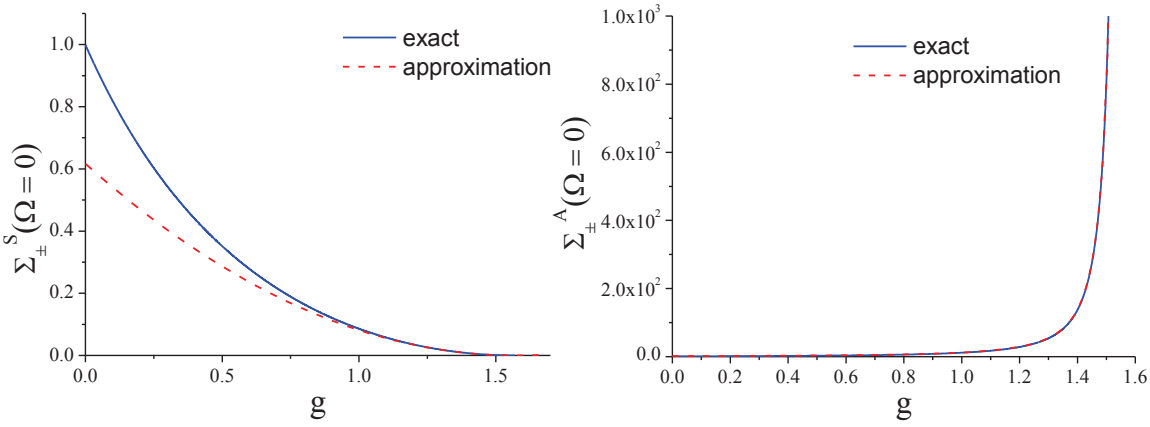

Fig. 5.3 Squeezing spectrum $\Sigma_{\pm}^{S}$ and anti-squeezing spectrum $\Sigma_{\pm}^{A}$ for $\Omega = 0$ as functions of g, compared with their approximations (red dashed lines), given by (5.29) and (5.30).

Notice that under optimal condition [i.e. when (5.25) holds], the relation between squeezing and antisqueezing strectra (5.29) holds $\forall\Omega$

$$\Sigma^S_{\pm}(\Omega) = [|U_s(\Omega)| - |V_i(\Omega)|]^2 = \frac{1}{[|U_s(\Omega)| + |V_i(\Omega)|]^2} = \frac{1}{\Sigma^A_{\pm}(\Omega)}. \tag{5.31}$$

For the sake of completeness we give here the explicit expressions for the squeezing spectra, which can be obtained using the definitions of the coefficients (4.24):

$$\Sigma^S_{\pm}(\Omega) = |\phi(\Omega)|^2 [1 - g\mathrm{Sinc}\gamma(\Omega)]^2 \tag{5.32}$$

$$= \frac{\gamma(\Omega) - g\sin\gamma(\Omega)}{\gamma(\Omega) + g\sin\gamma(\Omega)}. \tag{5.33}$$

Chapter 6

Spatio-temporal aspects

In previous chapters we mainly investigated the temporal properties of counterpropagating PDC, neglecting the spatial degrees of freedom. In fact we considered only collinear propagation, either assuming that light was collected at small propagation angles with respect to the pump, or because of a waveguiding configuration. The PDC entangled state in the standard copropagating geometry has been mostly investigated either in a purely temporal [3–5] or spatial [50, 42, 51, 44] framework. However, when considering large bandwidth both in the spatial and in the temporal domains, it is essential to consider a full three-dimensional model [52, 6, 53, 28, 39] because of the mutual dependence of the spatial and the temporal degree of freedom. In particular, as shown in [6] and demonstrated experimentally in [54], the structure of the PDC entangled state is characterized by an X-shaped structure, non-separable in space and time, that appears as a consequence of the phase matching-mechanism governing the wave-mixing process. This peculiar X geometry is intrinsic to PDC at the microscopic quantum level of photon-pair entanglement [55]. The full spatio-temporal description highlights how it is possible to tailor the biphotons properties in a novel non-separable way: temporal properties can be modified acting on the spatial degrees of freedom and vice versa. From these considerations it seems necessary to consider a full spatio-temporal model also for the description of the PDC process in a counterpropagating geometry. We will show in this chapter, however, that spatial and temporal degrees of freedom of the PDC state produced in a counterpropagating geometry are almost uncorrelated, justifying the choice of limiting our analysis only to the temporal domain.

In order to study the spatial properties of the PDC state we start from the propagation equations (1.47) written in the spatio-temporal domain, and we limit ourselves to the simple case of a monochromatic plane wave pump of frequency ω_p. As in Chapter 4 the pump field can be treated as a known classical field and the corresponding spectral field operator $\hat{a}_p(z, \boldsymbol{q}, \Omega)$ defined by Eq.(1.39) can be substituted with the z-independent c-number function

$\alpha_p(\Omega,\boldsymbol{q},z=0)=\alpha_p\sqrt{2\pi}\delta(\boldsymbol{q})\delta(\Omega)$. In this limit, the propagation equations for the signal and the idler fields take the following form, generalizing Eqs. (4.6) to the full spatio-temporal domain:

$$\frac{\partial}{\partial z}\hat{a}_s(\boldsymbol{q},\Omega,z)=+\frac{g}{l_c}\hat{a}_i^\dagger(-\boldsymbol{q},-\Omega,z)e^{-i\bar{D}(\boldsymbol{q},\Omega)z}e^{i\phi_p}, \tag{6.1a}$$

$$\frac{\partial}{\partial z}\hat{a}_i^\dagger(-\boldsymbol{q},-\Omega,z)=-\frac{g}{l_c}\hat{a}_s(\boldsymbol{q},\Omega,z)e^{i\bar{D}(\boldsymbol{q},\Omega)z}e^{-i\phi_p}, \tag{6.1b}$$

where

$$\bar{D}(\boldsymbol{q},\Omega):=D(\boldsymbol{q},\Omega,-\boldsymbol{q},-\Omega)=k_{sz}(\boldsymbol{q},\Omega)-k_{iz}(-\boldsymbol{q},-\Omega)-k_{pz}+k_G. \tag{6.2}$$

is the phase-mismatch of the conjugate signal-idler mode pair $(\boldsymbol{q},\Omega)$ and $(-\boldsymbol{q},-\Omega)$ in the cw plane-wave pump limit [see definition (1.36)]. We limit our investigation to the low gain regime $g=\sqrt{2\pi}\bar{\sigma}|\alpha_p|l_c\ll 1$, and solve Eqs. (6.1) within a first-order perturbative approximation [see introduction of Chap.III, Eqs. (3.8-3.10) for more details]. In the CW plane-wave pump limit, the solution can be written in the form of input-output relations:

$$\hat{a}_s^{out}(\boldsymbol{q},\Omega)=\hat{a}_s^{in}(\boldsymbol{q},\Omega)+\Psi(\boldsymbol{q},\Omega,-\boldsymbol{q},-\Omega)\hat{a}_i^{\dagger in}(-\boldsymbol{q},-\Omega), \tag{6.3a}$$

$$\hat{a}_i^{out}(\boldsymbol{q},\Omega)=\hat{a}_i^{in}(\boldsymbol{q},\Omega)+\Psi(\boldsymbol{q},\Omega,-\boldsymbol{q},-\Omega)\hat{a}_s^{\dagger in}(-\boldsymbol{q},-\Omega), \tag{6.3b}$$

where we introduced the *biphoton amplitude* defined as:

$$\Psi(\boldsymbol{q},\Omega,-\boldsymbol{q},-\Omega)=ge^{-i\bar{D}(\boldsymbol{q},\Omega)\frac{l_c}{2}}\mathrm{Sinc}\left[\bar{D}(\boldsymbol{q},\Omega)\frac{l_c}{2}\right]. \tag{6.4}$$

The spatio-temporal emission spectra $\langle\hat{I}_j(\Omega)\rangle=\langle\hat{A}_j^\dagger(\Omega)\hat{A}_j(\Omega)\rangle$, $(j=i,s)$, are given by

$$\langle\hat{I}_s(\boldsymbol{q},\Omega)\rangle=\langle\hat{I}_i(\boldsymbol{q},\Omega)\rangle=g^2\mathrm{Sinc}^2\left[\bar{D}(\boldsymbol{q},\Omega)\frac{l_c}{2}\right]. \tag{6.5}$$

We wish to compare the behaviour of those quantities in the counter-propagating and the co-propagating configurations. Considering the same conditions of purely spontaneous PDC emission and cw plane-wave pump, the biphoton amplitude and the field spectra have the same form (6.4) and (6.5) in both configurations. However, for the co-propagating case, the phase-mismatch function (6.2) must be replaced with (see discussion in Sec.1.1)

$$\bar{D}'(\Omega)=k_{sz}(\boldsymbol{q},\Omega)+k_{iz}(-\boldsymbol{q},-\Omega)-k_{pz}+k_G, \tag{6.6}$$

The different sign in front of the idler k-vector leads to a completely different behaviour of $\psi(\boldsymbol{q},\Omega)$ and $\langle \hat{I}_j(\boldsymbol{q},\Omega)\rangle$ in the spatio-temporal frequency space.

Figure 6.1 compares the spatio-temporal emission spectra in the co-propagating and in the counterpropagating geometries, evaluated respectively for type I BBO crystal and a type 0 KTP crystal both tuned for collinear emission at degeneracy. A first difference between the

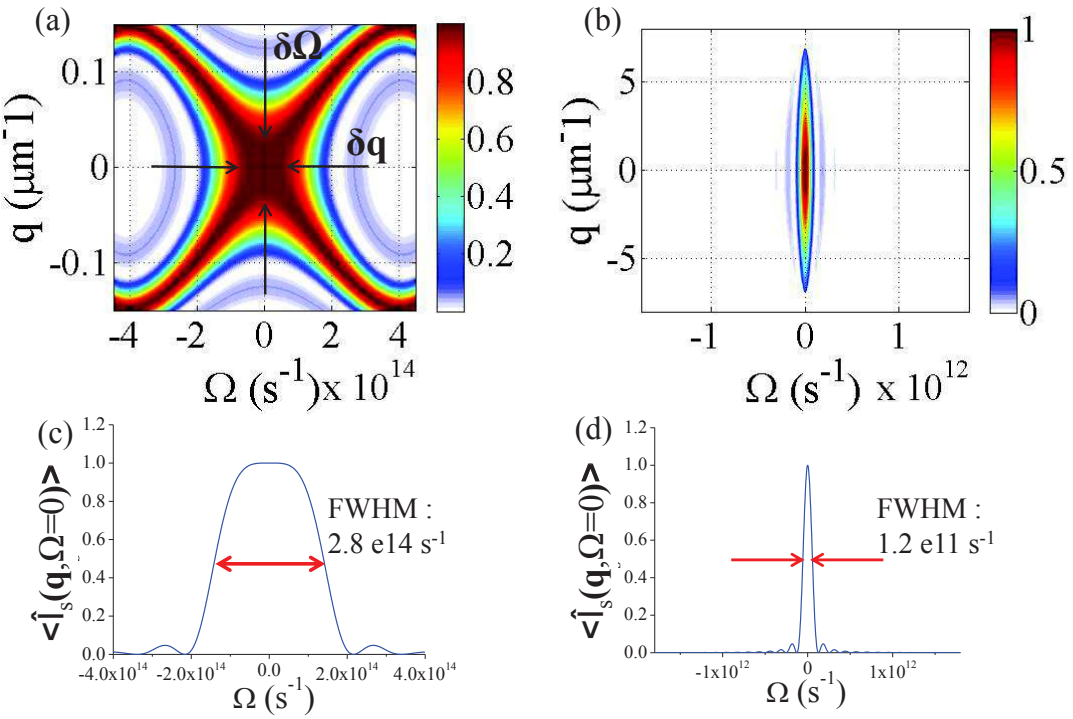

Fig. 6.1 Plot of the emission spectrum (6.5) in the $(\boldsymbol{q},\Omega)$ plane normalized by its peak value, respectively in (a) the copropagating configuration for a 4mm type I BBO crystal with collinear phase-matching at degeneracy and in (b) the counter-propagating configuration for a periodically poled 4mm KTP crystal, pumped at 821.4nm. In (c) and (d) are shown the section of the spectra for $\boldsymbol{q}=0$ and their FWHM. In order to achieve phase matching at the degenerate frequency the poling period $\Lambda_{\rm pol}$ has to be of order of $\approx 6.6\mu$m in the copropagating configuration, while in the counterpropagating configuration $\Lambda_{\rm pol}\approx 0.2\mu$m.

co-propagating configuration and the counter-propagating configuration is the shape of the spatio-temporal emission spectrum: in the co-propagating case [see Fig. 6.1(a)] the spectrum exhibits a characteristic non-factorable X-shaped geometry [6], which expresses a strong coupling between the spatial and the temporal degrees of freedom. More insight can be gained by performing a quadratic expansion of the phase-mismatch functions [(6.2,6.6)] close

to the phase-matched frequencies (at $\boldsymbol{q} = 0$, $\Omega = 0$) within the paraxial approximation. We thus adopt this approximation for the longitudinal component of the wave-vector $k_{jz}(\boldsymbol{q}, \Omega) = \sqrt{k_j^2(\Omega) - q^2}$:

$$k_{jz}(\boldsymbol{q}, \Omega) \approx k_j(\Omega) - \frac{q^2}{2k_j} \tag{6.7}$$

$$\approx k_j + k_j'\Omega + \frac{1}{2}k_j''\Omega^2 - \frac{q^2}{2k_j}. \tag{6.8}$$

where $k_j = k_j(0)$ and $k_j'' = d^2k_j/d\Omega^2|_0$. Substituing this approximated expression in the phase-matching relation (6.2) for the co-propagating configuration at degeneracy (type I), we obtain following phase-mismatch function (notice that by assumption $2k_s - k_p = 0$ at frequency $\omega_p/2$):

$$\bar{D}'(\Omega) = \frac{q^2}{k_s} + k_s''\Omega^2 + O(q^4, \Omega^4). \tag{6.9}$$

which does not contain linear terms. From Eq. (6.9) we see that close to degeneracy the phase-matched modes satisfy the linear relation

$$q \approx \pm\sqrt{\frac{k_j}{k_j''}}\Omega \tag{6.10}$$

within a very broad spatial and temporal bandwidth of the order of $\delta q_0 = \sqrt{k_s/l_c}$, $\delta\Omega = \sqrt{1/k_s''l_c}$, respectively (see arrows in figure 6.1a).

On the contrary, in the counter-propagating case [see Fig. 6.1(b)] the X-shaped geometry of the standard co-propagating configuration is replaced by a very narrow vertical cigar-like spectrum that extends to much higher transverse vectors (corresponding to angles up to ninety degree, see also Fig. 6.3b). In this case the expansion of the phase mismatch function also includes linear terms and is given by the expression (taking into account that $k_s - k_i - k_p + k_G = 0$ at $\Omega = 0$):

$$\bar{D}(\boldsymbol{q}, \Omega) = (k_s' + k_i')\Omega + \frac{1}{2}(k_s'' - k_i'')\Omega^2 - \frac{1}{2}\left(\frac{1}{k_s} - \frac{1}{k_i}\right)q^2 + O(q^3, \Omega^3). \tag{6.11}$$

In the degenerate case where perfect phase-matching takes place at frequency $\omega_p/2$ (corresponding to $\Omega = 0$), the type 0 configuration implies that $k_s = k_i$, $'k_s = k_i'$ etc., and the dependence on q disappears at all orders. In this particular case phase-matching is therefore satisfied for all emission angles at the same frequency $\omega_p/2$ and there is no coupling

between the spatial and temporal degrees of freedom: the angular dispersion characterizing the emission of most PDC sources is here completely absent.

The situation changes under non degenerate phase-matching conditions in which phase-matching along the collinear direction occurs at a frequency different from $\omega_p/2$. In this case the phase-matching curves of the signal and idler field in the (Ω, q)-plane are well approximated by the parabola

$$q = \pm\sqrt{\frac{2(k_s' + k_i')}{\frac{1}{k_s} - \frac{1}{k_i}}\Omega}. \tag{6.12}$$

obtained by neglecting the Ω^2 term describing second-order dispersion in Eq.(6.11). We see from this expression that close to degeneracy (for $k_s' \approx k_i'$) the spatial and the temporal degree of freedom are only weekly coupled (i.e. angular dispersion occurs only at large angles). The phase-matching in the counter-propagating geometry determines a very narrow frequency bandwidth in the temporal domain (FWHM$= 1.2 \cdot 10^{11}$ Hz), about 3 order of magnitude narrower than that of the copropagating case (FWHM $= 2.8 \cdot 10^{14}$ for $\boldsymbol{q} = 0$). In contrast, there is no restriction on the propagation direction.

In order to visualize the kind of angular spectrum which can be measured experimentally with an imaging spectrometer, we map the spectral intensity (6.5) in the (λ, α)-plane, α being the emission angle with respect to the pump reference frame defined by the relation $\alpha = \arcsin[\boldsymbol{q}/k_s(\Omega)]$. The reference frame and the pump one are illustrated in Fig.(6.2). In

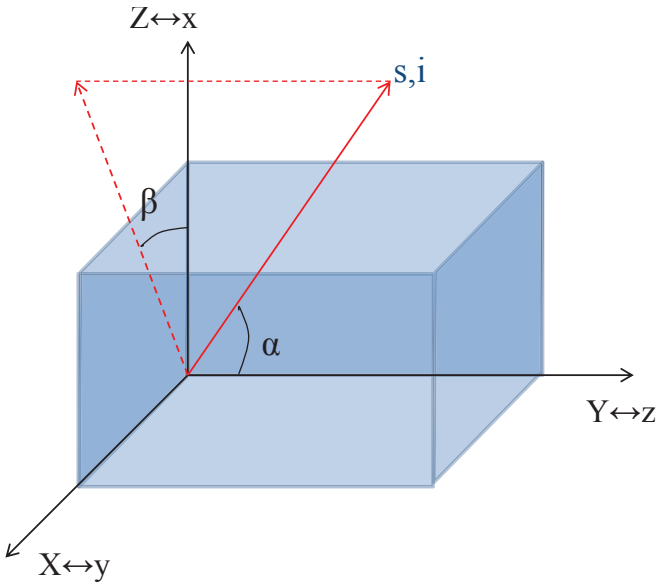

Fig. 6.2 Crystal reference frame and pump reference frame, respectively

Fig. 6.3 are represented the spatio-temporal emission spectra for the co-propagating and

for the counter-propagating geometry, respectively. We see that in the counter-propagating geometry signal and idler can be emitted at any angle up to $\alpha \approx 90^\circ$ [see Fig. 6.3(b)], while the angular emission is limited to angles smaller than $\approx 2^\circ$ in the standard configuration [see Fig. 6.3(a)].

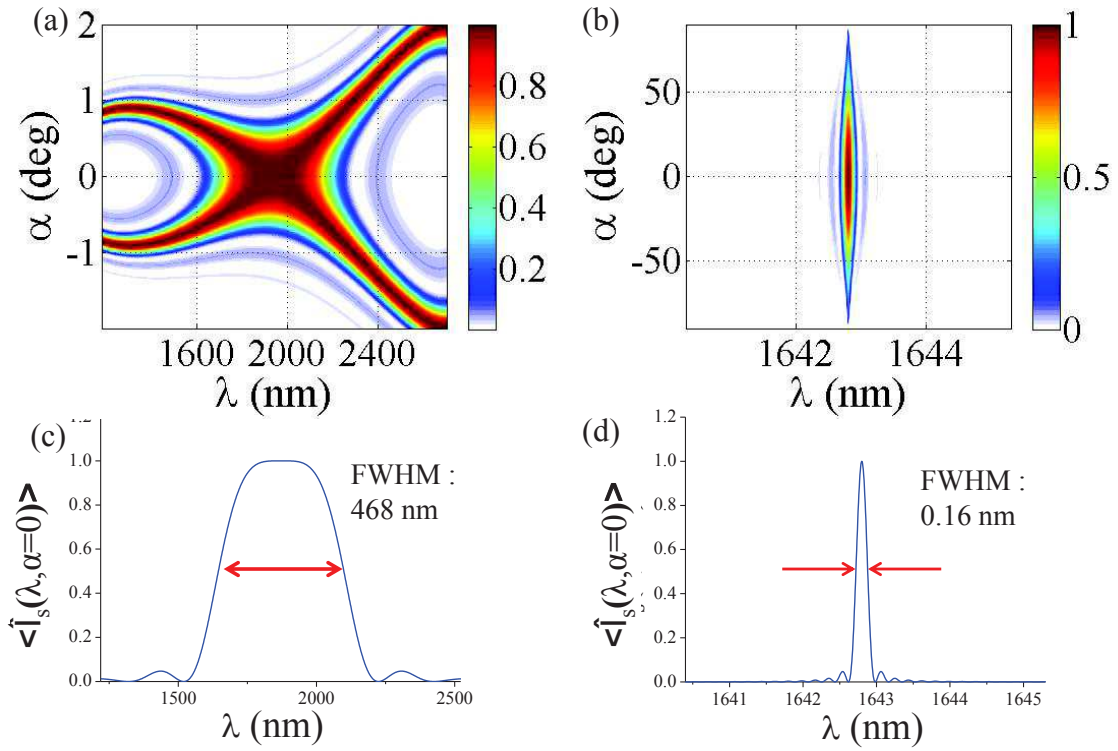

Fig. 6.3 Angular emission spectrum (normalized to its peak value) in the (λ, α) plane in the low gain regime ($g = 0.001$), respectively in (a) the co-propagating and in (b) the counter-propagating configuration (same configuration of Fig. 6.1). In (c) and (d) are shown the section of the spectra at $\alpha = 0.0^\circ$ and their FWHM. Here $\beta = 0.0^\circ$

In the non degenerate emission case the cigar-like spectrum exhibits a curvature that follows the prediction of formula (6.12). In Fig. 6.4 are represented the spatio-temporal emission spectra for the signal and idler fields in the non degenerate case considered in the experiment by Canalias *et al.* [1]. In this case the spatial and temporal degrees of freedom are correlated since the emission is characterized by a strong angular dispersion.

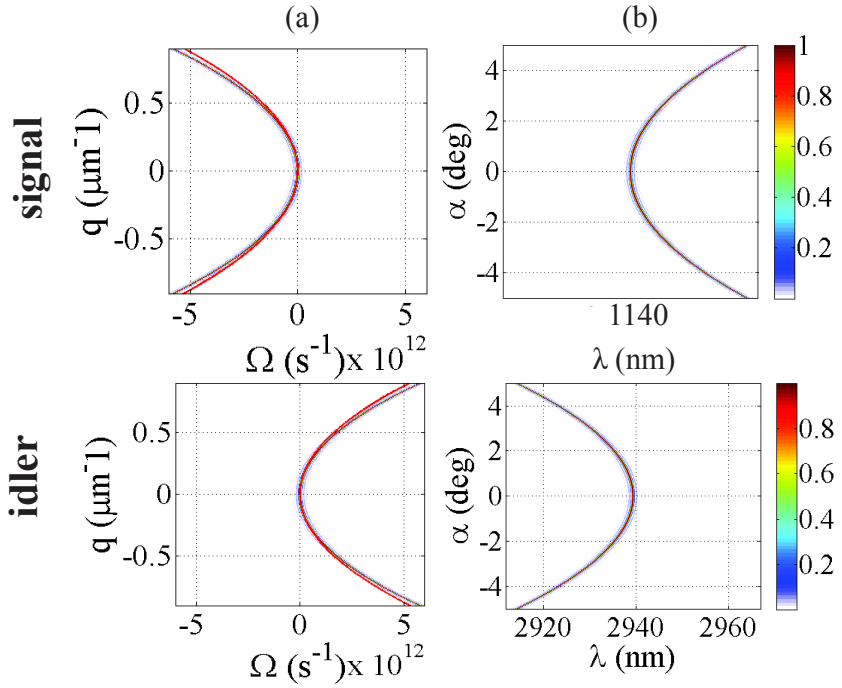

Fig. 6.4 Normalized signal emission spectrum at the output face of a KTP crystal, respectively in (a) the $(\boldsymbol{q}, \Omega)$ plane and in (b) the (λ, α) plane for for the non degenerate case. The red line represents the function defined in Eq. (6.12). Here the pump wavelength is 821.4 nm, the MOPO generated signal is at 1140 nm, and the idler at 2941 nm as in [1].

6.1 Evaluation of the effective nonlinear coupling costant

It is important to underline that since in the co-propagating geometry the angles involved are small, the variation of the nonlinear coupling constant with the propagation direction can be safely neglected. This is no more valid in the counterpropagating geometry, where the angles involved are very large.

In order to determine how the effective nonlinear coupling constant depends on the propagation direction, we use the following notation for the nonlinear susceptibility tensor (see Eq. 1.1):

$$d_{ijk} = \frac{1}{2}\chi^{(2)}_{ijk}, \tag{6.13}$$

where, the factor of $\frac{1}{2}$ is a consequence of historical convention. We now assume that d_{jkl} is symmetric in its last two indices. We then simplify the notation by introducing a contracted matrix d_{ji} (see [22]) according to the prescription:

kl :	11	22	33	23, 32	31, 13	12, 21	
i :	1	2	3	4	5	6	(6.14)

The nonlinear susceptibility tensor can then be represented as the 3×6 matrix

$$d_{ij} = \begin{pmatrix} d_{11} & d_{12} & d_{13} & d_{14} & d_{15} & d_{16} \\ d_{21} & d_{22} & d_{23} & d_{24} & d_{25} & d_{26} \\ d_{31} & d_{32} & d_{33} & d_{34} & d_{35} & d_{36} \end{pmatrix}. \tag{6.15}$$

As an example we can consider a KTP crystal for which the d_{ij} matrix is given by:

$$d_{ij} = \begin{pmatrix} 0 & 0 & 0 & 0 & d_{15} & 0 \\ 0 & 0 & 0 & d_{24} & 0 & 0 \\ d_{31} & d_{32} & d_{33} & 0 & 0 & 0 \end{pmatrix}, \tag{6.16}$$

with $d_{15} = 6.1 pm/V$, $d_{24} = 7.6 pm/V$, $d_{31} = 6.5 pm/V$, $d_{32} = 5.0 pm/V$, $d_{33} = 13.7 pm/V$.

We can describe the nonlinear polarization leading to difference-frequency generation in terms of d_{il} by the matrix equation (further details can be found in [26]):

$$\begin{pmatrix} P_x(\omega_m-\omega_n) \\ P_y(\omega_m-\omega_n) \\ P_z(\omega_m-\omega_n) \end{pmatrix} = 4\varepsilon_0 \begin{pmatrix} d_{11} & d_{12} & d_{13} & d_{14} & d_{15} & d_{16} \\ d_{21} & d_{22} & d_{23} & d_{24} & d_{25} & d_{26} \\ d_{31} & d_{32} & d_{33} & d_{34} & d_{35} & d_{36} \end{pmatrix} \begin{pmatrix} E_x(\omega_m)E_x^*(\omega_n) \\ E_y(\omega_m)E_y^*(\omega_n) \\ E_z(\omega_m)E_z^*(\omega_n) \\ E_y(\omega_m)E_z^*(\omega_n)+E_z(\omega_m)E_y^*(\omega_n) \\ E_x(\omega_m)E_z^*(\omega_n)+E_z(\omega_m)E_x^*(\omega_n) \\ E_x(\omega_m)E_y^*(\omega_n)+E_y(\omega_m)E_x^*(\omega_n) \end{pmatrix}, \tag{6.17}$$

where the extra factor of 2 comes from the summation over n and m. The equations for calculating the conversion efficiency use the *effective nonlinearity* d_{eff}, which comprises all the summation operations along the polarization directions of the interacting waves:

$$d_{\text{eff}} = \boldsymbol{P}_s d_{ij} \boldsymbol{P}_p \boldsymbol{P}_i = \boldsymbol{P}_i d_{ij} \boldsymbol{P}_p \boldsymbol{P}_s = \boldsymbol{P}_p d_{ij} \boldsymbol{P}_s \boldsymbol{P}_i, \tag{6.18}$$

where $\boldsymbol{P}_j$ is the polarization versor of the electric field (s,i,p) for a given propagation direction, determined by the angles α, β.

The quantity d_{eff} represents a scalar product of the first vector in (6.18) and a tensor product of the $d\boldsymbol{P}\boldsymbol{P}$ type, which is also a vector. The vector components P_i depends on the type of the interaction (oee,ooe,eee, and so on).

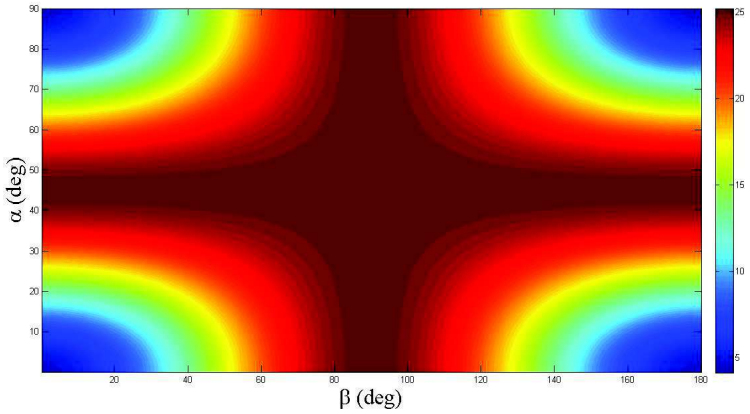

Fig. 6.5 Coefficient d_{eff} as a function of the emission angles α and β.

The dependence of the d_{eff} coefficient on the angles α and β is represented in Fig. 6.5, for a KTP crystal, *eee* configuration.

We see that for $\beta = 0°$ (walk-off plane) the angular emission is not equally favored for all the angles α, but it decreases at larger angles.

On the contrary, for $\beta = 90°$ (plane perpendicular to the walk-off), the angular emission does not depend on the emission angle α. This can be seen also in Fig. 6.6 which shows a comparison between emission spectra in the (α, λ) plane for $\beta = 90°$ and $\beta = 0°$, respectively. In the first column we see how there is no restriction on the emission angle α when we consider the plane perpendicular to the walk-off, while in the second column we see how the probability of emitting a pair of photons at large α decreases.

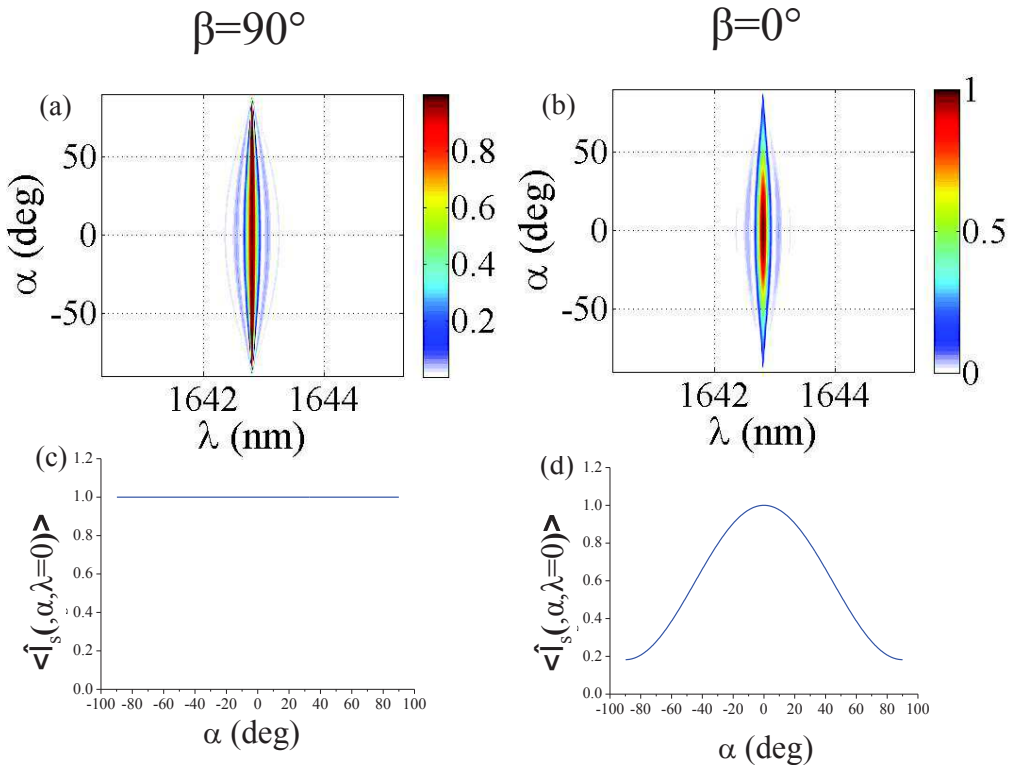

Fig. 6.6 Normalized signal emission spectrum at the output face of the crystal, respectively in (a) the walk-off plane ($\beta = 0.0°$) and in (b) the plane perpendicular to the walk-off ($\beta = 90.0°$) for a periodically poled KTP crystal of length 4mm, pumped at 821.4nm. In (c) and (d) are shown the section of the spectra for the central wavelength.

Conclusions

In this work we provided a theoretical analysis of the properties of counterpropagating twin beams generated by spontaneous parametric down-conversion occurring in periodically poled $\chi^{(2)}$ media. We first developed a general quantum model (Chap. I) that describes the multi-mode fields generated through parametric-down conversion in the counter-propagating configuration. We showed (Chap. II) that its classical counterpart can be reduced to the simple three-modes interaction model first introduced by Y.Ding and J. Khurgin [27] to describe PDC in the counter-propagating geometry. Through this elementary model we demonstrated the existence of a threshold above which coherent emission takes place through the combined effect of distributed feedback and stimulated PDC, showing that the source behaves as a mirrorless parametric oscillator.

In the framework of the quantum model developed in Chap. I we analyzed different operating conditions below the threshold for coherent emission. We first focused our attention on the purely spontaneous regime, well below the MOPO threshold, exploring the possibility to exploit the source for generating pure heralded single photons (Chapter III). We provided a detailed analysis of the conditions under which twin photons can be generated in a separable state through the quantitative evaluation of the Schmidt number. Our main result is that twin photons are emitted in a nearly separable state when the pump pulse duration τ_p lies within two very different characteristic time scales governing the system dynamics: the typical delay time associated to the group-velocity mismatch (GVM) between the signal and the pump photons $\tau_{gvm} = \frac{l_c}{2v_{gp}} - \frac{l_c}{2v_{gs}}$ (typically less than 1 picosecond), and the much longer GVS time scale $\tau_{gvs} = \frac{l_c}{2v_{gs}} + \frac{l_c}{2v_{gi}}$ giving the typical temporal separation of their arrival time on the crystal output faces (tens of picoseconds, comparable to the photon transit time across the crystal). Such a difference of time scales occurs naturally in the counterpropagating configuration, for basically any kind of material and tuning condition. Moreover, because of this same feature, counter-propagating twin photons in a pure state can in principle be heralded at any wavelength by choosing the appropriate poling period. This represents a major advantage with respect to more conventional co-propagating configurations where separability can be achieved only at special operational points through the technique of group-velocity matching

[5, 43]. The counter-propagating configuration offers thus much more flexibility, once the technical challenges for the fabrication of crystals with sub-micrometric poling periods are overcomed. As put in evidence from the evaluation of Schmidt number as a function of the pump pulse duration, entanglement is restored in the nearly monochromatic limit ($\tau_p \gg \tau_{gvs}$), where frequency correlations prevails because of energy conservation, as well as for ultra-short pulses ($\tau_p \ll \tau_{gvm}$), where correlations are determined by phase-matching. By inspecting the analytical form of the twin photons correlation function in the temporal domain we were able to provide a clear physical interpretation of those transitions between entangled and separable twin photon states. We also investigated the spectral properties of the emitted twin photons, which in general display much narrower bandwidths than in usual co-propagating geometries because of the peculiar phase-matching conditions. In particular we showed that for a long pump pulse twin photons have the same spectrum and the same coherence properties. Conversely, for an ultrashort pump pulse, the properties of the counterpropagating idler are entirely determined by the phase matching and reflect the momentum conservation in the process, while the spectro-temporal properties of the signal are a replica of those of the co-propagating pump and rather reflect the energy conservation. For an ultrashort pump pulse, our quantum analysis has retrieved results analog to what was predicted in the classical description of the MOPO [1, 12], but with some additional limitation. Conversely to what predict in [1], our results impose a precise inferior limit to the observable bandwidth of the backward idler photon, which cannot be narrower than the phase-matching bandwidth $\Omega_{gvs} = 1/\tau_{gvs}$.

In the regime of stimulated pair production (Chapter IV) below the MOPO threshold, the analysis was mainly devoted to the investigation of the effects of the feedback mechanism on the temporal coherence and correlation of twin beams in the transition from below to above threshold, for a monochromatic CW pump field. We developed a fully analytical model based on a unitary input-output transformation formalism which describes the system in the regime of an undepleted monochromatic pump. Through this model we characterized the transition from the regime far from threshold, where the dominant process is the spontaneous production of photon pairs, to the regime close to threshold, where the combined effect of stimulated PDC and distributed feedback affects dramatically the properties of the light source. A narrowing of the spectra and the consequent widening of the correlation and coherence times is predicted when approaching the threshold for coherent emission. This critical slowing down of the quantum fluctuations and critical divergence of the correlation time, which is typical of phase transitions, is studied for the first time in this system. We also gave an intuitive picture explaining the main characteristics of the coherence and correlation of the fields in the transition between the low gain and the high gain regime. We also presented

some preliminary results for the transition of the system from below to above threshold: numerical simulations suggests that the spectral bandwidth of the source diminishes to a minimum at the MOPO threshold and broadens again when moving away. Lacking a full analytical model to describe the system above threshold, we do not have a straightforward physical explanation for this behaviour and further investigations are needed in order to characterize the properties of coherence and correlation of the generated twin beams in this regime.

We also investigated the potentiality of the source to generate squeezing and EPR type correlations in the threshold vicinity (Chapter V). We demonstrated that the quadrature correlations becomes asimptotically perfect as the MOPO threshold is approached. Moreover very good squeezing can be obtained in the whole MOPO bandwidth even for fixed phase-angles, in sharp contrast with the more common single-pass co-propagating geometry, where squeezing is more difficult to observe at fixed detection phase-angles, because the orientation of the squeezing ellipse varies rapidly within the PDC bandwidth (which is typically much larger than in the MOPO). The EPR correlations that characterize the MOPO close to threshold are in fact narrowband and very similar to those found in a standard optical parametric oscillators enclosed in a resonant cavity.

Our analysis focused mainly on the temporal properties of the counter-propagating twin beams along the direction collinear to the pump, neglecting the transverse spatial degrees of freedom of the field. We demonstrated (Chapter VII) that this approach was largely legitimated by the weak coupling between the spatial and the temporal degree of freedom characterizing the counter-propagating geometry. Twin photons, however, are in principle emitted along all directions without any constraint (angular dispersion related to phase-matching is indeed almost absent, in contrast to standard PDC). Since emission even orthogonal to pump direction is allowed, the boundary conditions along the crystal transverse dimension may play a significant role in experiments and display new features. Future research should therefore include non-collinear emission in order to provide a more realistic description of the source emission. In addition, the extension of our model to a waveguided configuration which limits the number of spatial modes would be also of great interest, in view of the promising application of developing an efficient source of heralded single photons in a pure state.

References

[1] C. Canalias and V. Pasiskevicius. Mirrorless optical parametric oscillator. *Nat. Photon.*, 1:459–462, Jun 2008.

[2] A. Christ, A. Eckstein, P. J. Mosley, and C. Silberhorn. Pure single photon generation by type-ipdc with backward-wave amplification. *Opt. Expr.*, 17(5):3441–3446, Mar 2009.

[3] C. K. Hong, Z. Y. Ou, and L. Mandel. Measurement of subpicosecond time intervals between two photons by interference. *Phys. Rev. Lett.*, 59:2044–2046, Nov 1987.

[4] C. K. Law, I. A. Walmsley, and J. H. Eberly. Continuous frequency entanglement: Effective finite hilbert space and entropy control. *Phys. Rev. Lett.*, 84:5304–5307, Jun 2000.

[5] W. P. Grice, A. B. U'Ren, and I. A. Walmsley. Eliminating frequency and space-time correlations in multiphoton states. *Phys. Rev. A*, 64:063815, Nov 2001.

[6] A. Gatti, E. Brambilla, L. Caspani, O. Jedrkiewicz, and L. A. Lugiato. *x* entanglement: The nonfactorable spatiotemporal structure of biphoton correlation. *Phys. Rev. Lett.*, 102:223601, Jun 2009.

[7] O. Jedrkiewicz, J.-L. Blanchet, E. Brambilla, P. Di Trapani, and A. Gatti. Detection of the ultranarrow temporal correlation of twin beams via sum-frequency generation. *Phys. Rev. Lett.*, 108:253904, Jun 2012.

[8] Yu. M. Mikhailova, P. A. Volkov, and M. V. Fedorov. Biphoton wave packets in parametric down-conversion: Spectral and temporal structure and degree of entanglement. *Phys. Rev. A*, 78:062327, Dec 2008.

[9] Malte Avenhaus, Maria V. Chekhova, Leonid A. Krivitsky, Gerd Leuchs, and Christine Silberhorn. Experimental verification of high spectral entanglement for pulsed waveguided spontaneous parametric down-conversion. *Phys. Rev. A*, 79:043836, Apr 2009.

[10] Alan Migdall, Sergey Polyakov, Jingyun Fan, and Joshua Bienfang, editors. *Single-Photon Generation and Detection: Physics and Applications*, volume 45 of *Experimental Methods in the Physical Sciences*. Academic Press, November 2013.

[11] S. E. Harris. Proposed backward wave oscillation in the infrared. *Appl. Phys. Lett.*, 9(3):114–116, 1966.

[12] Gustav Strömqvist, Valdas Pasiskevicius, Carlota Canalias, Pierre Aschieri, Antonio Picozzi, and Carlos Montes. Temporal coherence in mirrorless optical parametric oscillators. *J. Opt. Soc. Am. B*, 29(6):1194–1202, Jun 2012.

[13] Valdas Pasiskevicius, Gustav Strömqvist, Fredrik Laurell, and Carlota Canalias. Quasi-phase matched nonlinear media: Progress towards nonlinear optical engineering. *Opt. Materials*, 34(3):513 – 523, 2012.

[14] A. C. Busacca, C. L. Sones, V. Apostolopoulos, R. W. Eason, and S. Mailis. Surface domain engineering in congruent lithium niobate single crystals: A route to submicron periodic poling. *Appl. Phys. Lett.*, 81(26):4946–4948, 2002.

[15] C. Canalias, V. Pasiskevicius, R. Clemens, and F. Laurell. Submicron periodically poled flux-grown ktiopo4. *Appl. Phys. Lett.*, 82(24):4233–4235, 2003.

[16] G. Strömqvist, V. Pasiskevicius, C. Canalias, and C. Montes. Coherent phase-modulation transfer in counterpropagating parametric down-conversion. *Phys. Rev. A*, 84:023825, Aug 2011.

[17] Carlos Montes, Bernard Gay-Para, Marc De Micheli, and Pierre Aschieri. Mirrorless optical parametric oscillators with stitching faults: backward downconversion efficiency and coherence gain versus stochastic pump bandwidth. *J. Opt. Soc. Am. B*, 31(12):3186–3192, Dec 2014.

[18] K. Gallo, P. Baldi, M. De Micheli, D. B. Ostrowsky, and G. Assanto. Cascading phase shift and multivalued response in counterpropagating frequency-nondegenerate parametric amplifiers. *Opt. Lett.*, 25(13):966–968, Jul 2000.

[19] Stefano Longhi. Time-reversed optical parametric oscillation. *Phys. Rev. Lett.*, 107:033901, Jul 2011.

[20] Jacob B. Khurgin. Slowing and stopping photons using backward frequency conversion in quasi-phase-matched waveguides. *Phys. Rev. A*, 72:023810, Aug 2005.

[21] Chih-Sung Chuu and S. E. Harris. Ultrabright backward-wave biphoton source. *Phys. Rev. A*, 83:061803, Jun 2011.

[22] Robert W Boyd. *Nonlinear optics; 3rd ed.* Academic Press, Amsterdam, 2003.

[23] G. G. Gurzadian, V. G. Dmitriev, and D. N. Nikogosian. *Handbook of nonlinear optical crystals*. Springer-Verlag Berlin ; New York, 1991.

[24] M Born and E Wolf. *Principles of Optics*. Cambridge University Press, 7 edition, 1999.

[25] A. Yariv. *Quantum electronics*. Wiley, 1967.

[26] F. Zernike and J.E. Midwinter. *Applied nonlinear optics*. Wiley series in pure and applied optics. Wiley, 1973.

[27] Y.J. Ding and J.B. Khurgin. Backward optical parametric oscillators and amplifiers. *Quantum Electronics, IEEE Journal of*, 32(9):1574–1582, Sep 1996.

[28] L. Caspani. *Spatiotemporal structure of entanglement in Parametric Down Conversion*. PhD Thesis, 2010.

[29] R. Loudon. *The Quantum Theory of Light*. Oxford University Press, 1992.

[30] Albert Ferrando, Mario Zacarés, Pedro Fernández de Córdoba, Daniele Binosi, and Álvaro Montero. Forward-backward equations for nonlinear propagation in axially invariant optical systems. *Phys. Rev. E*, 71:016601, Jan 2005.

[31] Milton Abramowitz and Irene A. Stegun. *Handbook of Mathematical Functions with Formulas, Graphs, and Mathematical Tables*. Dover Publications, New York, 1972.

[32] Gustav Strömqvist, Valdas Pasiskevicius, and Carlota Canalias. Self-established non-collinear oscillation and angular tuning in a quasi-phase-matched mirrorless optical parametric oscillator. *Appl. Phys. Lett.*, 98(5):–, 2011.

[33] T. Suhara and M. Ohno. Quantum theory analysis of counterpropagating twin photon generation by parametric downconversion. *IEEE Journal of Quantum Electronics*, 46(12):1739 – 17451, 2010.

[34] Mark C. Booth, Mete Atatüre, Giovanni Di Giuseppe, Bahaa E. A. Saleh, Alexander V. Sergienko, and Malvin C. Teich. Counterpropagating entangled photons from a waveguide with periodic nonlinearity. *Phys. Rev. A*, 66:023815, Aug 2002.

[35] Kiyoshi Kato and Eiko Takaoka. Sellmeier and thermo-optic dispersion formulas for ktp. *Appl. Opt.*, 41(24):5040–5044, Aug 2002.

[36] Artur Ekert and Peter L. Knight. Entangled quantum systems and the schmidt decomposition. *American Journal of Physics*, 63(5):415–423, 1995.

[37] S. Parker, S. Bose, and M. B. Plenio. Entanglement quantification and purification in continuous-variable systems. *Phys. Rev. A*, 61:032305, Feb 2000.

[38] M. P. van Exter, A. Aiello, S. S. R. Oemrawsingh, G. Nienhuis, and J. P. Woerdman. Effect of spatial filtering on the schmidt decomposition of entangled photons. *Phys. Rev. A*, 74:012309, Jul 2006.

[39] A. Gatti, T. Corti, E. Brambilla, and D. B. Horoshko. Dimensionality of the spatiotemporal entanglement of parametric down-conversion photon pairs. *Phys. Rev. A*, 86:053803, Nov 2012.

[40] K. Laiho, A. Christ, K. N. Cassemiro, and C. Silberhorn. Testing spectral filters as gaussian quantum optical channels. *Opt. Lett.*, 36(8):1476–1478, Apr 2011.

[41] Andreas Christ, Kaisa Laiho, Andreas Eckstein, Katiúscia N. Cassemiro, and Christine Silberhorn. Probing multimode squeezing with correlation functions. In *Research in Optical Sciences*, page QT1B.4. Optical Society of America, 2012.

[42] C. K. Law and J. H. Eberly. Analysis and interpretation of high transverse entanglement in optical parametric down conversion. *Phys. Rev. Lett.*, 92:127903, Mar 2004.

[43] P J Mosley, J. S. Lundeen, B.J. Smith, and I. A. Walmsley. Conditional preparation of single photons using parametric downconversion: a recipe for purity. *New Journal of Physics*, 10(9):093011, 2008.

[44] E. Brambilla, A. Gatti, M. Bache, and L. A. Lugiato. Simultaneous near-field and far-field spatial quantum correlations in the high-gain regime of parametric down-conversion. *Phys. Rev. A*, 69:023802, Feb 2004.

[45] William H. Press, Saul A. Teukolsky, William T. Vetterling, and Brian P. Flannery. *Numerical Recipes in FORTRAN; The Art of Scientific Computing*. Cambridge University Press, New York, NY, USA, 2nd edition, 1993.

[46] A. Einstein, B. Podolsky, and N. Rosen. Can quantum-mechanical description of physical reality be considered complete? *Phys. Rev.*, 47:777–780, May 1935.

[47] Z. Y. Ou, S. F. Pereira, H. J. Kimble, and K. C. Peng. Realization of the einstein-podolsky-rosen paradox for continuous variables. *Phys. Rev. Lett.*, 68:3663–3666, Jun 1992.

[48] D.F. Walls and G.J. Milburn. *Quantum Optics*. SpringerLink: Springer e-Books. Springer Berlin Heidelberg, 2008.

[49] Mikhail I. Kolobov. The spatial behavior of nonclassical light. *Rev. Mod. Phys.*, 71:1539–1589, Oct 1999.

[50] Morton H. Rubin. Transverse correlation in optical spontaneous parametric down-conversion. *Phys. Rev. A*, 54:5349–5360, Dec 1996.

[51] E. Gatti, A. Brambilla and L. A. Lugiato. *Quantum imaging*. E. Wolf, editor, Progress in Optics 51. 2008.

[52] Mete Atatüre, Giovanni Di Giuseppe, Matthew D. Shaw, Alexander V. Sergienko, Bahaa E. A. Saleh, and Malvin C. Teich. Multiparameter entanglement in femtosecond parametric down-conversion. *Phys. Rev. A*, 65:023808, Jan 2002.

[53] A. Gatti, R. Zambrini, M. San Miguel, and L. A. Lugiato. Multiphoton multimode polarization entanglement in parametric down-conversion. *Phys. Rev. A*, 68:053807, Nov 2003.

[54] O. Jedrkiewicz, A. Gatti, E. Brambilla, and P. Di Trapani. Experimental observation of a skewed x-type spatiotemporal correlation of ultrabroadband twin beams. *Phys. Rev. Lett.*, 109:243901, Dec 2012.

[55] A. Gatti, L. Caspani, T. Corti, E. Brambilla, and O. Jedrkiewicz. Spatio-temporal entanglement of twin photons: An intuitive picture. *International Journal of Quantum Information*, 12:1461016, May 2014.

Appendix A

Nonlinear polarization

The general expression for the $\chi^{(2)}$ nonlinear polarization can be written in the time domain as (see [22])

$$P_j^{(2)}(t) = \varepsilon_0 \int dt' \int dt'' \chi_{jkl}^{(2)}(t-t', t-t'') E_k(t') E_l(t''), \tag{A.1}$$

$$\chi_{jkl}^{(2)}(t,t') = 0 \text{ if } t < 0 \text{ or } t' < 0 \quad \text{(causality condition)}, \tag{A.2}$$

where $\chi_{jkl}^{(2)}(t,t')$ is the second-order suseptibility tensor that describes the non instantaneous response of the medium. Introducing the Fourier transform of the second-order susceptibility tensor:

$$\chi_{jkl}^{(2)}(\omega', \omega'') = \int \frac{dt'}{\sqrt{2\pi}} \int \frac{dt''}{\sqrt{2\pi}} e^{i\omega' t' + i\omega'' t''} \chi_{jkl}^{(2)}(t', t''), \tag{A.3}$$

and substituting in Eq.(A.1), we can derive the expression for the non linear polarization in the Fourier domain:

$$\begin{aligned}
P_j^{(2)}(t) &= \varepsilon_0 \int dt \int dt' \int \frac{d\omega'}{\sqrt{2\pi}} \int \frac{d\omega''}{\sqrt{2\pi}} e^{-i\omega'(t-t')-i\omega''(t-t'')} \\
&\qquad \times \chi_{jkl}^{(2)}(\omega',\omega'') \int \frac{d\omega_1}{\sqrt{2\pi}} e^{-i\omega_1 t'} E_k(\omega_1) \int \frac{d\omega_2}{\sqrt{2\pi}} e^{-i\omega_2 t''} E_l(\omega_2) \\
&= \varepsilon_0 \int \frac{d\omega'}{\sqrt{2\pi}} \int \frac{d\omega''}{\sqrt{2\pi}} \int \frac{d\omega_1}{\sqrt{2\pi}} \int \frac{d\omega_2}{\sqrt{2\pi}} e^{-i(\omega'+\omega'')t} \\
&\qquad \times \int dt' e^{i(\omega'-\omega_1)t'} \int dt'' e^{i(\omega''-\omega_2)t''} \chi_{jkl}^{(2)}(\omega',\omega'') E_k(\omega_1) E_l(\omega_2) \\
&= \varepsilon_0 \int \frac{d\omega'}{\sqrt{2\pi}} \int \frac{d\omega''}{\sqrt{2\pi}} \int \frac{d\omega_1}{\sqrt{2\pi}} \int \frac{d\omega_2}{\sqrt{2\pi}} e^{-i(\omega'+\omega'')t} \\
&\qquad \times (2\pi)^2 \delta(\omega'-\omega_1)\delta(\omega''-\omega_2) \chi_{jkl}^{(2)}(\omega',\omega'') E_k(\omega') E_l(\omega'') \\
&= \varepsilon_0 \int d\omega' \int d\omega''\, e^{-i(\omega'+\omega'')t} \chi_{jkl}^{(2)}(\omega',\omega'') E_k(\omega') E_l(\omega'')
\end{aligned}$$

Taking the Fourier transform with respect to time, we obtain

$$\begin{aligned}
P_j^{(2)}(\omega) &= \int \frac{dt}{\sqrt{2\pi}} e^{i\omega t} P_j^{(2)}(t) \\
&= \varepsilon_0 \int d\omega' \int d\omega'' \int \frac{dt}{\sqrt{2\pi}} e^{i(\omega-\omega'-\omega'')t} \chi_{jkl}^{(2)}(\omega',\omega') E_k(\omega') E_l(\omega'') \\
&= \varepsilon_0 \int d\omega' \int d\omega'' \chi_{jkl}^{(2)}(\omega',\omega'') E_k(\omega') E_l(\omega'') \delta(\omega-\omega'-\omega'') \\
&= \varepsilon_0 \int d\omega' \chi_{jkl}^{(2)}(\omega',\omega-\omega') E_k(\omega') E_l(\omega-\omega'). \qquad \text{(A.4)}
\end{aligned}$$

Appendix B

Relation between formalisms

Here we discuss the relataion between the low-gain field formalism (3.12) and the formalism of the biphoton state (3.16).

We start from the input-output relations (3.12), which represent the perturbative solution of the field propagation equations (3.4), correct up to first order in the parametric gain $g \ll 1$. The transformation (3.12) can be recast as

$$\hat{a}_j^{\text{out}}(\Omega) = \hat{R}^\dagger \hat{a}_j(\Omega)\hat{R}, \tag{B.1}$$

where $\hat{a}_j$ are the input operators (for brevity of notation we omitted the "in" superscript),

$$\hat{R} = \exp\left\{ \int d\Omega_s d\Omega_i [\psi(\Omega_s,\Omega_i)\hat{a}_s^\dagger(\Omega_s)\hat{a}_i^\dagger(\Omega_i) - \psi^*(\Omega_s,\Omega_i)\hat{a}_s(\Omega_s)\hat{a}_i(\Omega_i)] \right\} \tag{B.2}$$

and it is meant that only zero and first order in g have to be retained in the transformation (B.1). Conversely, by applying the generator of the transformation (B.1) to the input vacuum state and retaining only terms up to first order in g, one gets

$$|\phi\rangle_{\text{out}} = \hat{R}|0\rangle \approx \left[\hat{1} + \int d\Omega_s d\Omega_i \; \psi(\Omega_s,\Omega_i)\hat{a}_s^\dagger(\Omega_s)\hat{a}_i^\dagger(\Omega_i) \right] |0\rangle \tag{B.3}$$

which is the biphoton state (3.16). The second procedure, however, does not produce entirely equivalent results. To be precise, it produces equivalent results for second-order moments of field operators. As can be easily verified, the biphoton correlation $\langle \hat{a}_s(\Omega_s)\hat{a}_i(\Omega_i)\rangle$ and the coherence function $\langle \hat{a}_j^\dagger(\Omega)\hat{a}_j(\Omega')\rangle$ calculated with the output state (B.3) are the same as those taht will be calculated within the field formalism, displayed in formulas (3.17), and (3.54) and (3.55), respectively. However, some differences arise for higher order moments. Let us consider, for example, the autocorrelation of intensities in each signal-idler arm. The

field approach gives the thermal-like formula (3.56), while the calculation with the biphoton state gives only the shot noise term of Eq. (3.57). For $g \to 0$ the two results asymptotically coincide. However, when considering the normally ordered part of the correlation, in the field formalism,

$$\langle : \hat{I}_j(\Omega)\hat{I}_j(\Omega') : \rangle = \langle \hat{I}_j(\Omega) \rangle \langle \hat{I}_j(\Omega') \rangle + |G_j^{(1)}(\Omega, \Omega')|^2, \tag{B.4}$$

while with the biphoton state,

$$\langle : \hat{I}_j(\Omega)\hat{I}_j(\Omega') : \rangle = 0. \tag{B.5}$$

These differences arise from the truncation at first order in g: In the field formalism it leaves the possibility of generating multiple photon pairs, although with a smaller and smaller probability. As a result, the marginal statistics of each beam is the thermal statistics corresponding to a very low mean photon number, where the probability of having more than one signal or idler photon is small but not zero. Conversely, the truncation at first order on the state has a more drastic effect, leaving only a two-photon state, for which the probability of having more than one photon in each arm is exactly zero, which implies relation (B.5).